

Universidade de São Paulo  
Instituto de Física

Sistema de imagem de grande área, sensível à energia,  
para fluorescência de raios-X baseado em detectores  
GEM.

Geovane Grossi Araújo de Souza

Orientador: Prof. Dr. Marco Bregant  
Co-orientador: Prof. Dr. Hugo N. Luz

Monografia apresentada ao Instituto de Física como requisito  
parcial para a qualificação no Curso de Doutorado em Ciê-  
ncias.

São Paulo  
2021



University of São Paulo  
Physics Institute

Large sensitive area and energy dispersive X-ray  
fluorescence imaging system based on GEM detectors.

Geovane Grossi Araújo de Souza

Supervisor: Prof. Dr. Marco Bregant  
Co-supervisor: Prof. Dr. Hugo N. Luz

Report submitted to the Physics Institute of the University  
of São Paulo for the Doctor of Science Qualifying Exam.

São Paulo  
2021



# Resumo

As técnicas de imageamento por fluorescência de raios-X ou por transmissão de raios-X são de suma importância pois são consideradas não invasivas e não destrutivas. Sua utilização tem uma importância imprescindível nas análises de patrimônios histórico e cultural, medicina e indústria. Mais especificamente no âmbito da curadoria de arte e patrimônio, existe a necessidade de autenticação de obras e diversos museus e grupos trabalham com técnicas e instrumentação para caracterização de pigmentos, materiais e sua eventual autenticação através de técnicas de arqueometria.

Este trabalho consiste na construção, estudo e caracterização de um detector gasoso de grande área, sensível à posição e com resolução em energia baseado em GEMs (*Gas Electron Multiplier*), optimizado para operar na faixa de energia entre 1 keV e 30 keV. Esses detectores de micro-estruturas apresentam resultados satisfatórios para amostras grandes pois permitem a reconstrução de imagens sem a necessidade de fazer uma varredura no objeto estudado. Além disso, podem alcançar altas taxas de contagens, apresentam baixo custo quando comparados com os detectores de estado sólido e ganhos elevados pois podem ser utilizados em estruturas multiplas para multiplicação. Ademais, o manuseio e manutenção desses detectores é relativamente simples quando não são utilizados gases inflamáveis e tóxicos, e acabam sendo versáteis em relação à montagem, podendo detectar diferentes tipos de radiação.

Junto com os resultados experimentais um conjunto de simulações computacionais foram feitas de forma a ajudar no projeto, estudo e construção do detector, adequando a sua montagem da melhor maneira à aplicação desejada.

**Palavras-chave:** Detectores de radiação, detectores gasosos baseados em micro-estruturas, detectores do tipo GEM, imagem de fluorescência de raios-x.



# Abstract

X-ray fluorescence and X-ray transmission imaging techniques are of great importance as they are considered non-invasive and non-destructive. They are applied in the fields of cultural and historical heritage study, medicine and industry. Specifically in the field of curating art and cultural patrimony, there is the need to authenticate pieces and many museums and groups are working into the development of new archeometric techniques and instrumentation to characterize pigments and materials.

This work consists of the assembly, study and characterization of a large area, position sensitive, and energy dispersive X-ray gaseous detector based on GEMs (*Gas Electron Multiplier*), optimized to operate in the energy range of 1 keV to 30 keV. The advantage of using such large detectors is to reconstruct images without the need to scan the sample. These detector are cheaper when compared to solid state devices, they can reach high gains using multiple multiplication structures and with the suitable read-out electronics it is possible to work at high counting rates. Moreover, handling these detectors is relative simple since they can work without flammable and toxic gases and by doing small changes related to their assembly, it is possible to detect different types of radiation.

Along with the experimental results, a set of simulations were made in order to adapt these detectors that were first used in high energy physics in a lower energy scenario such as X-ray fluorescence.

Keywords: Radiation detectors, micropattern gaseous detectors, Gas Electron Multiplier, X-ray Fluorescence imaging.



# Contents

<b>1</b>	<b>Introduction</b>	<b>11</b>
<b>2</b>	<b>Radiation interaction with matter</b>	<b>13</b>
2.1	Electromagnetic radiation . . . . .	13
2.1.1	Photoelectric effect . . . . .	13
2.1.2	Compton scattering . . . . .	14
2.1.3	Pair production . . . . .	15
2.2	Attenuation of radiation by matter . . . . .	16
2.3	Characteristic X-rays emission or X-ray fluorescence . . . . .	16
2.4	Electrons and Positrons . . . . .	17
2.4.1	<i>Bremsstrahlung</i> . . . . .	18
2.5	Ions . . . . .	20
2.6	Neutrons . . . . .	20
<b>3</b>	<b>Gaseous detectors</b>	<b>23</b>
3.1	The single and multi wire proportional detectors . . . . .	25
3.2	Microstrip Gas Chamber . . . . .	26
3.3	Micromesh Gaseous Structure . . . . .	27
3.4	Gas Electron Multiplier . . . . .	28
3.5	The time projection chamber principle . . . . .	30
<b>4</b>	<b>Detector characterization</b>	<b>31</b>
4.1	Efficiencies . . . . .	31
4.1.1	Conversion or quantum efficiency . . . . .	31
4.1.2	Collection and extraction efficiencies . . . . .	32
4.2	Detector gain . . . . .	33
4.3	Ion back-flow . . . . .	34
4.4	Measuring efficiencies, ion back-flow and gain in the laboratory . . . . .	34
4.5	Energy resolution . . . . .	36

<b>5 The detector, the scalable read-out system and the SAMPA chip</b>	<b>37</b>
5.1 The detector . . . . .	37
5.1.1 The geometry for XRF imaging . . . . .	38
5.2 The scalable read-out system . . . . .	39
5.3 The SAMPA chip . . . . .	39
<b>6 Simulations</b>	<b>41</b>
6.1 Quantum efficiency and energy resolution: . . . . .	41
6.2 Photon escape probability . . . . .	44
6.3 Copper background contamination. . . . .	46
6.4 Geometric response . . . . .	52
6.5 Simulating a read-out system and reconstruction algorithms . . . . .	56
6.5.1 Strip read-out system . . . . .	57
6.5.2 Flat-field correction algorithm for strip read-outs . . . . .	60
6.6 Ion back-flow reduction . . . . .	63
6.6.1 New geometries . . . . .	63
6.6.2 Using a mesh to reduce the IBF . . . . .	67
<b>7 Experimental results</b>	<b>73</b>
<b>8 Conclusion and next steps</b>	<b>79</b>
8.0.1 Schedule . . . . .	80

# Chapter 1

## Introduction

There is no doubt that the discovery of X-rays changed the world and was a important breakthrough to science, industry and medicine. Since the first detection of such radiation, using platinocyanide plates by Wilhelm Conrad Röntgen [1], new detection techniques and technologies are being developed to improve the quality and capability of doing X-ray images.

After the development of energy-dispersive detectors we were able to use different approaches such as X-ray fluorescence (XRF)[2] and particle-induced X-ray emission (PIXE)[3] to make spectral analyses, obtained important results and developments in fields such as geology, cultural heritage studies and new materials development.

Gaseous detectors are a class of detectors that are sensitive to ionizing radiation and can either be or not energy-dispersive, that is, capable to distinguish X-rays with different energy, and thus, create a energy spectrum of a sample. These detectors are dated from the first decades of the 20th century and their use has not changed since then, consisting into collect the free charge carriers generated by the passage of ionizing radiation inside a gaseous volume [4].

Since the creation of the Multi-Wire Proportional Chamber (MWPC) by Charpak [5], a detector capable to locate the radiation interaction vertex, and years later the development of the Time Projection Chamber (TPC) by Nygren [6], these detectors are being widely used in the high energy physics experiments.

The new photo-lithography methods developed in the last few decades to create printed circuit also helped in the advance of gaseous detector. The micropattern gaseous detectors (MPGD) family is composed by different detectors such as the *Gas Electron Multiplier* (GEM) [7], the MICROMEGAS [8], the Thick-GEM [9] (*Thick-Gas Electron Multiplier*), the *Micro-Hole and Strip Plate* [10] and the ThickCOBRA [11]. These detectors form the new generation of proportional gaseous detectors and have shown good performance on high energy physics experiments in terms of spatial resolution, counting rate, radiation hardness, operational stability, as well as to be suitable to cover large regions (up to  $32\text{ m}^2$  in the ALICE TPC for example[12]).

## INTRODUCTION

---

MPGDs are structures used to amplify the primary charge generated after the radiation interaction with the medium. They are constructed using high precision photo-lithography followed by chemical or physical etching, a process similar to the one used on printed circuit factories. By applying a suitable potential to the MPGD structure it is possible to create a region that achieves the Townsend breakdown voltage [13], generating a multiplication region that amplifies the signal. Since some of the MPGDs are semi-transparent to the passage of electrons, it is possible to stack multiple structures, achieving high gains and a good signal-to-noise ratio.

Following all these planar amplifying structure it is possible to place a set of segmented electric conductive electrodes and using a multichannel reading electronic, calculate the vertex of interaction inside the detector. Using this assembly one can cover a large sensitive area for a much lower price when compared to Solid State Detectors (SSD).

The objective of this project is to develop a X-ray fluorescence image system based on GEMs, using a strip segmented read-out system that reads the charge collected by each strip independent. This way it is possible to make images with spatial resolution of a few hundred microns and with low image distortions or artifacts. Along with the experimental setup we are developing tools and algorithms to adjust the responsive curve of the detector in order to make quantitative analyses of samples using gaseous detectors.

This work is divided into chapters and the content covered in each of them is as follows. In chapter 2, it is possible to find a description of the most important concepts regarding the electromagnetic radiation interaction with matter. The MPGDs are versatile detectors and can detect different types of radiation, such as Neutrons or UV-light, however, here we will focus on the effects related to electromagnetic radiation.

Chapter 3 explains to the reader the family of gaseous detectors, their difference and applications in different fields.

Chapter 4 will introduce to the reader the different tools and definitions that describe the detector behavior and how to characterize it.

Chapter 5 is focused in simulations. We want to better understand how the detectors works and one way to do it is by using computational tools, such as the Garfield++[14]. Also, as a contribution to the RD51 collaboration[15] a study regarding the ion back-flow in GEM detectors and ways to suppress it are shown.

In chapter 6 we introduce the reader to the Scalable Read-out System (SRS) and the SAMPA chip.

In chapter 7 we show preliminary experimental results.

Chapter 8 is the conclusion of this work until now, with an overview of the results and future work.

# Chapter 2

## Radiation interaction with matter

The passage of radiation in a medium may create charged particles. Collecting and processing the signal generated by these charge carries is the principle of operation of most radiation detector. The mechanism of interaction and the energy loss and consequently the number of charged particles created are going to be different for X-rays photons, electrons, ions or neutrons. This section will provide a brief review on each one of this processes.

### 2.1 Electromagnetic radiation

Photons are electromagnetic radiation produced by electronic transitions and the acceleration of charged particles. If these photons have a wavelength between about 0.01 to 1 nm (energies between 124 eV to 124 keV) they are conventionally named X-rays. Due to this broad energy range, different effects may occur when X-ray interact with matter. There is no partially absorbed X-ray when it interacts with the medium, and so, a photon beam traveling through a material will be attenuated in intensity but will not suffer from energy degradation, and this will be a difference when comparing interaction with matter of photons and of charged particles or neutrons, for example.

#### 2.1.1 Photoelectric effect

In 1887 Hertz discovered that the probability to create an electric discharge between electrodes was higher when it was irradiated by ultra-violet (UV) electromagnetic radiation [16]. The mechanism was named photoelectric effect and it was only fully comprehended when Einstein proposed a theory to explain this phenomenon. The energy of each photon is equal to the product of electromagnetic frequency  $\nu$  with Planck's constant  $h$ . When the photon energy value is higher than the bidding energy of the electron in the material, it can be ejected, passing from a bound state to a free state.

The kinetic energy of an electron ejected from the atom is given by:

$$K = h\nu - W, \quad (2.1)$$

where  $W$  is the binding energy between the electron and the atom, also known as the work function and  $h$  is the Planck's constant. This effect is only feasible if the photon have at least the energy equals to  $W$ . The cross-section for photoelectric effect in the K-shell can be calculated using the Born approximation. Disregarding relativistic effects ( $h\nu \ll m_e c^2$ ), the cross-section (for the K-shell only) is given by equation 2.2 [4].

$$\sigma_p = \frac{8\pi Z^5 \alpha^4 4\sqrt{2}}{3} \left( \frac{e^2}{m_e c^2} \right)^2 \left( \frac{m_e c^2}{h\nu} \right)^{7/2}, \text{ for } h\nu > E_K \quad (2.2)$$

where  $m_e c^2$  is the invariant mass of the electron,  $\alpha$  is the fine structure constant, which is equal to  $\frac{1}{137}$  and  $Z$  is the atomic number of the target. This equation gives the probability of interaction between the photon and the K-shell electron and it scales with  $Z^5$ , but decreases rapidly as the photon energy increases, as the  $(h\nu)^{-3.5}$  dependency of the last term of the equation shows. In the energy range of this work this effect is going to be the major component of energy deposition by radiation in matter (as figures 2.4 and 2.3 shows) and the most important, since it is the effect that will lead to the generation of a characteristic X-ray emission, which is the aim of this work.

### 2.1.2 Compton scattering

The Compton scattering or Compton effect is the inelastic scattering between a photon and a free electron [17], that is, due to this interaction the wavelength of a photon will be shifted, giving part of its energy to the electron and therefore, depositing energy in the medium.

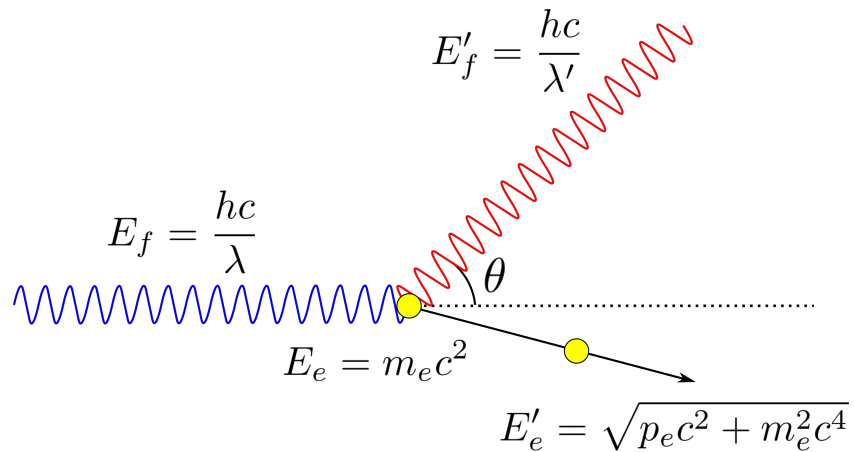


**Figure 2.1:** Compton effect diagram.

One can describe the problem writing both the energy and momentum conservation of the

system as:

$$\vec{P}_p = \vec{P}'_p + \vec{P}'_e$$

$$E_p + E_e = E'_p + E'_e$$

The initial momentum of the electron is neglected, since it is considered to be in rest. Rewriting and substituting expressions, it is possible to reach equation 2.3, which describes the relationship between the initial and final energies of the photon:

$$E'_p = \frac{E_p}{1 + \frac{E_p}{m_e c^2} (1 - \cos \theta)} \quad (2.3)$$

or depending on the wavelengths, as seen in equation 2.4 [17]:

$$\lambda' - \lambda = \frac{1}{m_e c} (1 - \cos \theta) \quad (2.4)$$

As can be seen in figure 2.1, after the interaction, part of the photon energy will be transferred to the electron, resulting in a partial energy deposition and a radiation wavelength shift. Looking at figures 2.3 and 2.4 it is possible to see that in the energy range of X-rays, the contribution to the total absorption cross section is dominated by photo-electron effect, and so, this energy shift and absorption generated through the Compton mechanism can be neglected.

### 2.1.3 Pair production

The pair production is the creation of pairs of electrons and positrons by high energetic photons like the ones generated in colliders, by heavy nuclei decays and astronomical events such as gamma-ray bursts. The pair production becomes possible only when the photon's energy is greater than twice the rest mass of an electron, 1.022 MeV.

The photon needs to interact with the nuclei Coulomb field (which is a requirement for momentum conservation [4]), and then it is converted into a pair, as can be seen in figure 2.2. Due to the high mass of the nucleus, its recoil energy is negligible.

After losing energy to the medium through Coulomb interaction, the positron may encounter an electron and they are annihilated in a process that emits a pair of photons. These photons are emitted back-to-back and this well known characteristic is exploited in many different techniques that have application not only in physics but also in medicine such as the positron emission tomography (PET)[18].

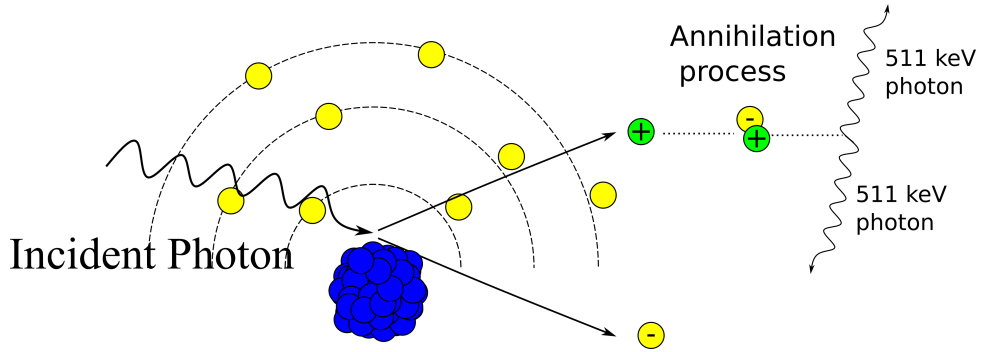


**Figure 2.2:** Pair production diagram.

## 2.2 Attenuation of radiation by matter

As was said before, X-rays are not degraded in energy when they interact with matter, they are only attenuated in intensity. The Lambert–Beer law describes how the absorption and attenuation of electromagnetic radiation by a material takes place, and it has a great importance in nuclear physics studies and radiologic protection. A mono-energetic beam, with intensity  $I_0$ , is attenuated according to the following equation:

$$I = I_0 e^{-\lambda x} = I_0 e^{-\mu \rho x}, \quad (2.5)$$

where,  $I$  is the beam intensity after passing through the material,  $\lambda$  is the linear attenuation coefficient,  $\mu$  is the mass attenuating coefficient, equal to  $\frac{\lambda}{\rho}$ , expressed in  $(\text{cm}^2/\text{g})$ ,  $\rho$  is the material density and  $x$  is its thickness.

Each effect related to the interaction of radiation with matter occurs with a certain probability, which is related with the photon energy and the target's atomic number, thereby, the linear attenuation coefficient  $\lambda$  can be written:

$$\lambda = \tau + \sigma + \kappa, \quad (2.6)$$

where  $\tau$ ,  $\sigma$  and  $\kappa$  are the contributions related to photo-electric effect, Compton effect and pair production respectively. In figure 2.4 one can visualize the region of predominance for each one of the effects as a function of the atomic number and energy.

## 2.3 Characteristic X-rays emission or X-ray fluorescence

Electrons can be ejected from inner atoms shells if this atom get hit by a high energy photon or a charged particle. The atom that has a unfilled shell is considered excited and this means that it is unstable. For the atom to achieve stability it needs to liberate a certain amount of energy. One way to achieve that is by filling this inner electronic shell with an outer electron and in

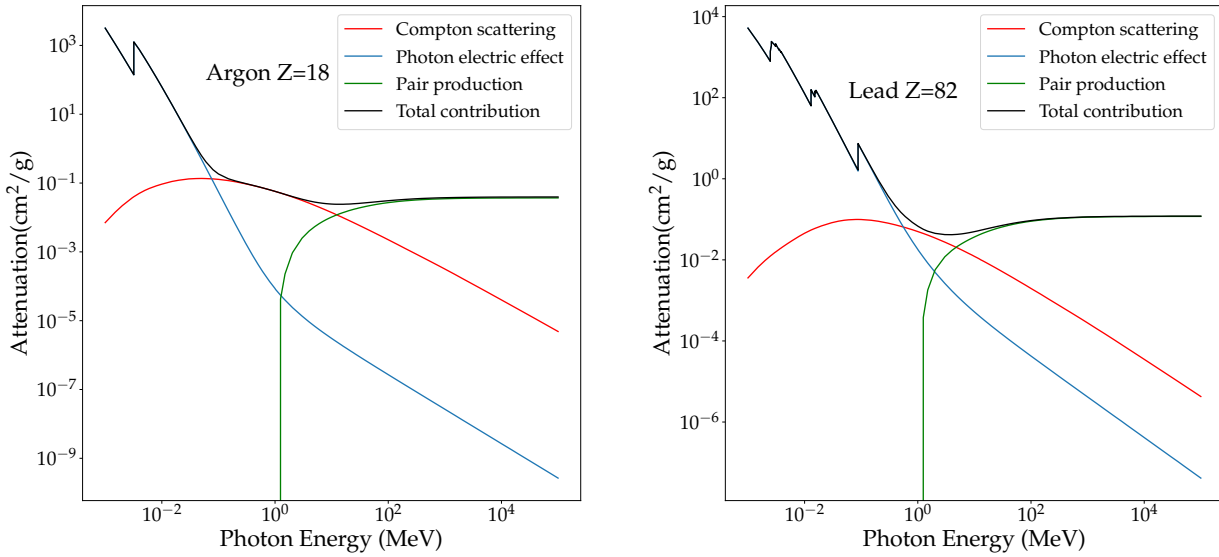


**Figure 2.3:** Mass attenuation coefficient for argon and lead as a function of the energy. Values obtained from the XCOM database [19].

the process emitting a characteristic X-ray with energy equal to the energy difference between the final and initial states, as figure 2.5 shows.

For heavier the atoms, equivalent shells will have greater energy differences, and the characteristic X-rays will be more energetic. The transitions gets their name by the electronic shell that was filled and they get a sub index which is related to the shell where this transition electron came from. If its initial state was on a L or M shell, it will get named as K<sub>α</sub> or K<sub>β</sub> respectively. Since the energy difference grows for outer shells, β transitions will be more energetic than α ones. The maximum energy that a K-series photon shows is produced by filling the vacancy with an unbound electron, and the energy corresponding to this transition is given by the K shell binding energy[13].

X-ray fluorescence spectrometry consists on the analysis of the spectra of photons emitted by a sample after it has been irradiated by ionizing radiation. The peaks on each spectrum will indicate the presence of different elements, since their emission lines are unique. This powerful technique is non-invasive and non-destructive, thus being useful to identify different elements on rare and inestimable samples.

## 2.4 Electrons and Positrons

The electrons and positrons will deposit energy in the medium by two different processes, the collisional and the radiative (Bremsstrahlung). The first one is similar as for other heavy charged particles and Hans Bethe developed a theory for the energy loss regarding this compo-

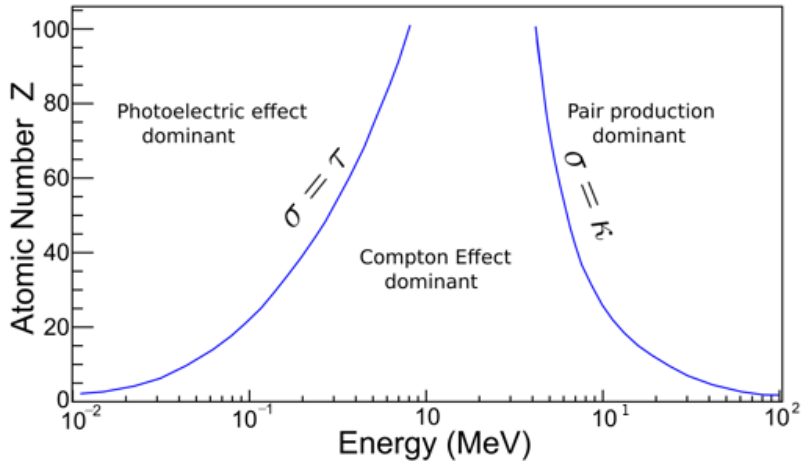


**Figure 2.4:** Radiation interaction predominant effect as a function of energy and atomic number. The lines indicate the region where neighboring effects have the same contribution. Adapted from [20].

ment in 1930[21]. The second will depends on the medium atomic number and also the initial electron energy. The ratio between the energy loss due to collisional and radiative process for an electron can be written as:

$$\frac{(dE/dx_r)}{(dE/dx_{col})} \approx \frac{EZ}{700} \quad (2.7)$$

where  $E$  is the electron energy in units of MeV and  $Z$  is the medium atomic number. It can be seen that the contribution of the energy loss due to radiative processes for the electrons in the energy range of 1-30 keV, the one we are interest in this work, is small and can be neglected when talking about gaseous detectors filled with argon or krypton.

Each interaction between fast electrons and orbital electrons will result in a large amount of momentum transference due to the equal masses that they have, therefore, a larger amount of energy is lost in a single collision, resulting in abrupt changes of trajectory and energy deposition. Thus, when compared with ions, the path traveled by these fast electrons is much more chaotic[13].

### 2.4.1 *Bremsstrahlung*

The “braking radiation” or Bremsstrahlung in German is the radiation emitted by any charged particles after undergoing a force field. These photons are emitted by the moving particle when they interact with a magnetic field or another charged particle for example. This acceleration can be positive or negative and tangential or perpendicular to the vector of velocity. For higher kinetic energies and target atomic numbers, the conversion of kinetic energy into radiation will be larger [13]. This process is extremely important in the X-rays production and happens in

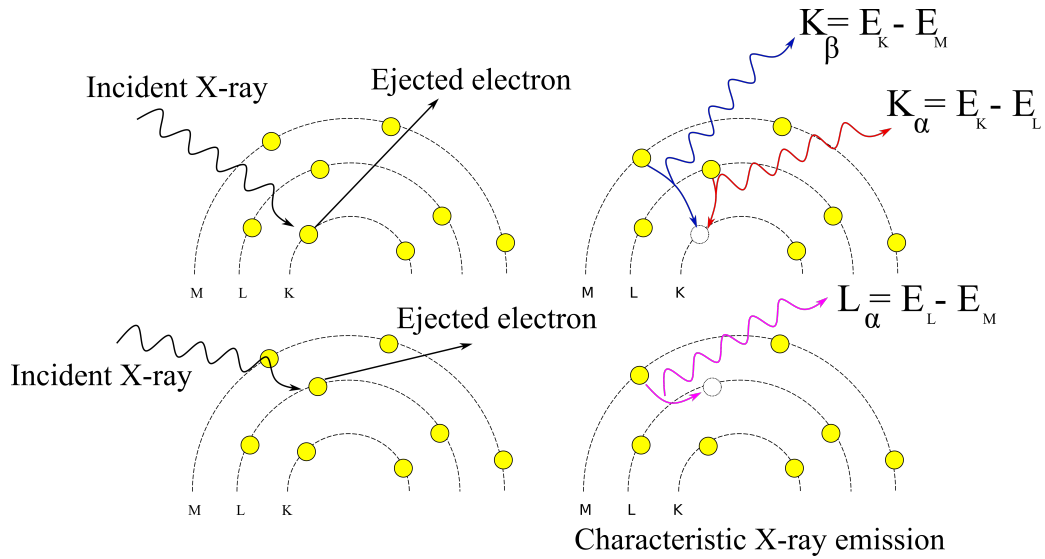


**Figure 2.5:** The emission of a fluorescence X-ray.

giant Synchrotron accelerators and in commercial X-rays tubes sources.

In commercial X-ray sources bremsstrahlung radiation is generated by the decelerating electron when they are throw into a target. If the energy is high enough, along with this continuous background spectrum, characteristics X-rays are generated, just as figure 2.6 shows, and its energy will depend on the target used inside the X-ray tube.

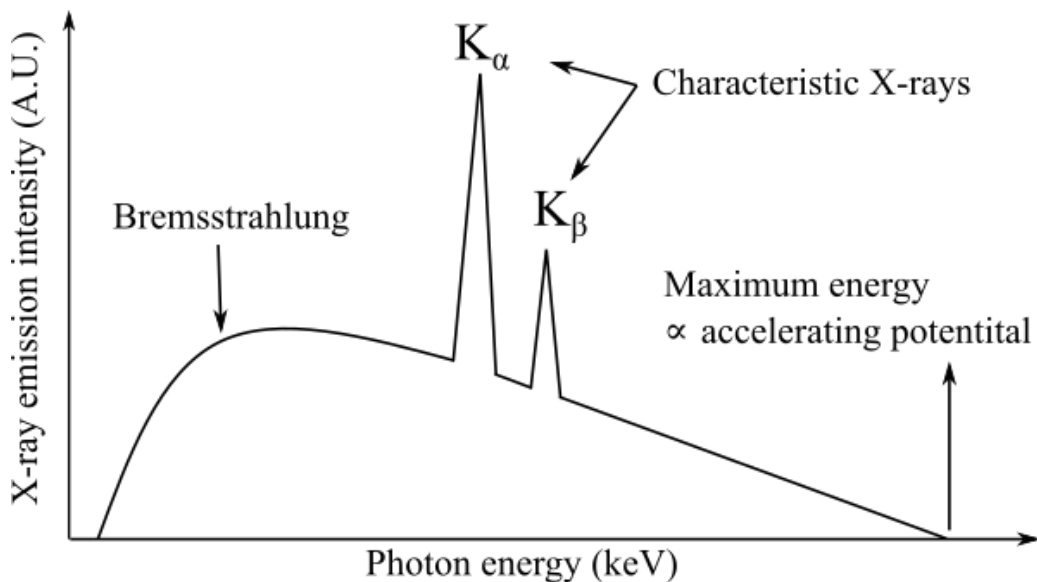


**Figure 2.6:** The emission of a commercial X-ray tube.

## 2.5 Ions

The heavy charged particles will interact through coulomb force between the ion positive charge and the electrons of atom orbitals. The interactions may create excitation or ionization in the atoms of the medium and the ion will lose velocity at each encounter. Differently than for electrons, the ion track will be much more defined.

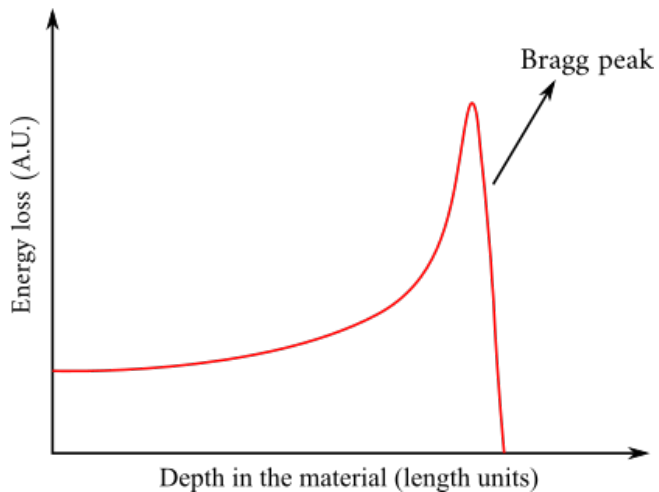


**Figure 2.7:** Example of an ion energy loss curve in a material.

It can be seen in figure 2.7, that the amount of energy loss in the track will be higher towards the end of the ion's traveled path. This is known as the Bragg peak and happens because at lower velocities(end of a track), the energy loss reaches its maximum. At the very end, the ion capture electron, get neutralized and the  $dE/dx$  drops sharply [4].

## 2.6 Neutrons

The basic mechanism to detect neutrons is to use a conversion element, which will capture the neutron, and as a result, will generate a charged particle or a high energy photon which will be detected according to the mechanisms that were shown before.

For many years  ${}^3\text{He}$  was one of the most used gas to convert neutrons into charged particles, however, in the last two decades, due to the high demand and low production, many facilities are running out of it[22].

To overcome this problem, other elements which have the capability to convert neutrons are being tested. Figure 2.8 shows the neutron interaction cross-section for different elements.

Two promising elements to replace  ${}^3\text{He}$  are the  ${}^{157}\text{Gd}$  and  ${}^{10}\text{B}$ . The conversion mechanism for these elements can be seen below:



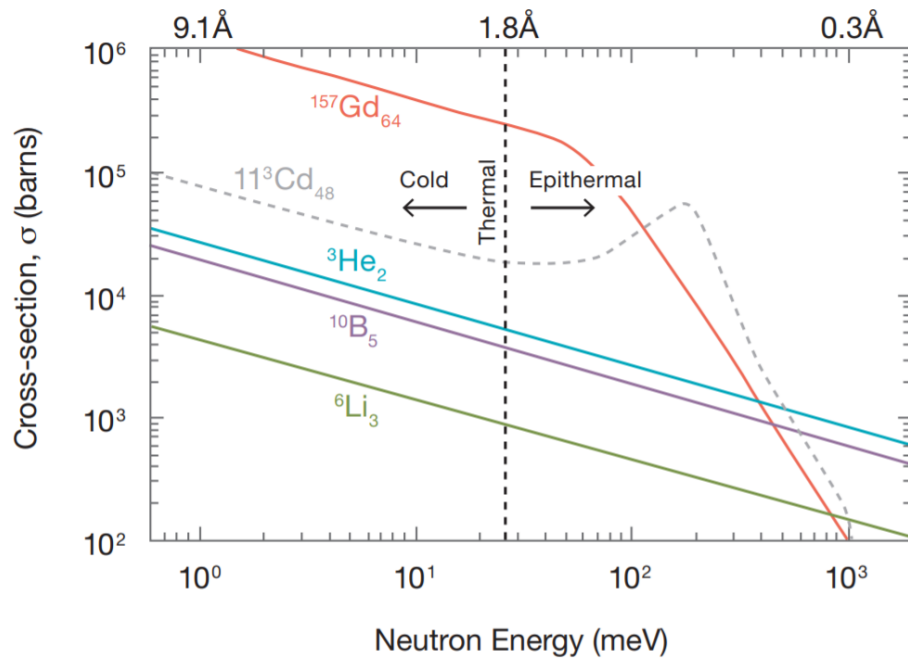
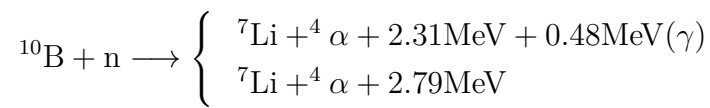


**Figure 2.8:** Neutron interaction cross-section for different conversion elements. Figure from [23].





# Chapter 3

## Gaseous detectors

The basic principle of operation of any radiation detector is to use an absorbent medium, i.e., a material which will have its physical properties changed due to the passage of radiation. The first radiation detectors for example, the photographic plates, suffered from a chemical reaction induced by the passage of a charged particle or an photon. Once exposed, the light-sensitive chemicals became more or less opaque depending on the amount of exposure [24].

Modern gaseous radiation detectors still use these properties and figure 3.1 exemplifies it. A charged particle will create a track of ionization inside the medium. By applying a potential on the electrodes, it is possible to collect ions and electrons and by using a proper electronics, transform this charge into a signal that can be read and interpreted. According to different characteristics of the signal it is possible to discover parameters related to the original event, such as the energy deposited in the medium and the type of charged particle.

Depending on the applied electric field, the output pulse height will change, and consequently, we may divide the regions of operation of gaseous detectors according to this behavior as figure 3.2 shows.

In the first region the voltage applied to electrodes is not high enough to avoid charge recombination and therefore signals are lost and a detector cannot operate at this condition. Increasing the electric field we reach the first regime of operation for gaseous detectors, which is the ion saturation. In it, the charge carriers generated by the ionizing radiation reaches the read-out electrodes without any type of amplification. The electric field applied in the system is high enough only to prevent pair recombination and to avoid non-linear effects in the signal that is read. Increasing the electric field in this region will not change the pulse height, since the multiplication threshold is not reached and the most famous detector that operates in this regime are the ionization chambers.

In the proportional regime the electric field is high enough to reach charge multiplication. The primary electrons generated, very few, a charge of the order of atto-coulomb ( $10^{-18}$ ), drifts towards specific structures inside the detector and there they are multiplied. To reach the mul-

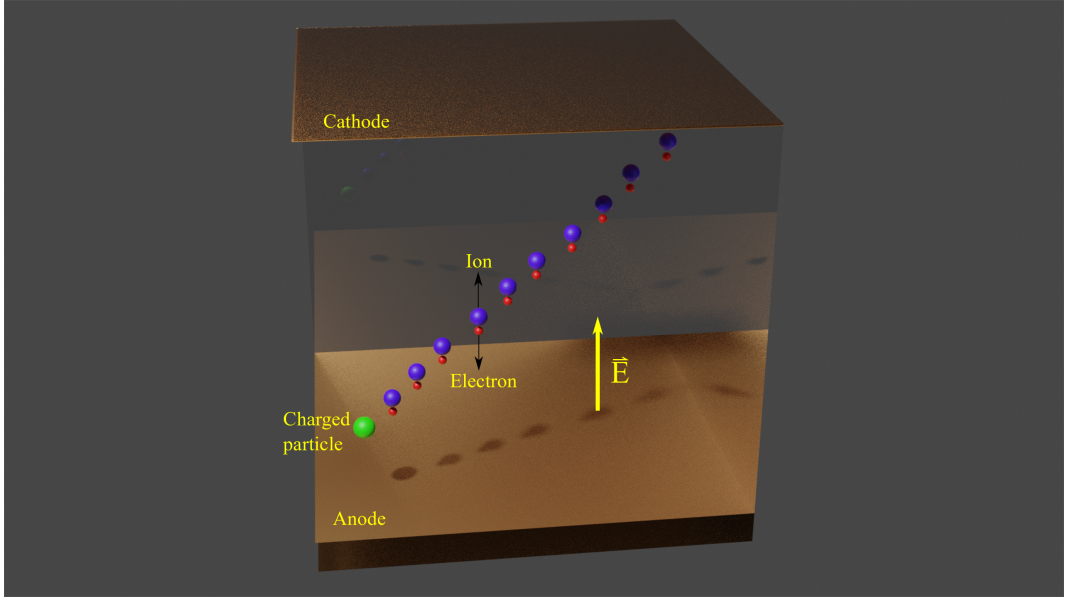


**Figure 3.1:** Basic principle of operation of any radiation detector.

tiplication threshold, an electric field of the order of  $10^6$  V/m for typical gases at atmospheric pressure is used [13], accelerating the electrons and giving them enough kinetic energy to create new electron-ion pairs and sustain the so called Townsend avalanche process (fig. 3.3). Detectors such as the Single and Multiwire Proportional Chambers and the Micropattern Gaseous Detectors (MPGD), which will be described in detail in the following sections, operate in this regime. The name of this region of operation is related to the output signal pulse height, which is proportional to the energy deposited by the radiation. These detectors are widely used since it is possible to obtain both information about the average rate of ionization and the energy deposited by each event.

As we continue to increase the electric field between the electrodes, we go through a region where the proportional regime is not valid due to non-linear effects and we reach the Geiger-Müller region. Working at this level of field intensity, no matter the energy of the ionizing radiation detected, it will always generate an electric discharge throughout all the detector's volume. In this discharge, the energy information is completely lost since all signals will have the same height. Detectors such as the Geiger-Müller counter are widely used to measure the radioactive source activity. If one increase the electric field applied on the electrodes for even higher values, the dielectric breakdown potential can be reached leading to a continuous discharge inside the detector spoiling completely the operation of the device.

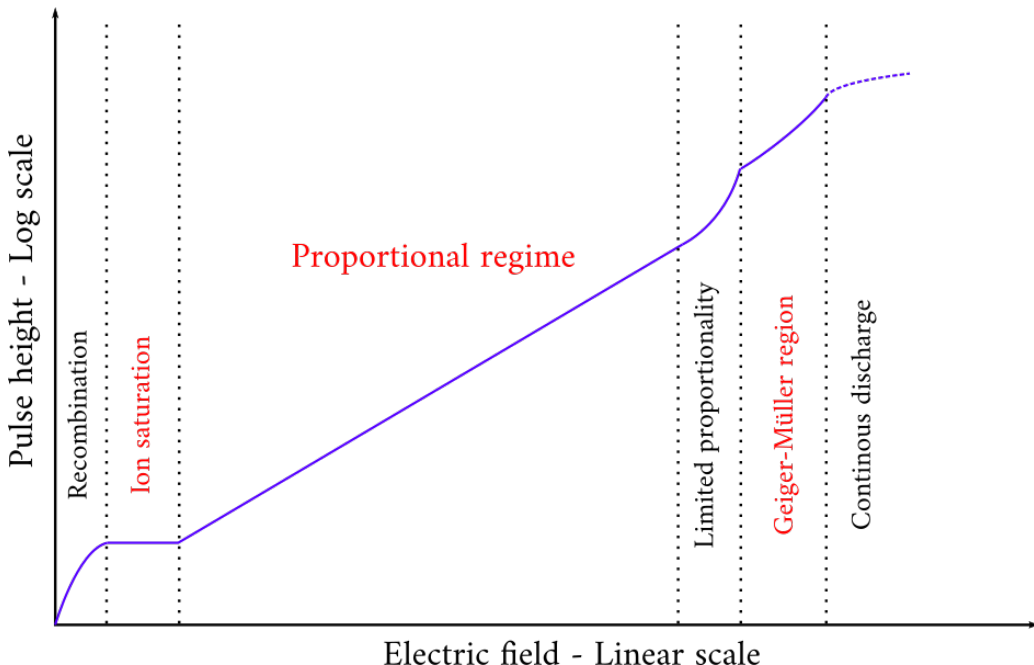
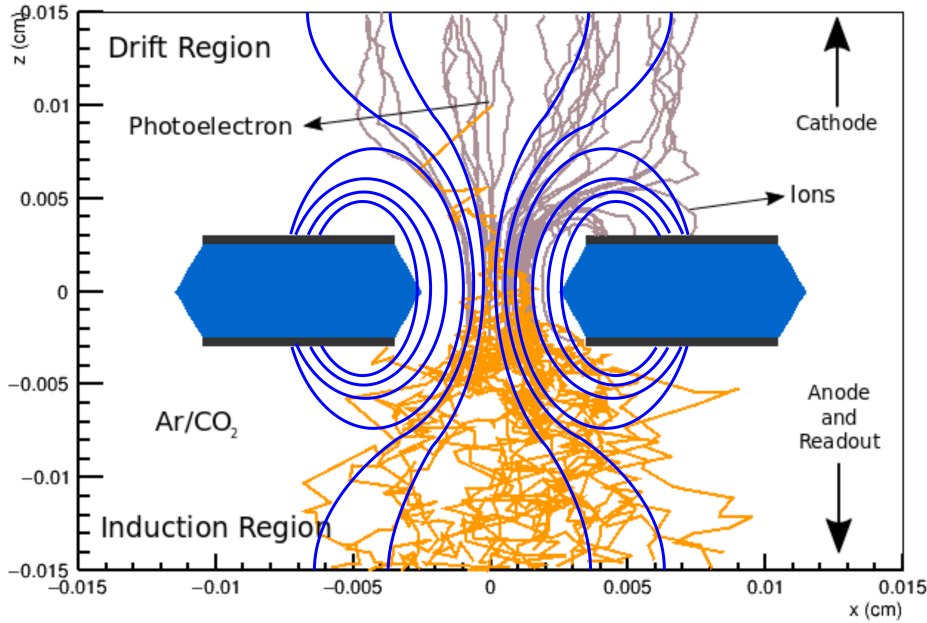


Figure 3.2: Regions of operation of gaseous detectors. Adapted from [13].

### 3.1 The single and multi wire proportional detectors

The first detector and most simple detector of the proportional regime is the single wire counter. This detector consists of a cylinder filled with gas, were a single conductive wire is stretched right in the middle of this gaseous volume. Filling it, normally with a inert gas and applying high voltage to this wire, it is possible to create a multiplication region in its vicinity, thus multiplying any charge that goes close enough to this anode just as figure 3.4 shows (by using the Gauss's law one can calculate the electric field at the vicinity of the wire and see that it grows with the inverse of the distance).

The Multi Wire Proportional Chamber (MWPC) [5], created by Georges Charpak, who was awarded the Nobel Prize of Physics in 1992 because of this invention, is an extension of the single wire principle. In his detector, several wires are placed in parallel to each other occupying a large area. Two cathodes plate are placed above and below the plane defined by the wires as figure 3.5 shows. By collection the charge in each wire it is possible to determine the position of interaction inside the detector using the center of mass algorithm (explained in details on chapter 6). Due to the possibility to detect position and energy, the MWPC played a huge role on the development of the particle and nuclear physics, being the core of detectors like the Time Projection Chambers (TPC)(e.g. [25]) and Tracking Chambers(e.g. [26]).



**Figure 3.3:** Simulation of the charge multiplication processes through Townsend mechanism inside a GEM detector. The orange lines represent the electron trajectories while the gray ones represent the positive ions. The blue lines are the representation of the electric field lines.

## 3.2 Microstrip Gas Chamber

The first MPGD developed was the Microstrip Gas Chamber (MSGC), created by Anton Oed in 1988 [27]. Just like the single wire and the MWPC, it has a simple architecture, where the electrode that creates the charge multiplication region also works as the read-out. Alternated strips of cathodes and anodes are etched above a dielectric quartz substrate. By applying a potential difference between these electrodes it is possible to create a multiplication region close to the anodes. The ions are collected in the cathode strips.

The pitch between anode strips is typically  $200\text{ }\mu\text{m}$  and the width of them are only  $10\text{ }\mu\text{m}$ . The cathode strip is placed in the middle of two different anode electrodes and it is larger, having a width of  $90\text{ }\mu\text{m}$ , although these structures seems to be small, they can be easily constructed by photo-lithography processes. The MSGC have the advantage to neutralize ions just after they are created by a multiplication, differently from the MWPC, where the ions goes towards the drift region and are neutralized after a long drift time, by a conductive grid or the cathode plane. This drives the collection time to shorter value, making the detector faster in terms of data acquisition and with lower dead time. Although the time response and spatial resolution are better when compared to the MWPC this detector presents low gains since it has only one multiplication stage and have major aging issues, where sparks can easily destroy the strips when high potentials are applied. These same issues can be seen in the MWPC and

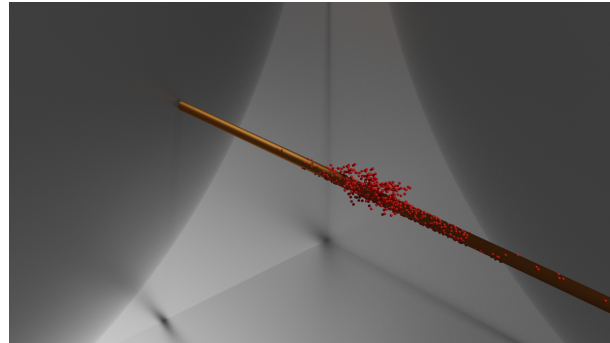


**Figure 3.4:** Single wire proportional detectors. The high electric field in the vicinity of the wire generate a multiplication region.

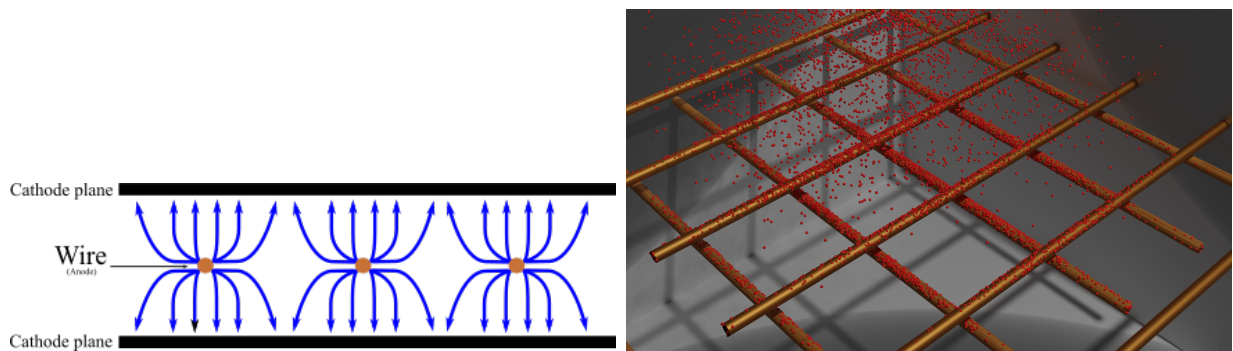


**Figure 3.5:** MWPC principle. A set of wires will create several multiplication regions and the collection of charge in each one of them can be used to determine the interaction position inside the gaseous volume.

the problem is that the multiplication and read-out structure are made by the same electrode, therefore aging processes and spark damage can completely kill a strip or even the hole detector.

### 3.3 Micromesh Gaseous Structure

The MICRO MEsh GAseous Structure (MICROMEGAS) was developed by a former disciple of Georges Charpak, Yannis Giomataris in 1996 [8]. This structure consists on an mesh structure electrode placed just above a read-out circuit. To sustain this structure, 100  $\mu\text{m}$  high quartz pillar spacers are used. Figure 3.7 shows the complete model.

The voltage difference between the mesh and the anode focuses the primary electrons towards the 100  $\mu\text{m}$  gap between both electrodes, where a high electric field multiplies this charge. This device is able to achieve very large gains with a very good intrinsic ion backflow suppression, a effect that will be discussed further on the text, but is a limiting factor on the operation of gaseous detector. To determine the position of interaction, a strip read-out is used and it consists of a set of parallel strip. The bulk MICROMEGAS production technique has very early allowed to achieve sensitive areas well above 1  $\text{m}^2$ .

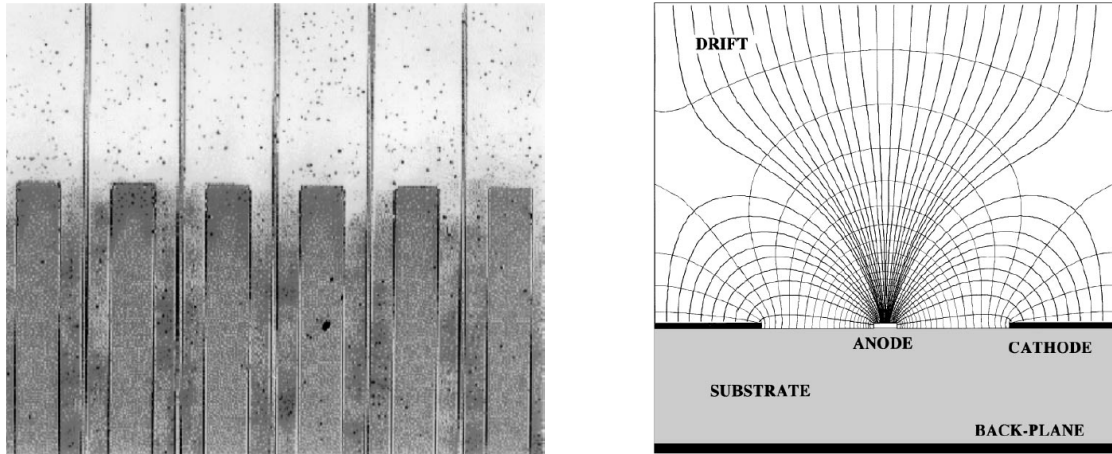


**Figure 3.6:** Left: The microstrip pattern. Right: Numerical calculation of the electric field generated by the strips. Images from [28].

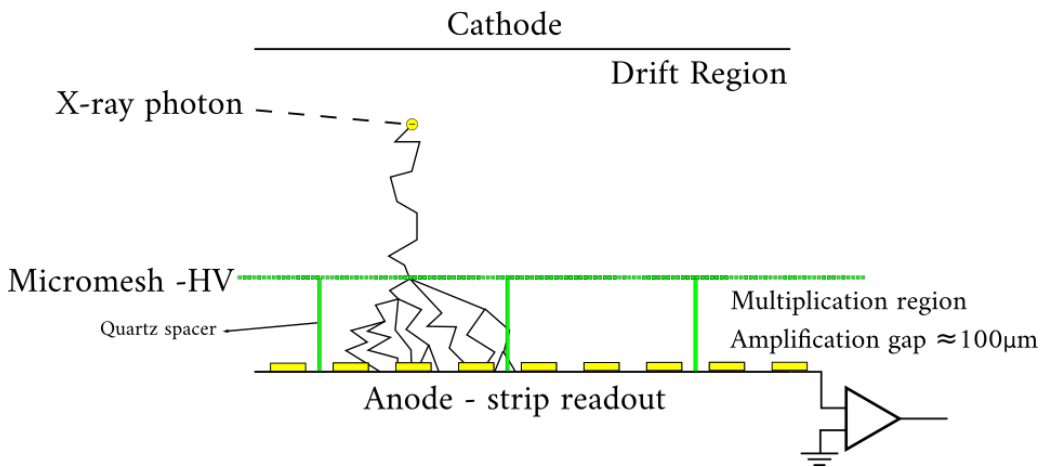


**Figure 3.7:** MICROMEGAS design.

An actual use of the MICROMEGAS can be found at the New Small Wheels (NSW) of the Muon Spectrometer of the ATLAS experiment. The detector is undergoing an upgrade for Run 3 and it will be composed by 8 MICROMEGAS layers for tracking in combination with 8 sTGCs (Small Strip Thin Gap Chambers) for triggering. Each wheel is composed by a set of two MICROMEGAS sandwiched by two sTGCs [29]. Due to the proximity between the multiplication region and the read-out, the detector's dead time is small, about 100 ns, linked only with the drift time for the ions to be collected by the mesh [30].

### 3.4 Gas Electron Multiplier

The Gas Electron Multiplier was created by Fabio Sauli in 1997 [7] (former colleague of MICROMEGAS's inventor Yannis Giomataris and also a Georges Charpak's disciple) and it was originally conceived to be a first multiplication stage for the MSGC, increasing the gain and

protecting the strips from discharges caused mainly due to the high potentials applied. It was observed however, that the GEM itself was able to operate at a very high gain, without the need of the MSGC, allowing to decouple the charge multiplication from the collection electrode, protecting very well the readout electronics.

The detector consists on a layer of dielectric material (normally it is used Kapton<sup>TM</sup> (polyimide, a dielectric polymer resistant to heat), covered on both sides by a thin conductive layer. By photo-lithography processes and chemical etching, holes are perforated in a hexagonal matrix [28]. The standard GEM produced at CERN is made using a 50  $\mu\text{m}$  kapton foil, covered on both sides by a 5  $\mu\text{m}$  copper layer. The holes are etched in a way that they get a bi-conical shape, with 70 microm diameter at the conductor layer and 50  $\mu\text{m}$  in the center of the dielectric. A standard value for the pitch between holes is 140  $\mu\text{m}$ .

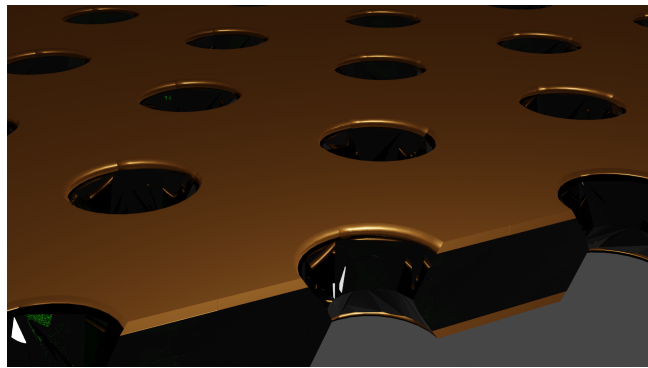


**Figure 3.8:** 3D model of a GEM foil.

By applying a potential difference between the copper electrodes, it is possible to create electric field of the order of  $10^4$  V/cm inside the GEM holes, focusing the primary electrons and creating a charge multiplication region, as shown in figure 3.3. Since the GEM structure allows the passage of electrons, one advantage of using GEMs is the possibility to stack several foils, creating multiple multiplication stages, achieving gains of the order of  $10^3$  with a single multiplication stage in Ar/CO<sub>2</sub> mixtures and above  $10^5$  with a triple GEM stack in a wide range of noble gases mixtures [31].

One of the problems when dealing with high counting rates is the flow of ions to the drift region (the sensitive volume of the detector), the so called ion backflow, which may spoil parameters such as the charge velocity in the drift region and energy resolution. The GEM however, shows a intrinsic suppression of this charge and so it is a good candidate to compose detectors. Dealing with any MPGD requires a clean environment, in order to avoid the deposition of suspended particles on the electrodes, specially in the holes which may lead to leak currents and increased spark risk.

The GEMs are replacing the MWPC in many high energy physics experiments and are now used in major detectors at CERN such as ALICE's TPC [32], the muon detector of the

CMS [33] and the LHCb [34] and the tracking chambers of COMPASS [35]. The foil can also be adapted by applying different coatings to its surface, making the GEM capable to detect other types of radiation, such as neutron (using  $^{157}\text{Gd}$ [36] and  $^{10}\text{B}$ [37, 38, 39] coatings) and UV photons (using CsI [40]).

### 3.5 The time projection chamber principle

The TPC concept was created by David Nygren in the late 1970s[6], when he invented a chamber that was capable to reconstruct the 3D trajectory of charged particles and by doing so, to identify the products after a collision. Figure 3.9 illustrate the basic principle of operation of a TPC. The high energetic charged particle will deposit energy in the gas, thus creating a track of charge carriers pairs. Applying a very uniform electric field across this volume drift the electrons towards a specific direction. Here is where the MPGDs show their true potential. Since they have the capability to cover large areas, they will multiply this electrons and after a while, the primary track will generate a projection on a read-out plane, giving information of the X and Y coordinates.

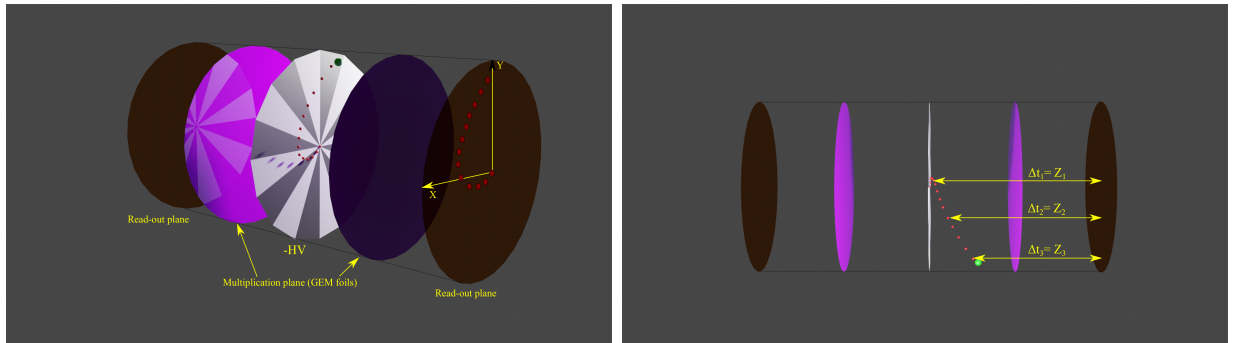


**Figure 3.9:** Time projection chamber principle. Left: Trajectory projection on the X-Y plane. Charged particles affected by a magnetic field will generate a round pattern Right: The Z component is obtained using the charge drift time.

The Z component is obtained by the time difference of each signal due to different paths traveled. The uniform electric field is required, along with a good time resolute electronics, to achieve a good spatial resolution in the Z direction, since it is completely related with the mean velocity of the charge carries in the gas. The particle is identified using the Lorentz force, that is, applying a magnetic field, to bend the particle trajectory and using it to obtain its charge and mass. The energy loss in the TPC will also helps in the charge identification.

# Chapter 4

## Detector characterization

To be able to compare different detectors capabilities, or between MPGDs or with different assembly, a set of measurements can be made in the laboratory or even simulated using different software. The complete study of these characteristics gives a complete vision regarding the quality of the equipment designed and how its is located when compared with other equipment.

In this chapter the reader will encounter the definition of different parameters used to characterize not only a gaseous detector, but also an imaging system.

### 4.1 Efficiencies

When talking about radiation detectors the quantum or conversion efficiency gives the capability of the system to convert the radiation into something that can be later acquired by the reading electronics and converted into information. In the case of gaseous detectors we also have to deal with the drift of the charge along a path until it can be collected and the lost of information during this time needs to be avoided.

To take into account this signal and to extract the best information regarding an event, the detector is tuned in terms of electrodes arrangement, potentials applied and the type of gas that can be used, along with its physicals properties.

#### 4.1.1 Conversion or quantum efficiency

The conversion efficiency of a detector, as said before, is the capability for the system to interact with the radiation and transform this energy into something that can be read or interpreted. Using a scintillator gas such as  $\text{CF}_4$  for example will transform part of the energy deposited by the radiation into photons with wavelength of visible light[41]. Although interesting, it is unfeasible to count or detect radiation this ways, and so, one thing that is used are detectors capable to collect this photons, transform them into charge and than create a image. This is

the basic principle of any digital camera. In the case of gaseous detector such as GEMs, we can collect directly the charge that is created inside the active volume.

Using the attenuation length coefficient  $\lambda$  and the Lambert-Beer we can calculate the attenuation of a beam with intensity  $I_0$  passing through matter and leaving the material with intensity  $I$ . The ratio  $I/I_0$  can be interpreted as the escape probability for a single photon.

$$P(x) = e^{-\frac{x}{\lambda}} \quad (4.1)$$

where  $x$  is the length traveled by the photon inside the medium. One can calculate the interaction probability or the conversion probability getting the complementary part, in other words,  $1 - P(x)$ . After the absorption of the photon, the electrons generated must reach the read-out system. Since not all of them are capable to drift towards the electronic system and their charge can be very low, these electrons need to be multiplied first by a GEM or other similar structure.

### 4.1.2 Collection and extraction efficiencies

The charge generated after the radiation deposits energy in the material will drift through the detector according to the electric field configuration. In the case of the GEM detector, there is a probability for the electron to hit for instance the top electrode of the GEM and thus be lost. Some works tried to model the charge transport inside a GEM based detector just by looking at the electric field and potentials configuration[42] and by doing experimental measurements[43]. However, slight changes in the geometry of the problem and displacement of the detectors parts may change the amount of charge that is collected, multiplied, and in the end hits the read-out plane.

To compare and study different experimental setups one can calculate different transport efficiencies for MPGDs. One of the main goals of these studies is to achieve the maximum values for each one of these quantities in order to get a large amount of information regarding the event and the best possible signal-to-noise ratio. The collection efficiency of a GEM is the capability to direct the charge towards the multiplication region as figure 4.1 shows.

Considering only the electron charge, the collection efficiency for a GEM foil can be calculated using the following relation:

$$C^- = 1 - \frac{Q_{\text{top}}}{Q_{\text{prim}}} \quad (4.2)$$

where  $Q_{\text{top}}$  and  $Q_{\text{prim}}$  are the the charge deposited at the top copper electrode and the primary charge respectively. This definition comes in hand when one wants to simulate the efficiencies and the ion charge can be left aside. The extraction efficiency gives the capability to remove the charge from the multiplication region and directs it towards another GEM to the read-out

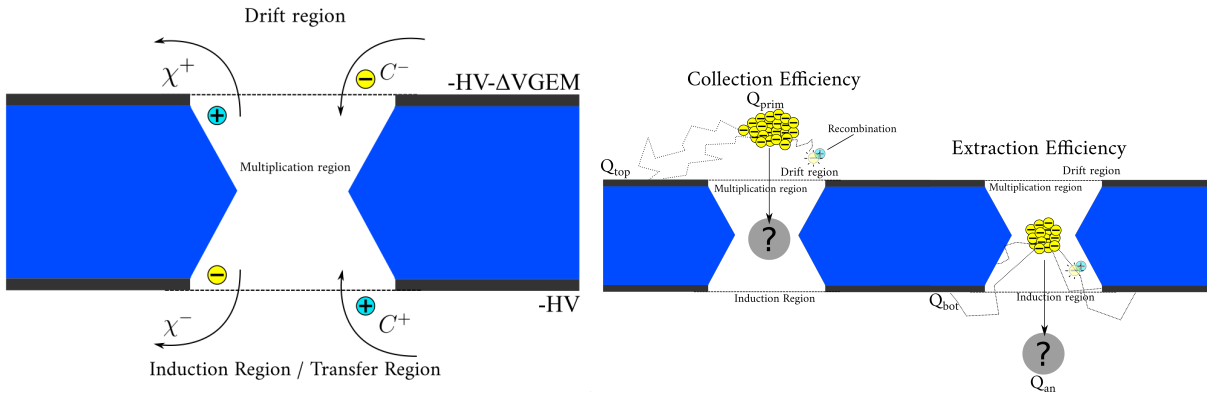


**Figure 4.1:** Definition of collection( $C$ ) and extraction efficiencies( $\chi$ ) for electrons and ions.

system. It can be calculated as shown below:

$$\chi^- = \frac{Q_{an}}{Q_{an} + Q_{bot}} \quad (4.3)$$

where  $Q_{bot}$  and  $Q_{an}$  are the electron charge deposited in the bottom electrode of the GEM and the read-out respectively. In simulations it is possible to distinguish the charge collected that came from ions and from electrons. In the case of ions, the definitions are analogous but the electrodes that are chosen to count the charge are going to be inverted due to the different direction of movement for the positive charge.

## 4.2 Detector gain

The gain of the detector is the capability to multiply the primary charge that was generated in the active region. It has two different definitions, the absolute gain that is the multiplication factor of the charge created inside the detector and the effective gain, which describes the amount of charge that actually reached the read-out electronics. The effective gain can be defined as the amount of charge which hits the read-out system ( $Q_{an}$ ) divided by the primary charge ( $Q_{prim}$ ).

$$G_{eff} = \frac{Q_{an}}{Q_{prim}}; \quad (4.4)$$

The absolute gain is calculated counting the total charge generated in the detector that reached every electrode after multiplication and it can be related to the effective gain using the relation below:

$$G_{abs} = \frac{Q_{tot}}{Q_{prim}} = \frac{G_{eff}}{C^- \chi^-} \quad (4.5)$$

## 4.3 Ion back-flow

Ion back-flow is one of the major limiting problem for gaseous detectors. It can be described as the flow of positive charge to the drift region of the detector and it may affect the behavior of the system as a whole. If a large amount of positive charge travels towards the cathode of the detector the drift field can be affected, leading to problems related with energy resolution (recombination and loss of the primary charge) and even position resolution in the case of TPCs due to deviations in the electron trajectories.

The definition for ion back-flow is the following:

$$\text{IBF} = \frac{I_{\text{cat}}}{I_{\text{an}}} \quad (4.6)$$

where  $I_{\text{cat}}$  are the cathode and  $I_{\text{an}}$  the anode current.

## 4.4 Measuring efficiencies, ion back-flow and gain in the laboratory

The definition that were shown previously are very useful to be used in simulated data, where there is a clear identification on the contributions of positive and negative charges. To calculate these quantities in the laboratory can be tricky. In order to obtain the primary current experimentally it is possible to use the following relation:

$$I_p = eN_p n \quad (4.7)$$

where  $e$  is the electron charge,  $N_p$  is the number of primary electrons, that can be calculated using the photon mean energy and the gas work function and  $n$  is the event rate. Although this measurement seams straight forward in the laboratory, it can be seen that this type of calculation has a high deviation for non mono-energetic photons, since the mean energy will have a higher uncertainty. Another way to do this same measurement is to apply the same potential on the top and the bottom electrode of the GEM (no amplification), and use a femtoammeter to measure the current generated at the cathode by the primary ions.

Calculate gain and efficiencies in the laboratory can be much more difficult and complex than in simulations. While in the simulations you can determine certain quantities just by looking at the initial and final position of charge carriers, in the laboratory we need to measure currents. Although there is a complex contribution from positive and negative charges on the currents measured, it is possible to calculate both efficiencies, the IBF and absolute gain by using 4 different ammeters. The definition of currents can be seen on figure 4.2.

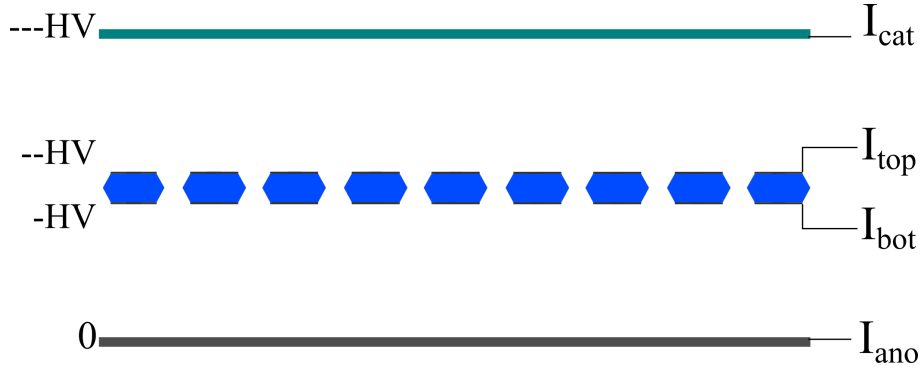


**Figure 4.2:** Currents used to experimentally characterize the detector.

$$I_{cat} = Q_{prim} + Q_{prim} C^- G_{abs} \chi^+ \quad (4.8)$$

The cathode current is composed by the primary ions plus the ones that compose the IBF, which are equal to the absolute gain times the extraction efficiency for ions( $\chi^+$ ).

$$I_{top} = -Q_{prim}(1 - C^-) + Q_{prim}G_{abs}(1 - \chi^+) \quad (4.9)$$

The top electrode current is composed by the primary electrons that does not reach the multiplication region and the ions that are not extracted.

$$I_{bot} = -Q_{prim}G_{abs}C^-(1 - \chi^-) \quad (4.10)$$

The bottom current is composed by all the electrons that are multiplied but are unable to leave the multiplication region.

$$I_{an} = -Q_{prim}G_{abs}C^-\chi^- = -Q_{prim}G_{eff} \quad (4.11)$$

The anode current is primary current times the effective gain of the detector. Using the ion back-flow definition and equations 4.8 and 4.11, we get the following:

$$IBF = \frac{1}{G_{eff}} + \frac{\chi^+}{\chi^-} \quad (4.12)$$

It is possible to see that there is 5 unknown variables( $G_{abs}$ ,  $\chi^-$ ,  $\chi^+$ ,  $C^-$  and  $Q_{prim}$ ) for 4 different current equations. However, it is possible to dodge this problem by using the results obtain through simulations to fix or calculate one of this variables. On chapter 6 this will be discussed in detail.

## 4.5 Energy resolution

Since we want to use gaseous detectors to measure the energy spectrum of photons, one of the most important parameters is the energy resolution. It is well known that due to statistical fluctuations in the pair creation inside the detector, the primary distribution of charge carriers is not a well defined line, but a distribution with some deviation around a mean value (more details are going to be discussed at chapter 6). In this work we calculate the energy resolution of the detector for a certain energy as the full width at half maximum (FWHM) of the distribution divided by the mean energy value ( $E_m$ ).

$$R_E = \frac{\text{FWHM}}{E_m} \quad (4.13)$$

# Chapter 5

## The detector, the scalable read-out system and the SAMPA chip

### 5.1 The detector

The fluorescence imaging system that is currently mounted in our laboratory consist of a triple-GEM detector with the dimensions shown on figure 5.1. We are operating this detector at atmospheric pressure and the electric field configurations were set such as to optimize collection and extraction efficiencies, selecting voltages (potentials) that our power supply can provide.

The detector is mounted on a FR4 PCB board that is also a support for the read-out strips and HV connectors. The detector frame, read-out plane and GEM foils were all designed and manufactured at CERN. The detector entrance window is a 50  $\mu\text{m}$  thick kapton foil. The frame is sealed with low vapor pressure viton O-rings and the only openings are the inlets and outlets gas tube in which a flow of 6 L/h passes through 4 mm tubes. The gas flow is controlled and measured accurately with digital mass flow controllers from Bronkhorst Hi-Tec [44], and the mixture composition (argon and carbon dioxide) can be set by the user.

Since we still want to change and optimize field characteristics, the bias of the GEM foils is done by independent high-voltage channels, using standard safety high voltage (SHV) connectors. In the future the idea is to remove most of the SHV connectors after the tuning of the detectors, making the bias distribution using only one HV channel and to choose values for each field by using high voltage resistors. This will transform the detector in a more compact structure that can be carried to other sites. As a power suppliers we are using a VME modules from CAEN [45] to distribute the voltage, controlling the system by a USB connection to a Raspberry Pi [46]. The HV control software was developed in HEPIC@IFUSP, providing live information, with safety features to protect the electronics against electrical discharges inside the detector. The coupling between the power supplier and the top electrode of the last GEM includes a low pass filter that successfully suppress frequencies down to around 60 Hz.

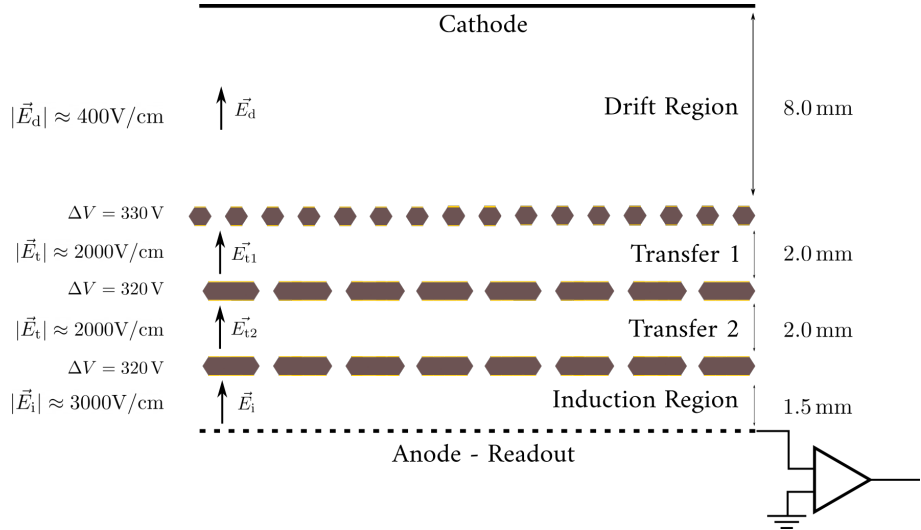


**Figure 5.1:** Scheme of the detector setup mounted in our laboratory and typical values of operation.

### 5.1.1 The geometry for XRF imaging

The difficult behind making X-ray fluorescence is the isotropically emission of photons when irradiating an object. Each piece of the sample will work as a punctual emission source and this will blur and degrades completely any image acquired, destroying the information regarding where a emission came from. To solve this problem 2 different approaches can be used. The first one is to use an multi-capillary optics or parallel collimators coupled with the detector window, mapping each point of the sample directly on the top of the detector. Another way to deal with problem is to use a pinhole setup. Using the same physical principle of Leonardo Da Vinci's *camera obscura*, it is possible to project light passing through a small hole, mapping an inverted image of an object in a plane. The advantage of using the parallel collimator optics is the higher flux of fluorescence photons that are able to reach the detector when compared to the pinhole geometry[47]. The disadvantage of using such method is that in every image, a projection of the collimator plate is going to appear, creating an additional artifact that can spoil image reconstruction. One advantage of the pinhole is the capability to magnify objects just by changing distance between parts of the setup. Figure 5.2 shows the two different setup that can be used for X-ray fluorescence imaging.

As mentioned before, the image made using a pinhole camera will be inverted and by playing with the distances of the sample and detector to the pinhole, magnification can be adjusted. Since in this work we want to test the capability of our imaging system, the distances between the pinhole and sample were kept the same (10 cm) and consequently the magnification equals to 1.

Currently we can use two different pinholes, with diameter and thickness of 1 mm: one in stainless steel and one in tantalum.

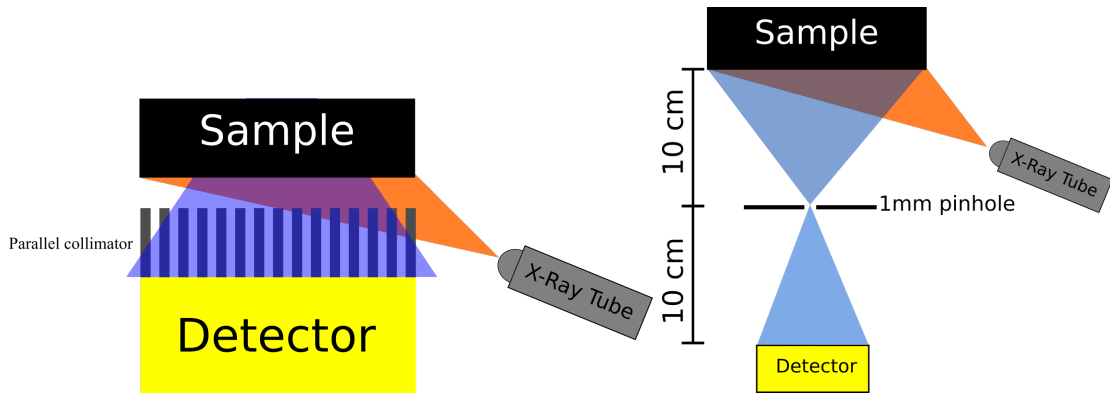


**Figure 5.2:** Different experimental setups to obtain fluorescence images. Left: Parallel collimator. Right: Pinhole geometry

## 5.2 The scalable read-out system

Developed at CERN, the SRS or Scalable Read-out System is a powerful electronics setup created to be a common back-end electronic to support different types of detectors and its front end electronics. One of the most used setups for gaseous detectors applications at the Gaseous Detector and Development laboratory at CERN and by members of the RD51 collaboration is to use the APV25, a CMOS (Complementary Metal Oxide Semiconductor) created to be used at the CMS tracker[48], as a multi-channel read-out chip. Using 4 APV25, it is possible to cover all the 512 electronic channels of the standard gaseous detector read-out, allowing to read each strip of the anode independently.

As the ‘scalable’ in the name SRS suggests, it can be used for table top experiments dealing with just a few electronics channels to systems with several thousands of them. In the case of using it for XRF fluorescence imaging, the advantage to read-out each anode strip independently is the improvement of spatial resolution when compared to resistive charge division[49]. The amount of data that is measured depends on the type of acquisition. For operations in non-zero suppression mode, where the wave form of the signal is saved, using the APV25 setup it is possible to achieve 50 Hz acquisition rate. If one wants to operate at zero suppression mode, that is, not reading or saving below a threshold, it is possible to acquired data at values above 1 kHz. It is possible to acquire data at higher counting rates (up to few MHz) using different chips such as the VMM[50] and in the future the SAMPA chip[51].

## 5.3 The SAMPA chip

The SAMPA chip is an ASIC (Application Specific Integrated Circuits) developed at the Integrated Systems Laboratory (LSI) of the USP Polytechnic School (POLI) aiming to serve both the TPC and the Muon Chambers of ALICE experiment. The chip is now being implemented

to the SRS to be a substitute for the APV25 since it is also capable to store the waveform. Each chip has 32 channels and operates at a nominal supply voltage of 1.25 V. Each channel is composed by a Charge Sensitive Amplifier (CSA), followed by shapers and a 10-bit Analog-to-Digital Converter (ADC) with sampling frequency of 10 MSps, with the capability to be run up to 20 MSps[51].

# Chapter 6

## Simulations

In this chapter we presents the results obtained throughout simulations. The aim is to better understand the behavior of the detector regarding its capability to detect radiation and, to find optimal ranges of applications and to understand effects that takes place in lower energy applications such as X-rays detection. The first study aimed in the overall quantum efficiency of the detector and the energy resolution limits for photons in the range of 1 keV to 30 keV. We have also model the copper background contamination, which is a intrinsic problem when using copper cladding GEM detectors to detect X-rays, we applied a flat-field correction to reduce image artifacts and we model how a peak of energy changes its intensity due to the different spatial response of the image system. Some simulations were conducted using Garfield++[14], a specific software for charge transport in gaseous detector and C++ and Python Monte Carlo (MC) codes written by the author.

### 6.1 Quantum efficiency and energy resolution:

As already stated, the standard detector that is currently mounted in our laboratory consists into a triple-GEM detector that is illuminated through a pin-hole. The first question we want to answer is this instrument capability to detect an event, in our case, to convert photons into electrons. If we take into account the distance between the radiation source (the sample under analysis) and the detector (in our case 20 cm of air) and that we are using a 50  $\mu$ m kapton window, almost no radiation below 3 keV is going to be detected. The drift region is the detector active part, the gaseous volume where photons are going to be converted into charge carriers and we performed our MC simulation for two different cases (configurations) one with 1 cm and another 3 cm.

The efficiency curves for the 3 different gases, Ar/CO<sub>2</sub> (70/30), Ne/CO<sub>2</sub> (90/10) and Kr/CO<sub>2</sub> (90/10), can be found in figure 6.1. This efficiency already takes into account the distance between the sample and the detector and the kapton window transmission. The

curves were obtained using the transmission and absorption data tables from [52].

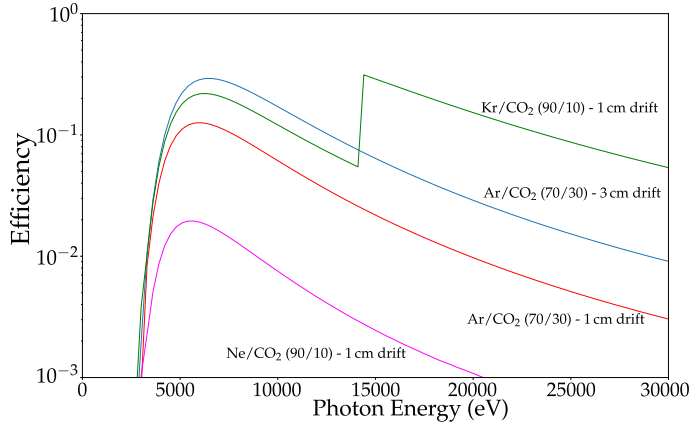


**Figure 6.1:** Conversion efficiency for three different noble gaseous mixtures for the detector configurations describe in the text.

The first thing to be noticed is the low efficiency of neon, being approximately one order of magnitude smaller than the other gases. Despite the low efficiency, neon may be an interesting gas because it has the advantage of producing an escape peak convoluted with the main characteristic radiation peak (neon fluorescence  $K_{\alpha} = 0.848$  keV [53]), and so, it will not produce additional peaks in the energy spectrum impairing the identification of elements (a discussion regarding the production of escape peaks will be presented in section 6.2). Along with a pinhole geometry, the count rate in a detector with neon is going to be very low, therefore, its use is recommended if the flux of photons is high enough. One can see that for the same drift region thickness, both krypton and argon have initially, and for lower energy, an efficiency that is relatively close to each other, however, due to the absorption K-edge, above 15 keV krypton shows a by far larger efficiency.

Since we are building a gaseous detectors to measure the energy dispersive spectrum, one of the most important parameters is the energy resolution. Due to statistical fluctuations higher energies, which are going to produce a larger amount of charge, have better energy resolution. Using Garfield++[14], more specifically the HEED library[54], we are capable to simulate the detection of a mono energetic photons, interacting inside a gaseous volume filled with either Argon or Krypton mixtures. We do not simulated neon since both this gas is not available in our laboratory and, even if we manage to have it, the relative low photon flux we usually work with will results in an unbearable long acquisition time.

The distribution of the number of primary electrons generated by the 6 keV photons can be found in figure 6.2. These photons were thrown perpendicular to the detector plane, inside the gaseous volume of Ar/CO<sub>2</sub> (70/30) or Kr/CO<sub>2</sub> (90/10), both operating at atmospheric pressure, with dimensions of 10 cm length,  $\times$  10 cm width  $\times$  1 cm height. The number of

primary electrons is directly proportional to the energy deposited in the drift region, hence the energy of the incident X-ray photons. The secondary peak in the plot on the left is the argon escape peak. Until 15 keV, krypton will not produce a prominent escape peak due to the energy of its fluorescence emission. This effect, which can be an advantage, is going to be discussed further in this chapter.

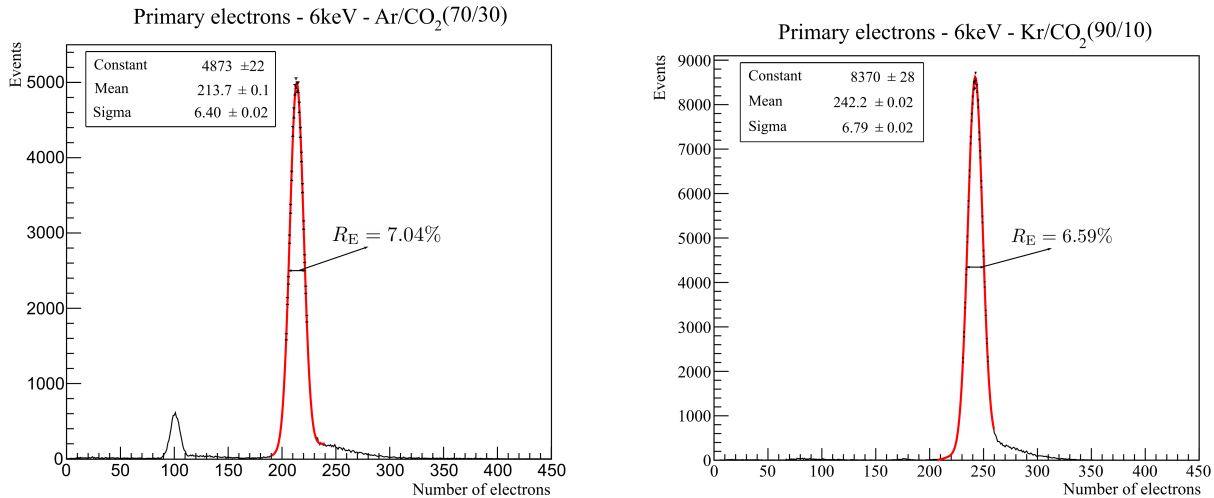


**Figure 6.2:** Number of electrons generated per event at the drift region by mono energetic photons with 6 keV.

The primary electrons count fluctuation is caused due to statistical Poisson processes and since the event that creates charge carriers is not completely independent, there is a correction to deal with the deviation of the distribution, which is called Fano's factor [4]. The energy resolution limit of a detector can be estimated using the following equation:

$$R_{\min} = 2.35 \sqrt{\frac{Fw}{E_x}} \quad (6.1)$$

where  $F$  is the Fano's factor for the medium,  $w$  is the work function and  $E_x$  the energy of the incident radiation. This is why solid state detectors will have better energy resolution due to their low energy requirement to create a charge carrier pair in the active volume, which increases number of carriers and consequently reduces statistical deviation. However, this is not the only effect which degrades the energy resolution. Due to the Townsend multiplication mechanism which is in charge of signal amplification in a gaseous detector, the energy distribution becomes wider. Figure 6.3 shows a simulation of the effective gain distribution obtained with a single GEM detector for different voltages. The drift field ( $E_d$ ) was set to 400 V/cm while the induction field ( $E_i$ ) kept at 4000 V/cm.

Using the probability density function (PDF) obtained in figure 6.3 we can use the histogram of primary electrons of figure 6.2 and by applying a MC method to draw values, obtaining a spectrum after multiplication, which can be seen in figure 6.4.

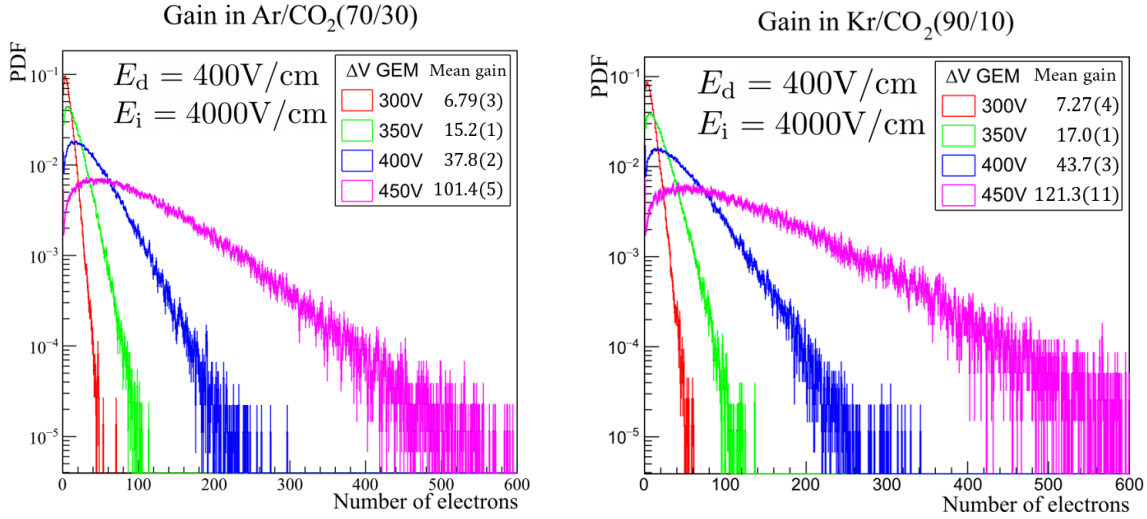


**Figure 6.3:** Gain distribution as a function of the voltage applied on the GEM electrodes. One can see that the dispersion is wider for higher voltages.

It is possible to notice the energy resolution degradation after multiplication. We have made the same procedure for two and three GEM foils, however, no considerable difference in the energy resolution could be found. The value obtained is important since it shows the best energy resolution that can be achieved, ignoring other effects such as electronic noise. Using Ar/CO<sub>2</sub>, operating at atmospheric pressure, the minimum value that can be achieved is close to 7% and if one uses a structure such as GEMs to increase the signal, which is mandatory to obtain a charge value above de intrinsic electronic noise, the value goes to 15%, which can difficult the identification of elements that are neighbors in the periodic table, in the case of using such detector for X-ray fluorescence (XRF) or particle induced x-ray emission.

The main advantage of applying higher voltages across the GEM foil is to improve the signal-to-noise ratio after electronic processing. This factor is one of the most important parameters to be improved in a detection system, however, it is possible to see that the mechanism itself, that makes our signal higher is also limiting our detection capability. The same effect was simulated in Kr/CO<sub>2</sub>(90/10) and since the Fano's factor for Krypton[55] and Argon[56] are similar, and also the effective gain achieved[57], the resolution degradation was alike the one present in figures 6.2, 6.3 and 6.4.

## 6.2 Photon escape probability

In both figures 6.2 and 6.4 we can notice the escape peak. It is generated when the total energy of an event is not completely deposited inside the detector. The secondary photon, emitted by the atom de-excitation, may not interact inside the gaseous volume and this energy is lost. Therefore, for each fluorescence line detected, an escape peak is expected, generated in a very

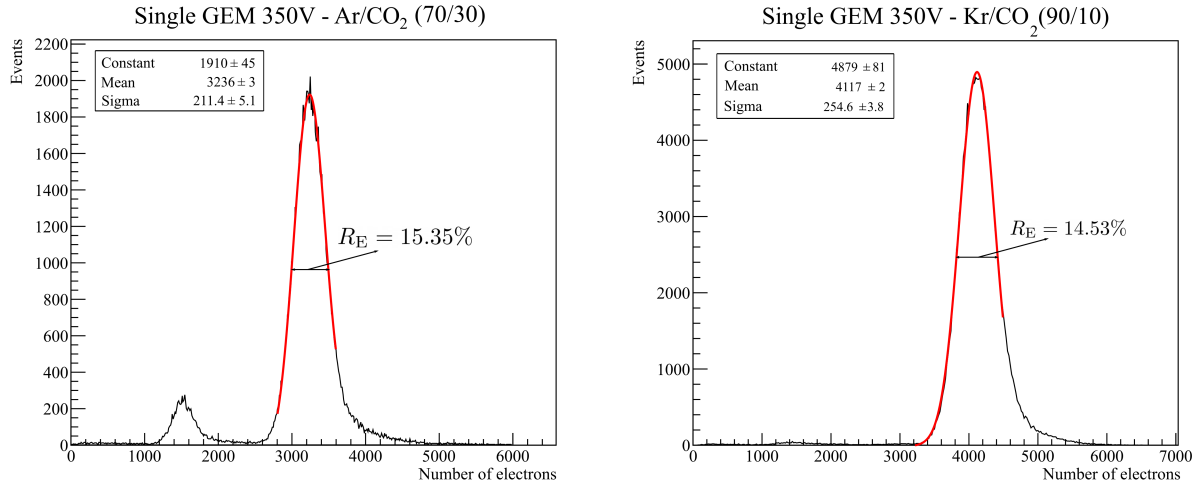


**Figure 6.4:** Number of electrons generated per event at the drift region by mono energetic photons with 6 keV after multiplication done by one GEM.

well known position in the energy spectrum.

One problem faced when we try to identify elements by spectral analyzes is the superposition of fluorescence lines being detected and escape peaks. To study such effects, one can simulate the probability of a photon to escape as a function of the drift region gap and the type of gas used inside the detector. Two different detectors models where design, the first one with a 1 cm drift region and the second with 3 cm, both with an active area of 10 cm × 10 cm, operating with Ar/CO<sub>2</sub>(70/30) as figure 6.5 shows. To calculate the escape probability we chose a point in space that is inside the drift volume and we throw for each point 10<sup>4</sup> photons (generated isotropically), covering the solid angle of  $\Omega = 4\pi$ . By analytical methods, the total length traveled inside the gaseous medium was calculated and using this length we can obtain the probability of escape for this photon, calculated using the Lambert-Beer equation2.5.

The escape probability for a photon of 3 keV(argon fluorescence energy [53]) can be seen in figure 6.5. One can notice that the escape probability drops just by increasing the drift region by a factor of 3. Also, by increasing the argon concentration in the mixture we can decrease the escape probability for the whole detector as figure 6.6 shows. However, increase this proportion may affect other parameters such as gain and operation stability in undesirable ways. The main factor that contribute to the result shown in figure 6.6 is that the interaction cross-section for photons of 3 keV is higher in argon than in carbon dioxide [19].

Lastly, if there is the necessity to work with shorter drift lengths, one alternative is to change the noble gas of the mixture. Krypton only emits the  $K_{\alpha}$  line if it is ionized by radiation with energy higher than 14 keV. For lower energies, the  $L_{\alpha}$  transition emits a photon with 1.59 keV [53]. Since this energy is lower, the probability to reabsorb this photons is higher, depositing the complete energy of the event in the gas. Figure 6.7 exemplifies it.

One can see that with the same geometry it is possible to reduce drastically the escape

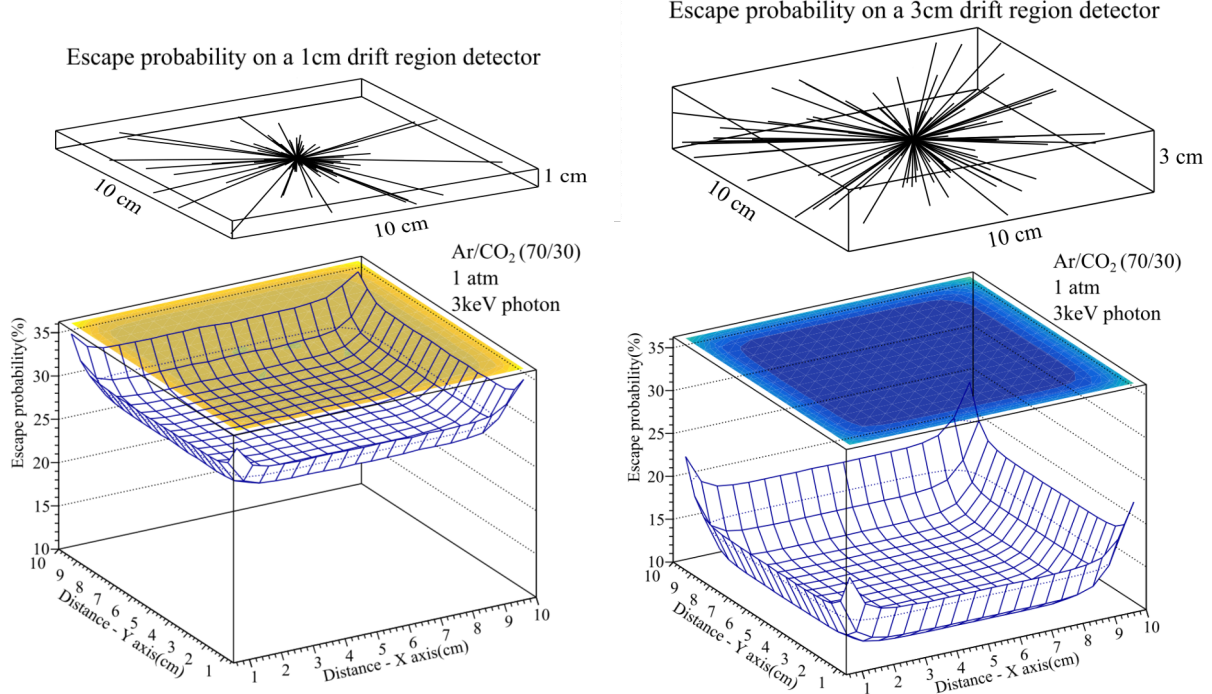


**Figure 6.5:** Escape probability along the Z-axis for two different detector geometries operating with Ar/CO<sub>2</sub> at atmospheric pressure. One can notice that the mean value at the center of the detector for the drift region of 3 cm is substantially lower.

probability. The use of krypton may be interesting for X-ray fluorescence gaseous detectors since it reduces the contribution of secondary escape peaks to the energy spectrum, however other factors need to be considered such as spatial resolution, energy resolution and quantum efficiency.

### 6.3 Copper background contamination.

One of the challenges of using GEMs for X-ray fluorescence imaging is the copper background contamination generated by its electrodes. Part of the radiation that does not interact in the drift region may hit a copper electrode of the GEM or the read-out and end up generating a fluorescence. This radiation may go towards the active area and be detected as an event. The copper has a K fluorescence emission at 8.05 keV [53], which is closely to the efficiency peak of our system, as we can see in figure 6.1. As we have calculated previously, the energy resolution limit for our detector is at the order of 15% in this energy range and the presence of this peak may jeopardize the identification of elements.

Figure 6.8 exemplifies how the contamination may happen. The photon coming from the radiation source or sample, is not going to interact with the active volume of the detector and will end hitting a copper electrode interacting at a depth  $y$ . If a fluorescence is triggered and a

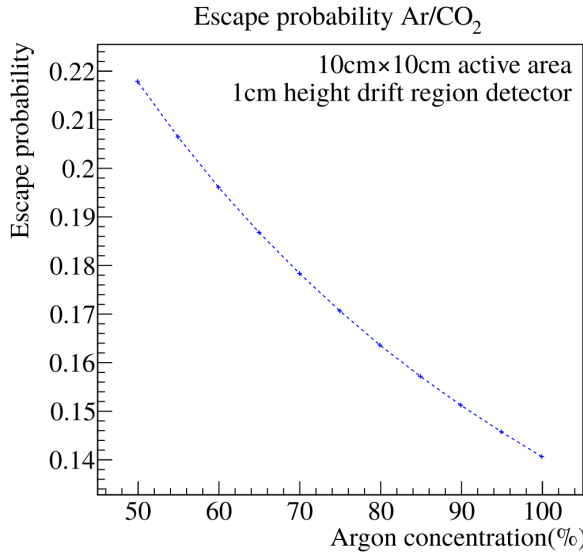


**Figure 6.6:** Escape probability as a function of argon concentration in the gaseous mixture with carbon dioxide.

photon emitted towards the drift region, it can be absorbed and deposit its energy in the gas, generating a copper peak that does not come from the sample but is intrinsic to the system if it is irradiated by energies above 8 kV.

To estimate the contribution of the copper contamination generated and detected by our own system, we have studied and complemented a model that is widely used in XRF spectroscopy field [58, 59]. The idea is to calculate the contribution for each copper electrode inside our detector and latter sum all of them.

The normalized intensity  $dI_k$  of the spectral line  $K_\alpha$  of copper, emitted by the infinitesimal thin copper layer  $dy$ , can be expressed as following :

$$dI_k(\nu_i, \nu_f) = \frac{dI(\nu_i, \nu_f)}{I_0} \propto \frac{d\Omega}{4\pi} \omega_k \frac{1}{\lambda_k(\nu_i)} \exp \left[ - \left( \frac{y}{\lambda_{Cu}(\nu_i)} + \frac{z}{\lambda_{Cu}(\nu_f)} \right) \right] dy \quad (6.2)$$

The first exponential term gives the intensity of the beam (with energy  $\nu_i$ ) that reaches the infinitesimal layer of copper( $dy$ ) after traveling a copper length of  $y$ . The second exponential is the attenuation of the fluorescence photons (with energy  $\nu_f$ ) that are generated inside this same infinitesimal layer and that pass through a total length of  $z$  inside the copper. The term  $\frac{1}{\lambda_k(\nu_i)}$  is related to the differential probability of photon fluorescence emission and takes into account only interactions which generate K-shell vacancies. At a first approximation the difference between the attenuation length using all the electronic shells or only the K-shell is small [60] and can be neglected, that is,  $\frac{1}{\lambda_k(\nu_i)} \approx \frac{1}{\lambda_{Cu}(\nu_i)}$ . The fraction  $\frac{d\Omega}{4\pi}$  will give the solid angle of the fluorescence emission and  $\omega_k$  is the fluorescence yield, that is, the probability of the K-shell vacancy be filled through radiative processes. The value used was 0.433, obtained through the fit in [61].

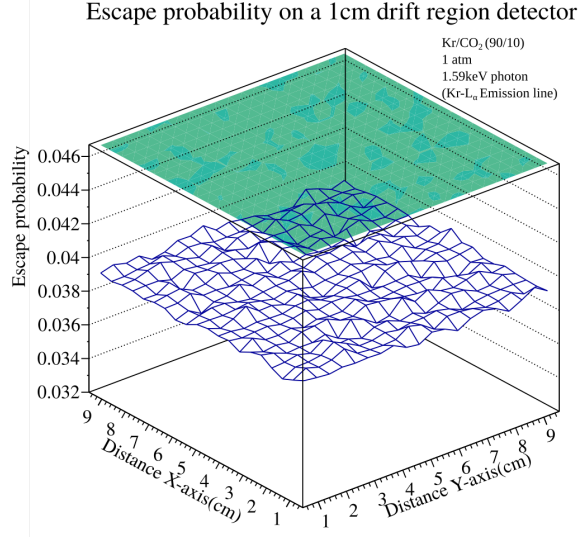


**Figure 6.7:** Escape probability along the Z-axis for a 1 cm drift region gap detector filled with Kr/CO<sub>2</sub>. The escape probability is one order of magnitude lower than the one with argon.

Two extra terms need to be added into this equation. The first is related to the beam attenuation until interaction with the copper cladding. The second is the probability of detection of the fluorescence photon by the drift region. Writing  $z = \frac{y}{\cos(\theta)}$ , we obtain the following:

$$dI_k(\nu_i, \nu_f) = \frac{d\Omega \gamma(\nu_i) \omega_k}{4\pi \lambda_{Cu}(\nu_i)} \exp \left[ - \left( \frac{y}{\lambda_{Cu}(\nu_i)} + \frac{y}{\lambda_{Cu}(\nu_f) \cos(\theta)} \right) \right] \left( 1 - \exp \left[ \frac{-D}{\lambda_{Ar}(\nu_f) \cos(\theta)} \right] \right) dy \quad (6.3)$$

where  $D$  is the drift region thickness,  $\lambda_{Ar}(\nu_f)$  is the argon attenuation length and  $\gamma(\nu_i)$  is the term related with the attenuation by the different materials which the photon beam may interact before going through the copper layer (that is, the air column between the source and the detector and the window and drift region transmission) and is energy dependent ( $\nu_i$ ). The total intensity calculated only for the first copper layer of the first GEM is given by:

$$I_k(\nu_i, \nu_f) = \frac{\gamma(\nu_i) \omega_k}{4\pi \lambda_{Cu}(\nu_i)} \int_0^{2\pi} d\phi \int_0^{\frac{\pi}{2}} d\theta \sin(\theta) \int_0^d dy \exp \left[ - \left( \frac{1}{\lambda_{Cu}(\nu_i)} + \frac{1}{\lambda_{Cu}(\nu_f) \cos(\theta)} \right) y \right] \left( 1 - \exp \left[ \frac{-D}{\lambda_{Ar}(\nu_f) \cos(\theta)} \right] \right) \quad (6.4)$$

Integrating over the copper thickness  $d$  and in the  $\phi$  angle we get:

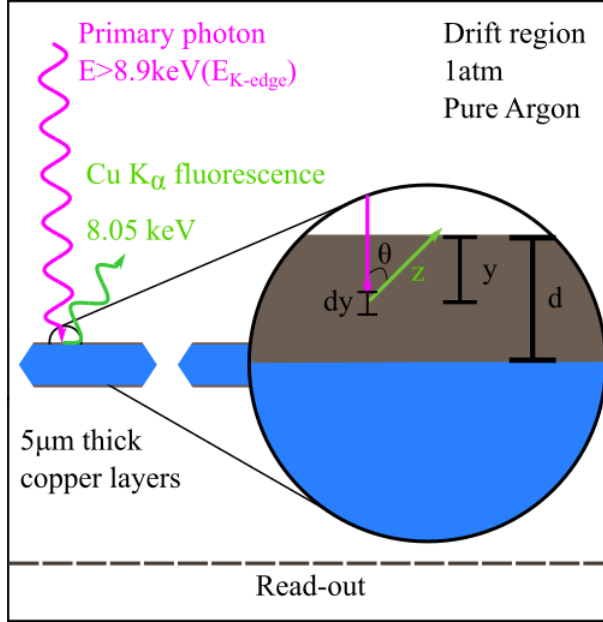


**Figure 6.8:** How the copper contamination takes place inside the detector, in this specific case, at the top layer of the GEM foil.

$$I_k(\nu_i, \nu_f) = \frac{\gamma(\nu_i)\omega_k}{2\lambda_{Cu}(\nu_i)} \int_0^{\frac{\pi}{2}} d\theta \sin(\theta) \frac{1}{\frac{1}{\lambda_{Cu}(\nu_i)} + \frac{1}{\lambda_{Cu}(\nu_f)} \cos(\theta)} \left( 1 - \exp \left[ - \left( \frac{1}{\lambda_{Cu}(\nu_i)} + \frac{1}{\lambda_{Cu}(\nu_f) \cos(\theta)} \right) d \right] \right) \left( 1 - \exp \left[ \frac{-D}{\lambda_{Ar}(\nu_f) \cos(\theta)} \right] \right) \quad (6.5)$$

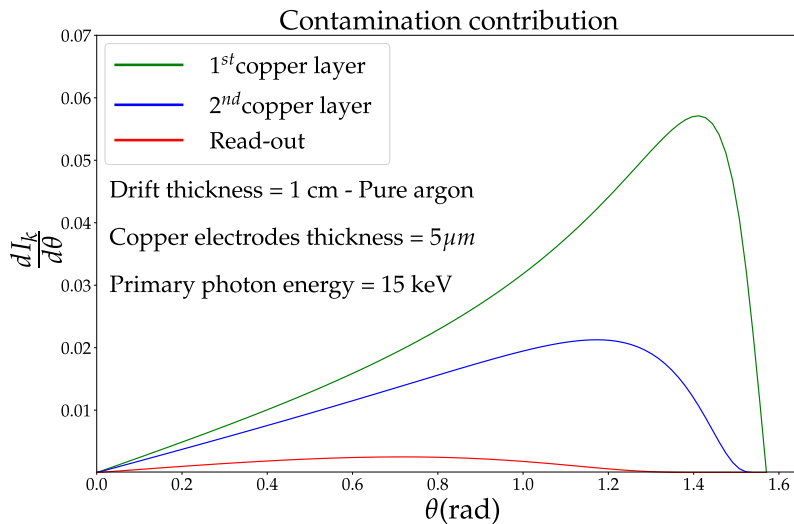
or

$$I_k(\nu_i, \nu_f) = \frac{\gamma(\nu_i)\omega_k}{2} \int_0^{\frac{\pi}{2}} d\theta \sin(\theta) \frac{a}{a + b \cos(\theta)} \left( 1 - \exp \left[ - \left( a + \frac{b}{\cos(\theta)} \right) d \right] \right) \left( 1 - \exp \left[ \left( \frac{-Dc}{\cos(\theta)} \right) \right] \right) \quad (6.6)$$

where  $a$ ,  $b$  and  $c$  are  $\frac{1}{\lambda_{Cu}(\nu_i)}$ ,  $\frac{1}{\lambda_{Cu}(\nu_f)}$  and  $\frac{1}{\lambda_{Ar}(\nu_f)}$  respectively.

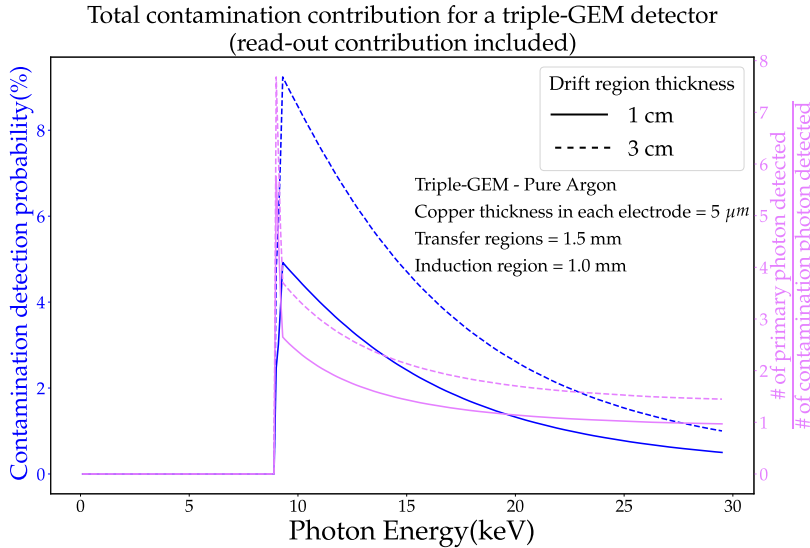
This integral can be solved numerically however, we have made some additional hypotheses to the problem. The first one is that the X-ray source is considered to be very far from the detector windows, this way all the photons enter the drift region perpendicular to the detector plane. This X and Y plane are also considered to be infinity in both directions. At first approximation the GEM foils holes and the space between the read-out strips where neglected. Thus, all the metallic electrodes are continuous. These hypotheses where made in order to simplify the problem and its development and future corrections and considerations may be applied. As it was said before, the equation 6.6 gives the intensity of contamination only for the first copper layer of the first GEM. To calculated the contribution of the others electrodes we have added more attenuation terms for both the incident and the contamination fluorescence photons.

Figure 6.9 show the contamination contribution for different copper parts of the detectors, calculated from equation 6.3 as a function of the fluorescence emission angle.



**Figure 6.9:** Contamination inside the detector.

It is clear that the contribution of contamination for layers which are more depth inside the detector are smaller, however, they need to be taken into account. If one integrate and sums this curves we can get the total contribution of contamination for a specific detector setup. Figure 6.10 shows the total contamination for two different systems. The first , with dashed lines, has a drift region with 1 cm, while the second has a drift with 3 cm. Both detectors have three GEMs and a read-out covered by copper. Each one of these electrodes are  $5 \mu\text{m}$  thick. The value for  $\gamma$  in the first layer calculation was kept equal to the transmission probability in the drift region and for the subsequent layers the terms related to the transmission in other components were added. The fluorescence photons also need to be attenuated by these same components after they are generated. The transfer and induction zones were 1.5 mm and 1 mm respectively.



**Figure 6.10:** Contamination detection probability (blue) e contamination fraction (magenta) for 1 cm (continuous) e 3 cm (dashed) drift thickness.

One can see that the probability to detect a contamination photon (blue curve) has its maximum just above the K-shell absorption edge and than it drops. This happens mainly due to the increase of the attenuation length for higher energy primary photons, while the attenuation length for the copper photons remains constant.

In magenta it is possible to see the number of primary photons with energy  $\nu_i$  that are detected divided by the number of contamination photons detected that were generated by photons with this same energy. The ideal is to maximize this ratio, increasing the number of primary photons which are detected, thus, the detector with thicker drift region shows more advantages in terms of lower contamination background.

One can see that the ratio between primaries and contamination photons detected is close to 1 for higher energies. A future more detailed study will investigate of this ratio, however, it is simple to think that this pollution in the middle of the spectrum may decreasing the position resolution of the detector (these photons are going to create a almost flat background in the images, decreasing the contrast over all active area) and of course, generating a extra peak at 8.05 keV and other peak at 5 keV(copper escape peak).

Different groups are working in ways to suppress the copper cladding contamination. One idea is to remove most of the copper conductive layer and to use just the adhesive tape which has chromium in its composition to active like the conductor [62]. Despite the clear contamination suppression [63], the process in which these GEM foils are produced is not clear and the chromium may also produce a contamination, although in much less intensity, in the region of interest, at 5.41 keV[53].

Another alternative is to use a different cladding for the GEM foils, replacing the copper

for another metal with same properties, however, with smaller atomic number. Aluminum may be one of the candidates, with X-ray fluorescence at 1.48 keV which will not spoil the energy spectrum in the region we are interest[64]. Figure 6.11 shows the total contribution of contamination detected by two different detectors, the first use GEMs with copper cladding and the other with aluminum. Both systems are using a copper read-out.

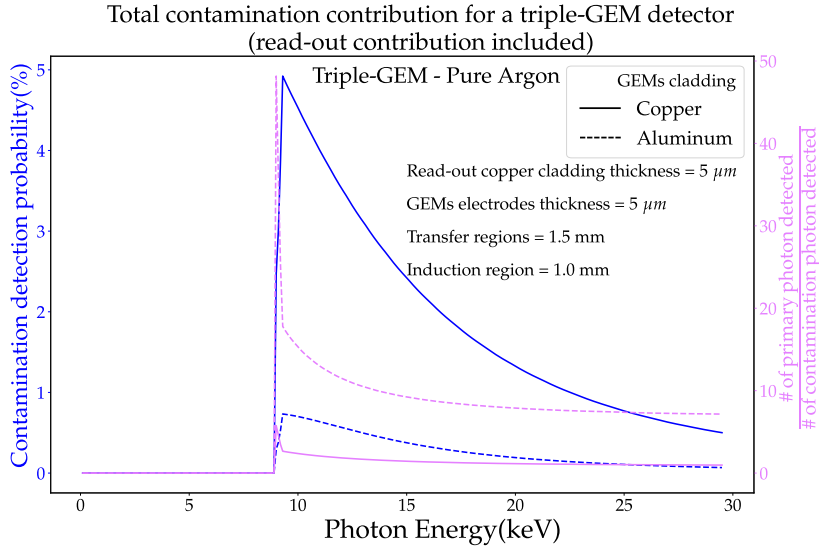


**Figure 6.11:** Copper fluorescence contamination probability of two different systems. One using GEMs with copper cladding and other with aluminum. Both systems uses a copper read-out system.

The relative dimensions were kept the same as the ones for the previous detectors. One can see that the probability to detect a contamination photon is small in the system using aluminum GEMs and also the ratio between detected primary photons and contamination ones is higher in this system. Although this is a promising result, the etching of aluminum foils may be more difficult and this electrode may show oxidation problems in a shorter time than the copper one. This calculation was made taking considering a much more simplified model of detector and sample, such as a perfectly flat sample which is parallel to the detector. In the future a more complex and realistic calculation need to be made in order to achieve a more reliable result and probably, it will need to be solved numerically and using MC methods.

## 6.4 Geometric response

One thing to be considered in the X-ray fluorescence image setup is the geometric response of the detector. Since we are using a source that does not irradiate the samples uniformly and the path that is traveled by light changes as we choose different points of the detector, the spectrum intensity on each region will be different and may interfere on a quantitative analyses.

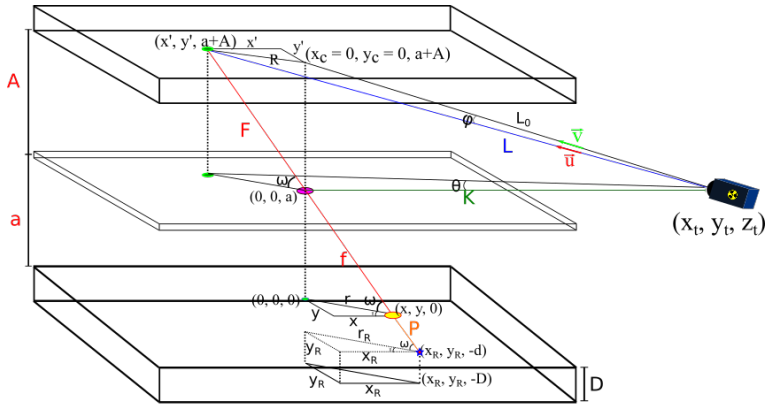


**Figure 6.12:** Geometric aspects of the detector that will interfere on the final spectrum.

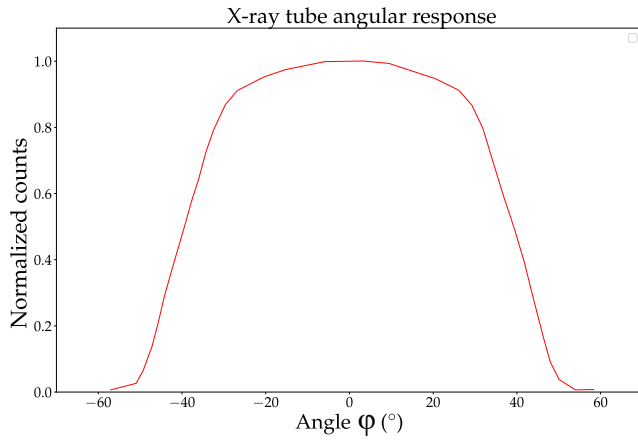


**Figure 6.13:** Intensity of the radiation emission as a function of the exiting angle  $\varphi$ . Data adapted from [65]

To calculate the response of the detector on each points of the read-out system we can work on the geometric aspects of the setup. Figure 6.12 illustrates the problem.

The origin of the coordinate system is at the middle of the detector's window, which is going to define a plane where the radiation passes before being absorbed. The detector response ( $I_R$ ) on each point is going to be a convolution of several aspects as equation 6.7 shows.

$$I_R = E_T(\varphi)P_{\text{air}}(\lambda)P_{\text{air}}(\lambda')P_{\text{win}}(\lambda')(1 - P_{\text{gas}}(\lambda')) \quad (6.7)$$

where  $E_T(\varphi)$  is the tube radiation emission intensity as a function of the exiting angle from the tube  $\varphi$  (check figure 6.13) and  $P_{\text{air}}$ ,  $P_{\text{win}}$  and  $P_{\text{gas}}$  are the transmission probability of a photon in air, the detector window and the gas respectively. The photon  $\lambda$  is the one emitted by the tube and will travel a path  $L$  and the photon  $\lambda'$  is the fluorescence photon and will travel a path  $F+f$  until it reaches the detector's window. The interaction probability can be calculated using equation 2.5, and the attenuation coefficients obtained from reference [52].

To calculate  $\varphi$  and the interaction probabilities we can use some geometry as following.

The path  $L$ , traveled by the photon  $\lambda$ , can be obtained using the tube coordinates  $(x_t, y_t, z_t)$  and the interaction point on the sample  $(x', y', A + a)$ . To calculate the emission angle, we also need the coordinate where the tube is aiming  $(x_c, y_c, A + a)$ , that is, the point in the sample where  $\varphi = 0$ .

The angle  $\varphi$ :

$$\cos \varphi = \frac{\langle \vec{u}, \vec{v} \rangle}{|\vec{u}| \cdot |\vec{v}|}$$

$$\varphi = \arccos \left( \frac{(x' - x_t)(x_c - x_t) + (y' - y_t)(y_c - y_t) + ((A + a) - z_t)^2}{\sqrt{(x' - x_t)^2 + (y' - y_t)^2 + ((A + a) - z_t)^2} \sqrt{(x_c - x_t)^2 + (y_c - y_t)^2 + (A + a) - z_t)^2}} \right)$$

To calculate the path  $F + f$ , traveled by the photon  $\lambda'$ , we need to know where it entered the detector.

We may than, use the following relations:

$$r = \sqrt{x^2 + y^2}$$

$$f = \sqrt{r^2 + a^2}$$

$$F = \frac{Af}{a}$$

The photon will be converted into charge carriers in a random point between 0 and  $D$ . In our example we are assuming the coordinate  $(x_r, y_r, -d)$ , and the electron cloud is going hit the read-out system at the point  $(x_r, y_r, -D)$ .

This coordinates can be obtained using:

$$x = \frac{a}{(a + d)} x_r$$

$$y = \frac{a}{(a + d)} y_r$$

And since we are using a pinhole geometry, this will lead to a known position of the sample:

$$x' = -x \frac{F}{f}$$

$$y' = -y \frac{F}{f}$$

Since the photon can interact at any height inside the gaseous volume, the probability needs

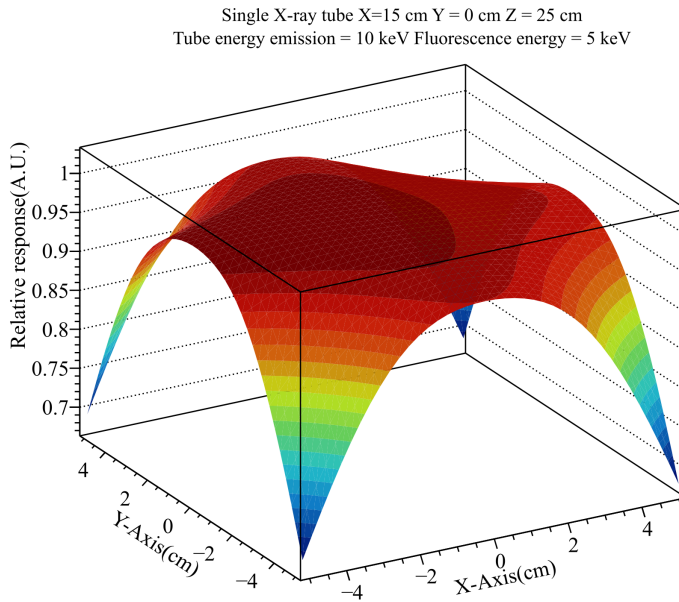


**Figure 6.14:** Normalized intensity measured by the detector for a 5 keV fluorescence photon. Sample irradiated with one X-ray tube placed on the coordinates ( $x_t=15$  cm,  $y_t=0$ ,  $z_t=25$  cm).

to be integrated over the thickness  $d$ .

As a result of this calculations we may use the equation 6.7 and look at the geometric response of the detector

Figure 6.14 shows the normalized response of the detector only as a function of geometric aspects. In this example one X-ray tube was placed on the coordinates ( $x_t=15$  cm,  $y_t=0$ ,  $z_t=25$  cm), the distances  $A=a=20$  cm, the detector drift region was set to 1 cm. The tube was aiming at the center of the sample. The simulated tube emitted a mono energetic 10 keV radiation beam. The fluorescence was also considered monochromatic, emitting 5 keV photons.

It is possible to see a large difference in the relative intensity measure by the detector just do to geometric aspects. This will lead to discrepancies in the energy spectrum if one measures the same uniform sample using different areas of the detector. To mitigate these problems, a simple thing that can be done is to rotate either the sample or the X-ray tube, however, it will increase the acquisition time. One alternative to mitigate this situation is to use two X-rays sources to irradiate a sample.

Looking at figure 6.15 we can see the effect in the uniformity of the irradiation when two X-rays tubes are used, one at the coordinates ( $x_t=15$  cm,  $y_t=0$ ,  $z_t=15$  cm) and the other on ( $x_t=-15$  cm,  $y_t=0$ ,  $z_t=15$  cm). The relative intensity deviation was reduced and the illumination in the central area of the sample and consequently detector is almost constant. Another method that can be used to suppress the non-uniformity is to create a post-processing data analysis that will correct the intensity of the energy spectrum for a specific region of the detector. To do so a more detailed simulation needs to be made, taking into account the emission

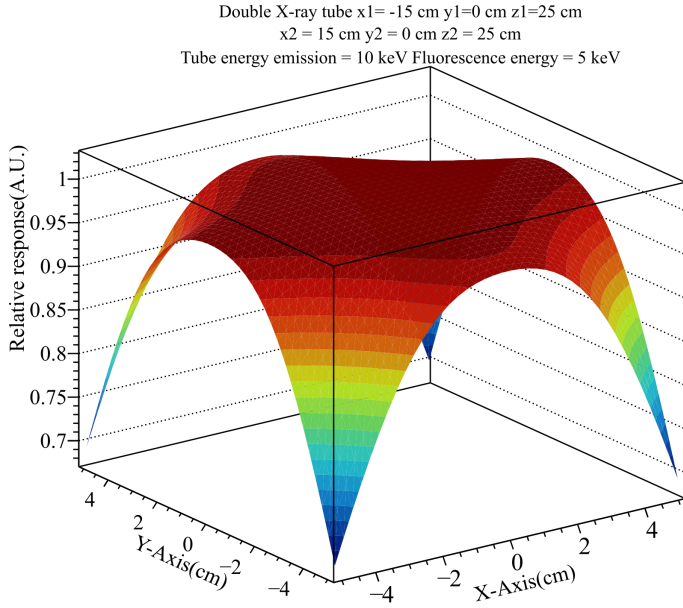


**Figure 6.15:** Normalized intensity measured by the detector for a 5 keV fluorescence photon. Sample irradiated with two X-ray tubes one place one at the coordinates ( $x_t=15$  cm,  $y_t=0$ ,  $z_t=15$  cm) and the other on ( $x_t=-15$  cm,  $y_t=0$ ,  $z_t=15$  cm).

curve of the X-ray tube and also the elements present in the sample needs to be identified to obtain both information about the energy of fluorescence and also the fluorescence yield.

## 6.5 Simulating a read-out system and reconstruction algorithms

Along with the development of the structures in charge of the electron multiplication, other parts of the detector, such as the read-out system are being studied and updated constantly.

For a bench top and portable detector the strip-like readout has a major advantage in terms of pixel size to electronic channels, however, they start to show limitations when an excessive number of events comes at the time window. If one or more interaction happens to a same set of strips but in different positions, part of the information is lost and strange artifacts may appear in the image. Optical read-outs can mitigate such effects and they are being used to reduce the image acquisition time and distortion [66]. These read-outs are able to collect directly the photons generated after a avalanche when using the proper gas mixture, normally a composition containing  $\text{CF}_4$  [41] or other gases with wavelength shifters. Although they may compose the next generation of gaseous detectors assemble, with the cost of such devices today, cheap detectors are unable to have such structures.

Studies showing different types of strip-like read-out, such as zig-zag strips have been made

for 1-D (mainly to measure with more precision the  $\phi$  coordinate and consequently the transversal momenta)[67][68]. In the following sections we are going to discuss intrinsic problems and challenges that are faced when using strip read-out systems.

### 6.5.1 Strip read-out system

One of the main types of read-out systems for detectors with high sensitive area is the strip read-out. It consists of two stacked planes of parallel conductive strips, rotated by  $90^\circ$ , one being perpendicular to another. The charge is collected independently for each strip and the signal is processed by a standard chain of preamplifier, shapers, discriminators and an analog-to-digital converter. To recreate the interaction point a center of mass algorithm is used as illustrated in figure 6.16.

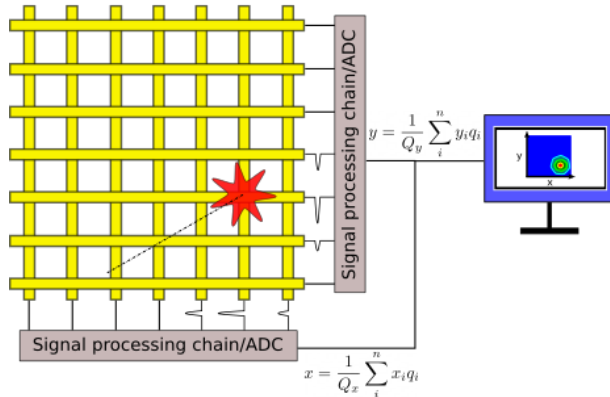


**Figure 6.16:** Example of segmented read-out system.

With strips crossing each other it is possible to create virtual pixels that have approximately the size of the read-out pitch. This is an advantage when compared to the pad read-out since a lower number of electronic channels will be needed to cover the same area. Since we are reading a continuous distribution of charge with a discrete system, we add a position dependent systematic error. To estimate the errors and to minimize the artifacts that may appear in our image we have conducted several simulations that take into account the parameters shown in figure 6.17, such as the electron cloud diffusion ( $\sigma$ ), the read-out pitch and the strip width. In the simulation we have included a read-out response function, that will collect all the charge that hits a strip and will not take into account the electrons that hits the read-out plane between two adjacent strips. Several additional features such as noise and the application of zero suppression algorithm, i.e. removing from the center of mass algorithm the strips where the charge does not reach a minimum threshold value can be applied, as figure 6.18 shows.

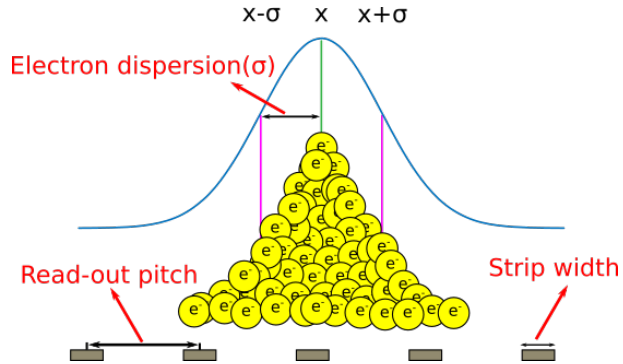


**Figure 6.17:** Simulation parameters that can be changed in order to study the precision of a segmented read-out system.

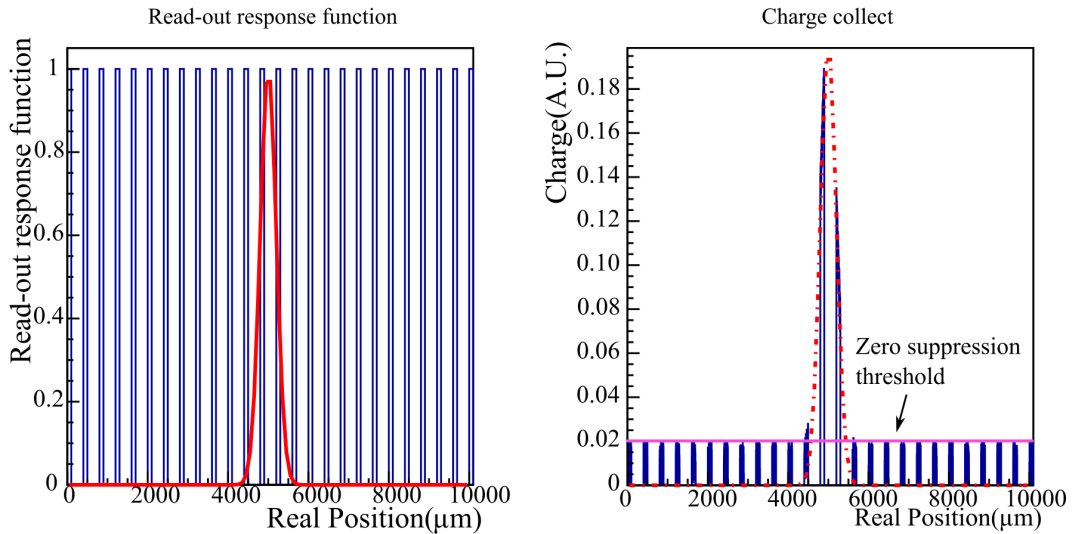


**Figure 6.18:** Left: Read-out response function. In red is possible to see where the charge distribution hit the read-out. Right: Charge collected and noise in each strip. The pink line indicates the zero suppression threshold.

By using the center of mass algorithm we can reconstruct the interaction position, using parameters that are similar to the ones used in our laboratory (strip width = 100  $\mu\text{m}$  and pitch = 400  $\mu\text{m}$ ). The center of mass is given by:

$$x = \frac{\sum x_i q_i}{\sum q_i} = \frac{\sum x_i q_i}{Q} \quad (6.8)$$

where  $q_i$  is the charge collected by the strip  $i$ , located at the point  $x_i$ .

Since we know the exactly the simulated electron cloud center, we are able to calculate the reconstruction error, which can be defined as:

$$\epsilon_x = x_r - x_c \quad (6.9)$$

where  $x_r$  is the real position and  $x_c$  is the reconstructed position.

We may also define the error for 2D images, which will be:

$$\epsilon_r = \sqrt{(x_r - x_c)^2 + (y_r - y_c)^2} \quad (6.10)$$

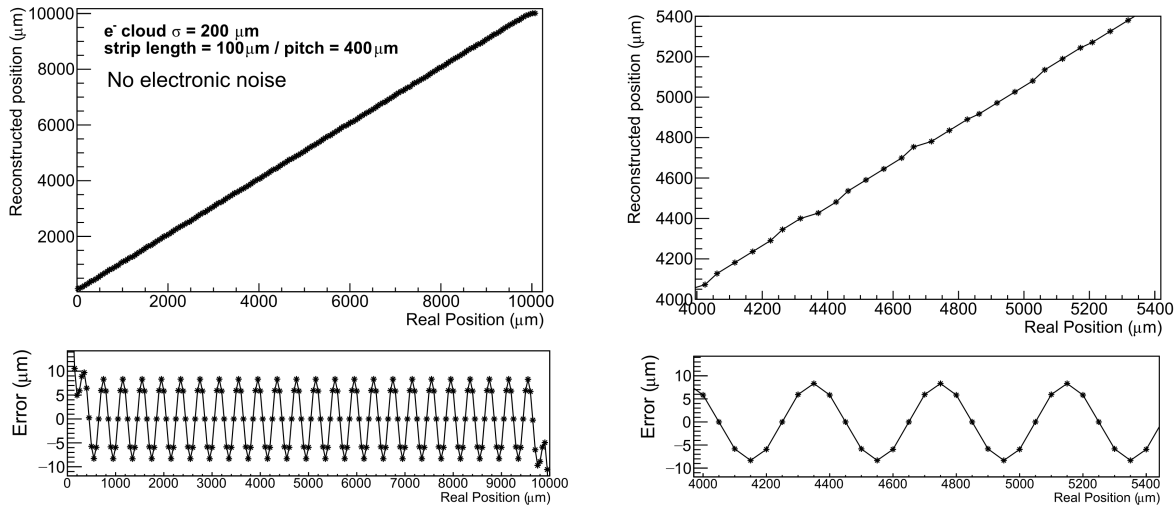


**Figure 6.19:** Left: One-dimensional reconstructed position of the interaction point as a function of the real position. Right: Zoom in of the left image.

In figure 6.19 we show a plot of the one-dimensional reconstructed position as a function of the real interaction point for  $\sigma = 200 \mu\text{m}$ . Taking a closer look to the error, we can see that it has a clearly periodicity and it will induce a specific artifact to images reconstructed, the mesh artifact.

We can use an extension of the same code to create images for 2 dimensions. In figure 6.20 we can see a set of reconstructions of the same data set. The image shown in A, denoted as the 'real image' is the distribution of the real position of the interaction points in the detector. The read-out strip mesh artifact can be clearly seen in figure 6.20-B. In this case the the high luminosity circle is completely affected. Figure 6.20-C shows a result that is similar to the one obtained in the laboratory, where the image reconstruction is not perfect but the main aspects of the sample are present and its identification is not compromised, nevertheless we can see the read-out pattern shadow and a modulation in the profile. Figure 6.20-D shows shows that for large widths of the charge clouds, the read out pattern is not a problem, due to the large multiplicity of strips. Therefore, it is important to remember that the effect of using a high zero suppression threshold to cancel noise may worsen the image reconstruction, leading to low strip multiplicity and an increase of artifacts.

One method that is widely used to characterize image detectors is the modulation transfer function (MTF)[69]. In this method the contrast of the image is measured for different spatial frequencies and by looking at its values it is possible to define the system resolution. If the read-

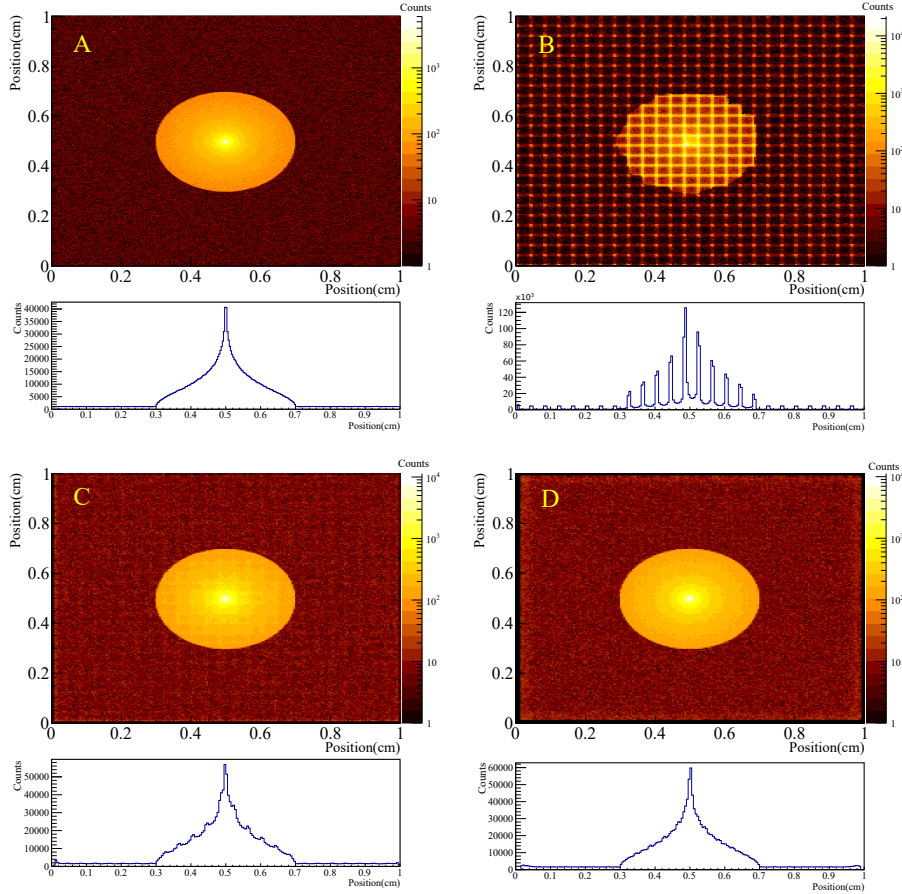


**Figure 6.20:** A: Real image. B: Electron cloud with  $\sigma = 100 \mu\text{m}$ . C: Electron could with  $\sigma = 200 \mu\text{m}$ . D: Electron could with  $\sigma = 300 \mu\text{m}$ . One can see that by increasing the dispersion of the electron cloud and consequently the strip multiplicity the artifacts vanishes.

out pattern creates a modulation in the whole image, the result of the test of characterization is affected leading to an incorrect determination for the position resolution.

Since this error is intrinsic to the measurement and can only be reduced and but not completely eliminated, one thing that can be done is a post processing analyses called flat field correction.

### 6.5.2 Flat-field correction algorithm for strip read-outs

The flat field correction is an algorithm used to improve the quality of digital images by leveling the sensibility of pixels. This method is used to calibrate many different imaging systems such as telescopes lens, CCDs devices[70] and in microscopes[71]. In our experimental setup we do not have pixel structures, however, the intersection of strips will create a pixel like structure, with roughly the same size of the strip pitch. For simplicity, in this section we are going to refer to these structures just as pixels.

The method consists into illuminating the detector evenly, generating a flat field image.

Later, after making an image of the desired sample, we divide it by the flat field image, normalizing the brighter and darker pixels. In the general formula, the counts in each pixel are going to be the sum of background, noise and a convolution between the light intensity distribution and the pixel sensitive[71]. Since in our detector we have a specific gain variation that follows the read-out pitch, we can use a slightly different algorithm that takes into account not individual pixels but the complete projection over a direction. The use of the profiles, instead of the 2D distributions for the flat field corrections takes advantage of improving the correction due to the better statistical quality of the 1D profiles.

To obtain the correction parameter ( $C(i, j)$ ) for a pixel with bin coordinate  $i$  and  $j$ , first we need to create two 1-D projection histograms of the flat field image,  $P_x$  and  $P_y$ . Then, we need to get the number of entries in each bin of these histograms( $N_x(i)$  and  $N_y(j)$ ) and the average number of entries over all bins from the projection histograms( $\bar{N}_x$  and  $\bar{N}_y$ ). The parameter then can be obtained using the following equation:

$$C(i, j) = \frac{N_x(i)}{\bar{N}_x} \frac{N_y(j)}{\bar{N}_y}$$

$$\bar{N}_x = \frac{\sum_{i=0}^A N_x(i)}{A}, \bar{N}_y = \frac{\sum_{j=0}^B N_y(j)}{B}$$

where A and B are the number of bins for the projection histograms  $P_x$  and  $P_y$  respectively. Afterwards, a new image can be generated using where the entries in each pixel will be:

$$N'(i, j) = \frac{N(i, j)}{C(i, j)}$$

where  $N(i, j)$  is the old number of entries for the pixel with coordinate  $i$  and  $j$ .

A simulation was made in order to show this principle. Using the same read-out simulation from the previous section, we have generated the flat field image (left image of fig. 6.21). We have also simulated a 'sample' with our model, a round object which will appear with higher intensity. It is possible to see that after applying the algorithm, the read-out pattern barely visible. One thing that has to be noticed is that the coordinates of the interaction are still wrong. When we look at the residual graph of figure 6.19 we can notice it. So, the flat field correction will affect only the intensity of each bin of the 2-D histogram and will not change anything in the coordinate of the event.

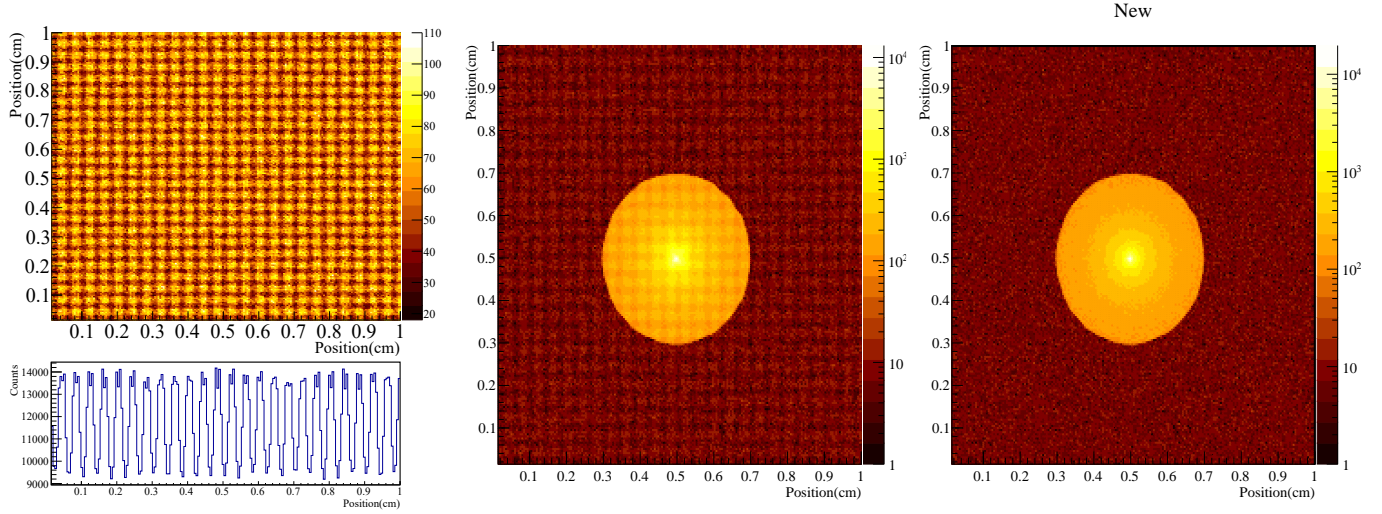


**Figure 6.21:** Left: Flat field image. Middle: Image before correction. Right: Image after applying the correction algorithm: the read-out pattern is barely visible.

We can apply the same algorithm to data obtained with the SRS system, as figure 6.22 shows. The detector was irradiated using an  $^{55}\text{Fe}$  source, placed 10 cm above the window. In this specific case, we have applied the correction factor to the flat field image itself.

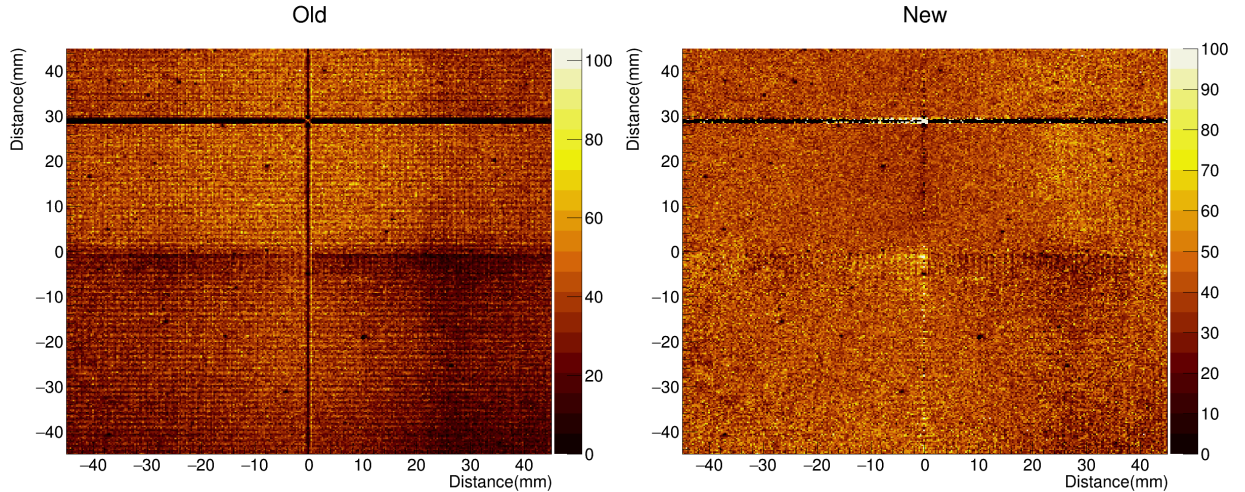


**Figure 6.22:** Left: Image reconstructed. The dark lines at  $x = 0$  mm and  $y \approx 30$  mm are dead strips. Right: Same data set image after applying the flat field correction algorithm.

Figure 6.23 shows the projections along the X and Y axis of figure 6.22:

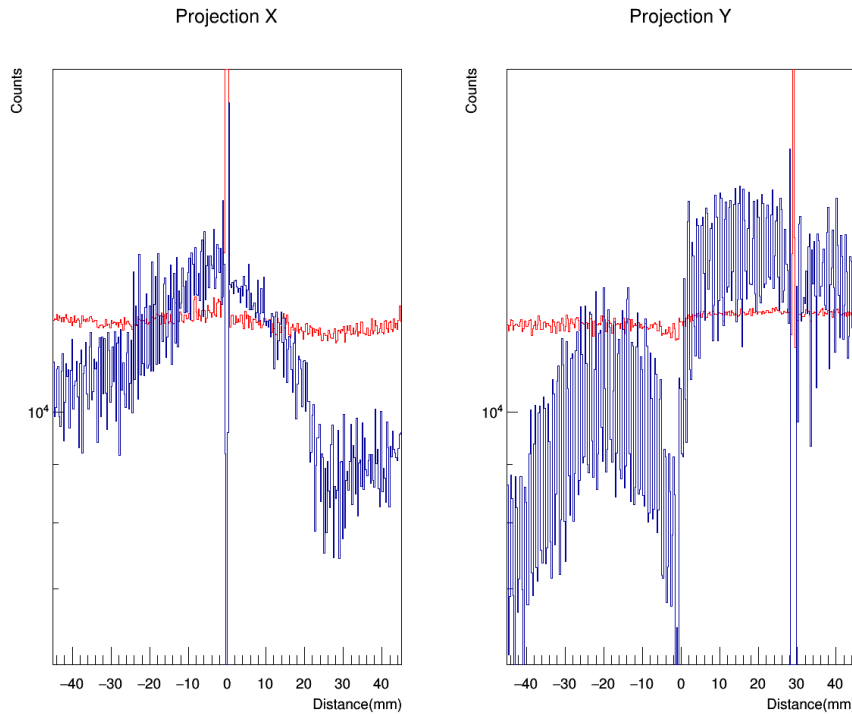


**Figure 6.23:** Profile of the image 6.22. The blue line represent the total counts integrated over one axis. The red line shows the profile of the same image after applying the correction.

It is possible to see that the read-out pattern is almost completely removed from the image, however, a small part of it can be seen close to the central strips of the detector. Each quarter of the detector is read by a different APV25 chip and so, larger counting differences between quadrants are expected, spoiling the algorithm behavior in these middle regions.

## 6.6 Ion back-flow reduction

The ion back-flowing towards the cathode after an avalanche may limit the detector operation and lifetime of certain structures, such as the photocathodes with low electron emission threshold[72]. One way to search for possibilities to reduce the ion back-flow is by simulating new structures. Other alternative is by changing the electric field configuration inside the detector. In the next sessions the reader is going to find two different ongoing works studying modifications to the standard configuration of GEM detectors in order to optimize the charge transport inside the detector.

### 6.6.1 New geometries

Different groups are studying ways to reduce the ion back-flow by changing the electrodes' displacements and configurations. One approach is to use graphene layers on the top GEM

electrode (above the holes), allowing the passage of electrons but blocking the ions[73]. Although very promising, the graphene deposition technique is not simple and it can create low resistance contacts between the GEM electrodes, preventing the capability to apply suitable and stable voltage values across the detector. Another alternative is to create a foil with an extra electrode. It can be a mesh in a middle of a Thick-GEM for example[74], or it can be a continuous conductive layer, placed in the middle of the kapton and just by doing a standard etching process, a extra electrode is created. The idea of adding additional electrodes is to change the dipole electric field configuration inside the GEM hole and allowing more the passage of electrons than the ions.

We have created two different alternatives for copper electrodes configurations and, to study how that affects electron and ion transport, we have conducted several simulations using Garfield++. Figure 6.24 shows these two configurations. The one on the left, called SD-GEM (sandwiched electrode) presents a third electrode placed slightly below the geometrical center of the dielectric layer. It was designed this way since the amount of positive charge that is generated inside the GEM hole is not symmetric, but it is more probable to be generated closer to the bottom electrode. In the right image we can see the TP-GEM (triple electrode) configuration, where a Micromega mesh(MM) is glued in the top of a GEM foil, which has the same pitch, but a smaller hole radius.

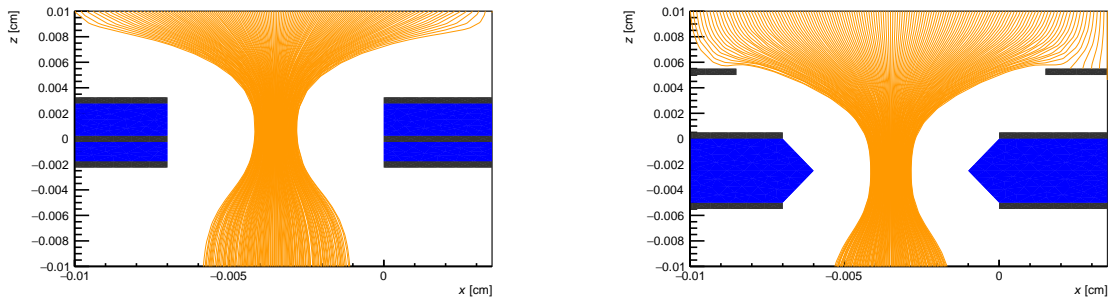


**Figure 6.24:** Left: The SD-GEM, a multi-layer GEM with a extra electrode in the middle of the dielectric foil. Right: The TP-GEM, a GEM with a Micro-Mesh on the top of it.

The electron collection efficiency and charging up effect, that is, the accumulation of charge at the dielectric, for these two structures can be seen in figure 6.25.

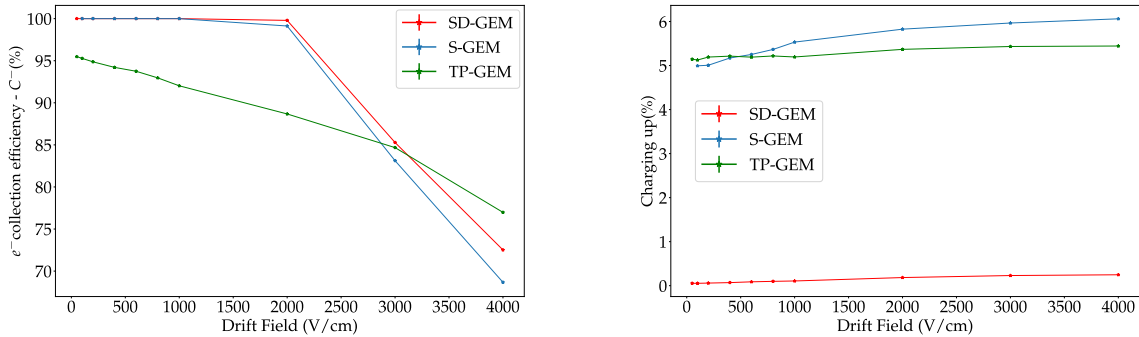


**Figure 6.25:** On the left, electron collection efficiency and on the right charging up effect, both as a function of the drift field for a standard GEM, a SD-GEM and a TP-GEM (details in the text).

It is possible to see that the electron collection efficiency is very compatible for both SD-GEM and the standard GEM (S-GEM) geometries, but is lower for the TP-GEM. The main difference is found when one looks at the charging up effect. The amount of charge accumulate in the dielectric is drastically reduce when a extra electrode is place in the middle of the structure. The charging up effect can affect the detector in terms of collection efficiency and gain, since this large amount of charge is going to virtually change the hole characteristics and consequently affect the behavior of the detector.

Figure 6.26 shows the ion extraction efficiency of the studied structures compared with a standard GEM. As it can be seen in equation 4.12, the IBF is going to be a function of the ion extraction efficiency since the gain and electron extraction efficiency hardly change by changing the drift field.

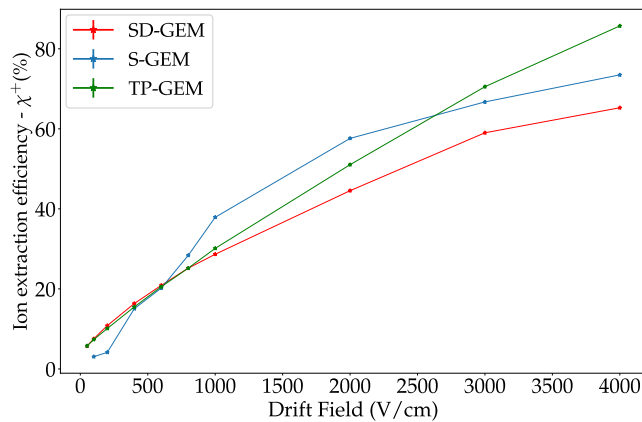


**Figure 6.26:** Ion extraction efficiency as a function of the drift region.

On both figures 6.26 and 6.25 the uncertainties regarding statistical deviation are calculated and plotted within the point. The curve is not smooth due to the low accuracy in the resolutions of the electric field that were corrected for the following simulations. Figure 6.27 shows the

electron collection efficiency and the ion extraction efficiency as a function of the drift region and the potential applied between the MM and the GEM foil.

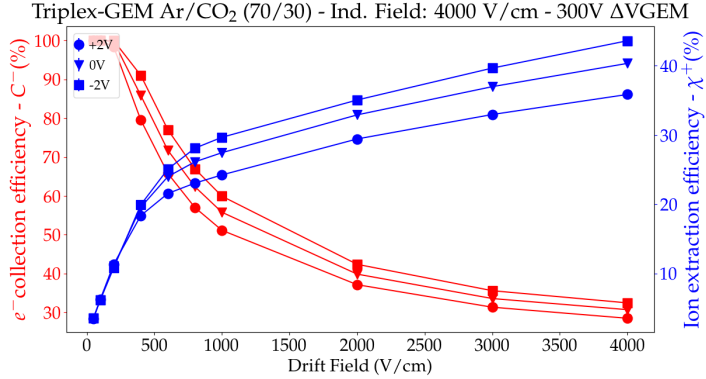


**Figure 6.27:** Electron collection efficiency and ion extraction efficiency calculated for three different potentials applied the extra electrode of the TP-GEM.

It is possible to see that by increasing the potential applied between the top and the middle electrode we decrease both the primary electron collection but also the extraction of ions. As the image shows, the best region to work, as expected, is the one with lower drift field.

We can compare the the same result with a standard GEM. Figure 6.28 shows the amount of charge collected and extracted as a function of the ratio between the MM and the GEM hole diameter. The dashed line represent the values for a standard geometry working with the same drift and extraction fields and also potential between the GEM electrodes.

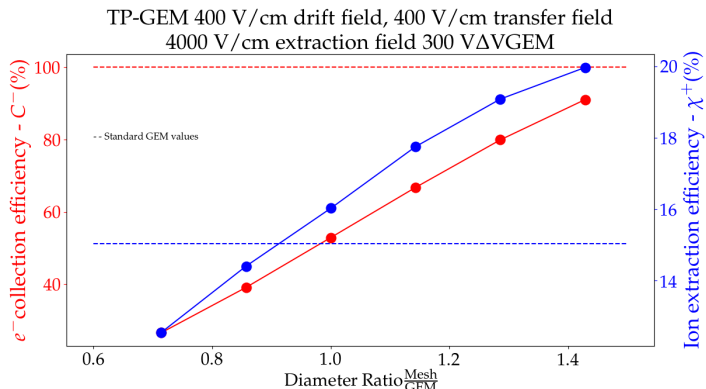


**Figure 6.28:** Collection efficiency and IBF for different diameters of the upper mesh. The dashed lines represent the standard GEM results for the same set of fields and potentials.

It is possible to see that we can suppress ion extraction using small holes in the mesh, however, are also going to lose a large amount of electrons hitting the top surface. Since collecting all the charge generated by the photon is the most important contribution to the energy resolution (due to low statistics, when one loses the primary charge, the energy resolution can be much more affected than losing charge after one or two stacks of multiplication), using

such geometry as a primary multiplication station would not be recommended, but in the future we intend to study how this structure behave as a second or third stage of multiplication in the stack.

### 6.6.2 Using a mesh to reduce the IBF

Different groups are prototyping mesh structures to reduce the amount of unwanted charge that passes through different regions of the detector and by doing that, reduce the IBF. Unlike the meshes with potential applied only during a fraction of time, like the gating grid scheme used in the original readout (MWPC based) of ALICE TPC[32], which may lead to complete block to the electrons and a high dead time for the detector, the idea is to use a continuous potential to the structure and to optimize the passage of electrons and ions.

Our group is performing some experimental work based on this principle[75]. The idea is to introduce a mesh in the middle of two different GEM structures just as figure 6.29 shows. The main idea of this problem is that applying a correct potential to the mesh, it is possible to divide the transfer region into two new regions that will work as an extraction region for the first GEM and a drift region for the second GEM.

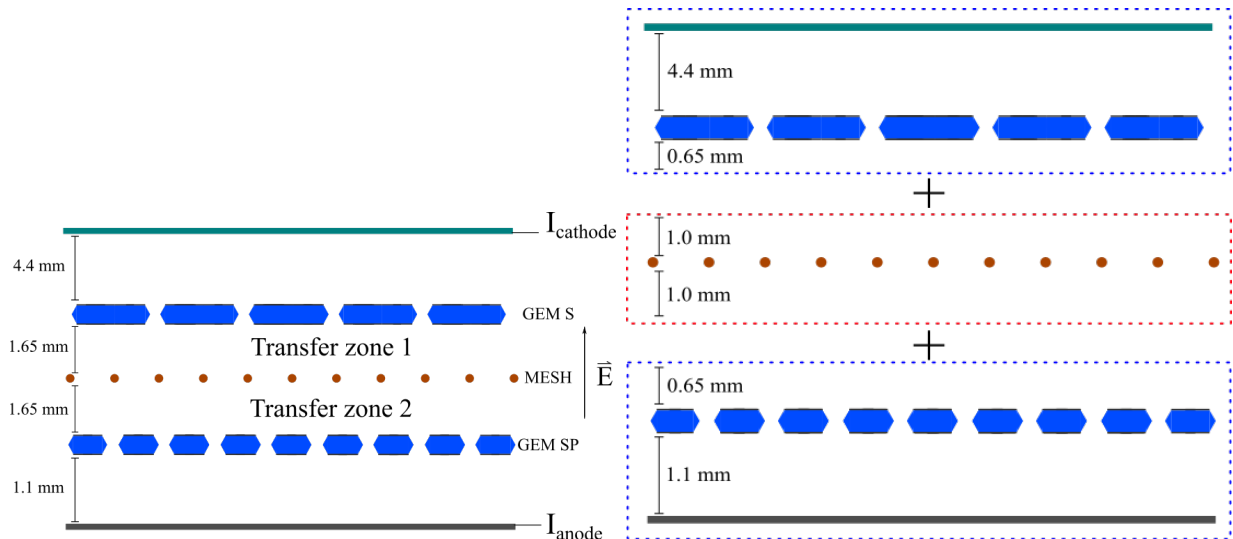


**Figure 6.29:** Left: Double GEM detector using a mesh to split the transfer zone in two. Right: Scheme of the simulated detector. 3 different unitary cell were made in order to generate a complete output.

Since a unitary cell for the complete configuration would be complex and heavy to load, we decided to divide the detector into tree different parts, just as shown in figure 6.29 (right) and to calculate the IBF using the efficiencies and transparencies curves.

To calculate the IBF using its definition(eq. 4.6) ones need to calculate both anode and cathode currents. The anode current can be written directly as:

$$I_{\text{ano}} = N_p G_{\text{eff}}^s T_m^- G_{\text{eff}}^{sp}$$

where  $N_p$  is the primary number of electrons,  $T_m^-$  is the mesh transparency for electrons and  $G_{\text{eff}}^s$  and  $G_{\text{eff}}^{sp}$  are the effective gain for the GEM-S and GEM-SP respectively. Knowing that  $G_{\text{eff}} = C^- G \chi^-$ , where  $G$  is the absolute gain, we can rewrite the anode current as:

$$I_{\text{ano}} = N_p C_s^- G_s \chi_s^- T_m^- C_{sp}^- G_{sp} \chi_{sp}^- \quad (6.11)$$

The cathode current will be the sum of 3 different contributions, the primary positive charge( $N_0^+ = N_p$ ), the ions that comes from the first GEM( $N_1^+$ ) and the ions that comes from the second GEM ( $N_2^+$ ). The ion contribution from the first GEM can be written as:

$$N_1^+ = N_p C_s^- G \chi_s^+$$

The ion contribution that comes through the mesh, generated at the second GEM( $N_m^+$ ):

$$N_2^+ = N_{sp}^+ T_s^+ T_m^+ \quad (6.12)$$

where  $T_m^+$  is the mesh transparency to ions and  $T_s^+$  is the standard (top)GEM transparency to ions. Naively one could assume that  $T_s^+ = \chi_s^+ C_s^+$ , however, looking at the transparency and extraction curves for ions, it can be seen that this quantities are not related. This effect is caused mainly due to the region inside the GEM hole that ions are created and the trajectory that they do towards the anode and the top electrode of the GEM.

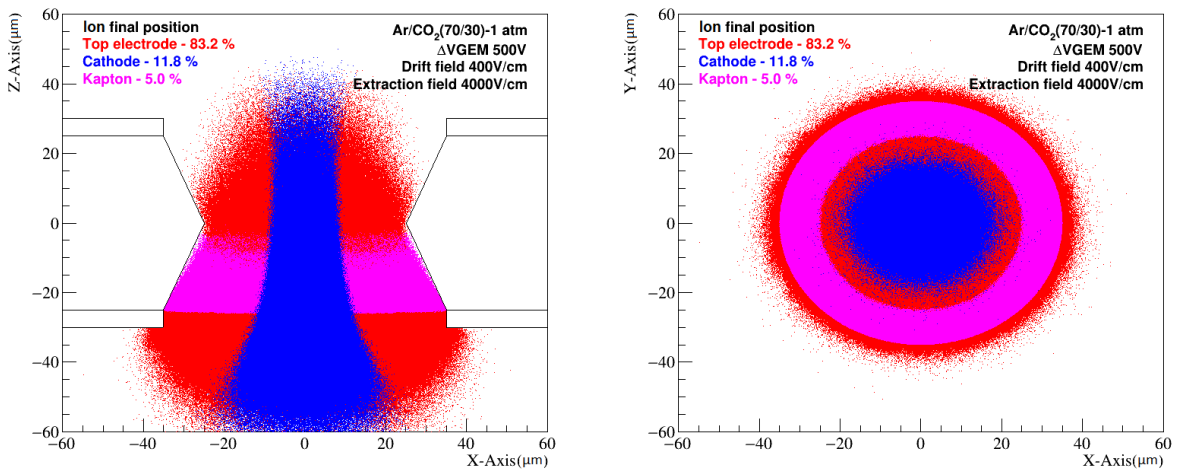


**Figure 6.30:** Initial position of ions generated on an avalanche. Each color indicates the final position after their drift.

Almost all the ions which are generated or passes through the middle of the hole end their

trajectory at the cathode as we may see in figure 6.30. This happens also for the ions that are created in a lower level GEM and drift towards the transfer region. Since the ion mobility is small, they have enough time to be deflected to the center of the hole and completely follow the electric field lines. In this way, the ion transparency is close to one for low transfer fields however it may drop when this field gets higher.

The number of ions that comes from the mesh will be related with the number of ions generated on the second GEM:

$$N_{sp}^+ = N_m^- C_{sp}^- G_{sp} \chi_{sp}^+ \quad (6.13)$$

where  $N_m^-$  is the amount of electrons that reaches the second GEM, coming from the mesh. They can be calculate using:

$$N_m^- = N_p C_s^- G_s \chi_s^- T_m^- \quad (6.14)$$

where  $T^-$  is the mesh transparency to electrons. Replacing values from equations 6.14 and 6.13 on equation 6.12, one can obtain:

$$N_2^+ = N_p C_s^- G_s \chi_s^- T_m^- C_{sp}^- G_{sp} \chi_{sp}^+ T_s^+ T_m^+ = N_m^- C_{sp}^- G_{sp} \chi_{sp}^+ T_s^+ T_m^+ = N_{sp}^+ T_s^+ T_m^+ \quad (6.15)$$

Summing the 3 contributions to the cathode charge, we get:

$$I_{cat} = N_0^+ + N_1^+ + N_2^+ = N_p + N_p C_s^- G_s \chi_s^+ + N_p C_s^- G_s \chi_s^- T_m^- C_{sp}^- G_{sp} \chi_{sp}^+ T_s^+ T_m^+ \quad (6.16)$$

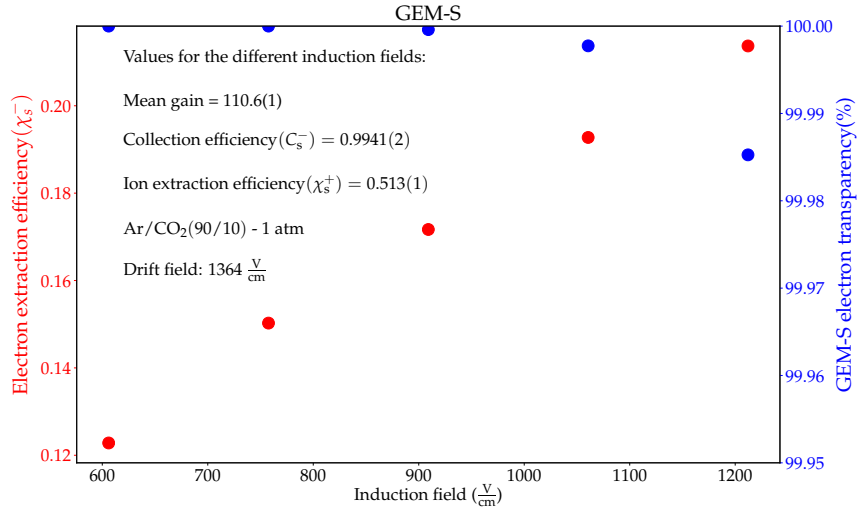
Using the ion back-flow definition:

$$IBF = \frac{I_{cat}}{I_{ano}} = \frac{N_p + N_p C_s^- G_s \chi_s^+ + N_p C_s^- G_s \chi_s^- T_m^- C_{sp}^- G_{sp} \chi_{sp}^+ T_s^+ T_m^+}{N_p G_s C_s^- \chi_s^- G_{sp} C_{sp}^- \chi_{sp}^- T_m^-}$$

rearranging the expression:

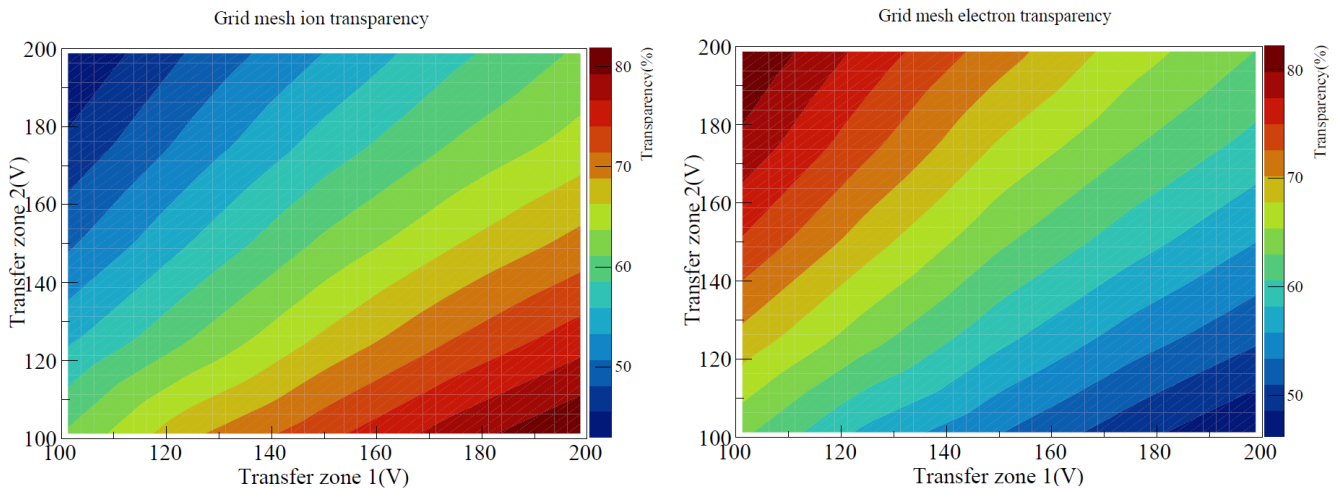
$$IBF = \frac{1 + C_s^- G_s \chi_s^+ + C_s^- G_s \chi_s^- T_m^- C_{sp}^- G_{sp} \chi_{sp}^+ T_s^+ T_m^+}{G_s C_s^- \chi_s^- G_{sp} C_{sp}^- \chi_{sp}^- T_m^-} \quad (6.17)$$

Figure 6.31 shows the electron extraction efficiency and electron transparency calculated for the GEM-S.



**Figure 6.31:** Electron extraction efficiency and electrons transparency as a function of the induction field.

Since the drift field was kept constant for different induction fields, the quantities that are somehow a function of the drift field, such as the collection efficiency for electrons and extraction efficiencies for ions are also constant. This will help us to confirm the independence of the electric field above and below the GEM foil. Its possible to see that the extraction efficiency for this structure has a linear relation with the external field. As it was said before, the electron transparency is close to one, although it start to change for huge induction field values due to charge loses to the bottom electrode. The uncertainties are limited to the point size.



**Figure 6.32:** Mesh transparency for ions (left) and electrons(right).

The mesh transparency for electrons and ions can be seen in figure 6.32. It is possible to

see that both behave in the opposite ways related to the field, that is, a high transparency to electrons is linked with a low transparency for ions, exactly what is wanted to reduce the ion back-flow value.

Looking at the last structure of the detector, the GEM-SP, the extraction efficiency for ions was calculated and can be seen in figure 6.33. The field value for 1060 V/cm shows a slightly discrepancy due to electric field resolution and will be recalculated in the future. Despite that we can see a linear relation between the extraction efficiency for ions and the drift field.

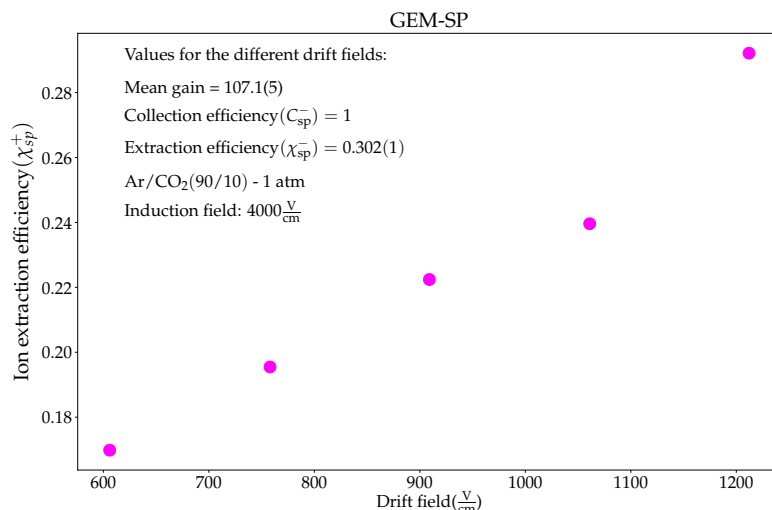


**Figure 6.33:** Ion extraction efficiency as a function of the drift field.

With all these results it is possible to use the equation 6.17 and obtain the value for IBF. Figure 6.34 shows the values obtained.

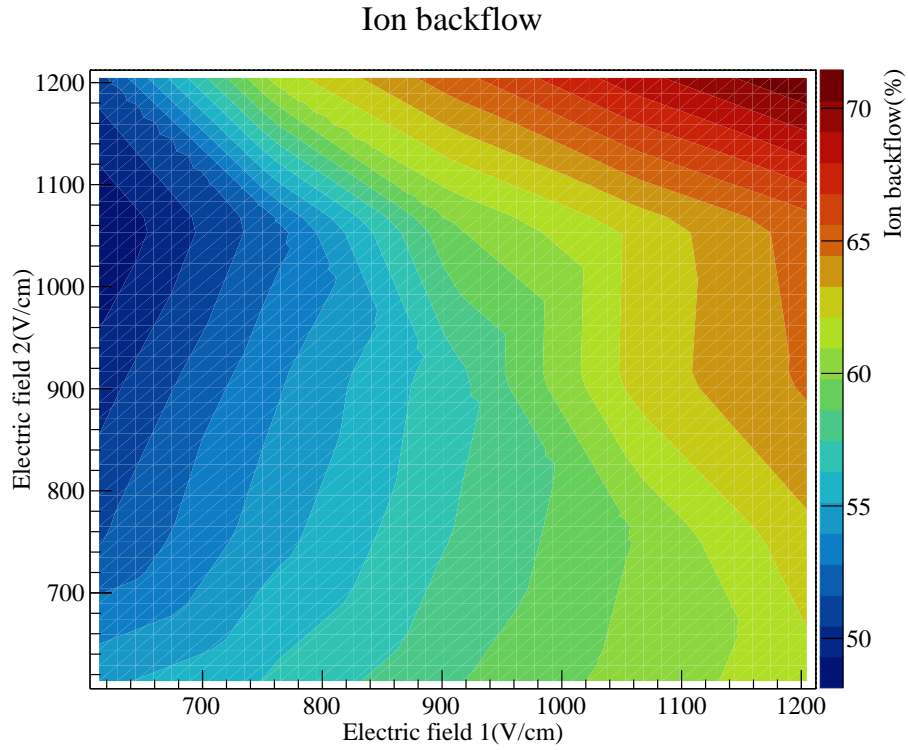


**Figure 6.34:** Ion back-flow calculated using equation 6.17.

It is possible to notice the clear influence of the transparency in the values obtained for the final IBF. The first hypothesis, to split the transfer region and maximize the efficiencies shows some contribution for the IBF reduction but is not the main value to be changed or optimize, while the mesh transparency is. The low electric field in the induction zone one and high fields in the drift region two gives a better fluency of electrons and suppress the movement of ions, minimizing the amount of positive charge that reaches the active volume of the detector.

# Chapter 7

## Experimental results

This chapter is going to be focused in the preliminary experimental results that were obtained during a first round of measurements in the laboratory. Further optimization of the system should be made in order to reduce noise and improve image quality (in terms of contrast and spatial resolution), along with pursuing better energy resolution.

The experimental setup, inside the shielding cage is presented in figure 7.1. Working in transmission mode we were able to evaluate the system spatial resolution using a specific lead pattern.

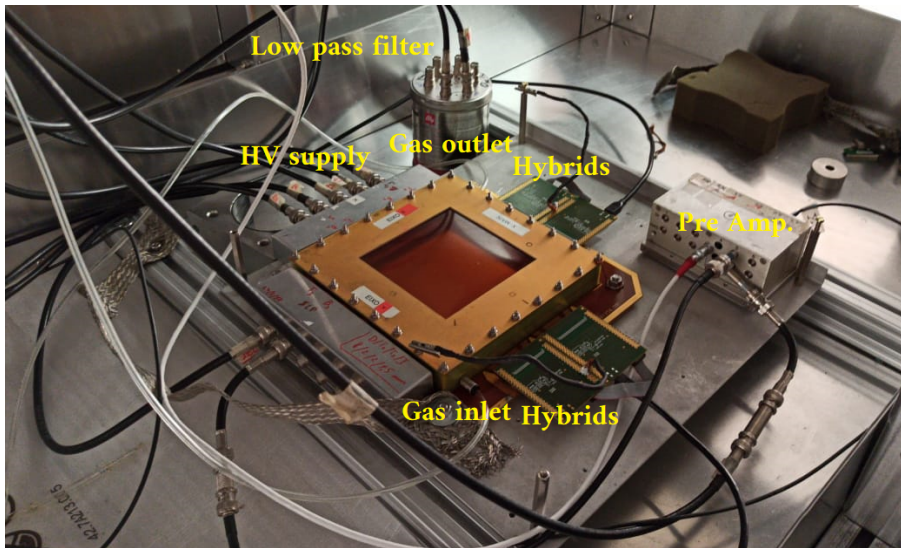


**Figure 7.1:** Picture of the detector inside the lead cage used for transmission and fluorescence images.

Placing the X-ray tube 25 cm above the detector's window, we were able to achieve a counting rate of about 1.5 kHz in transmission mode, limited only by the APV25 capability to process data. The X-ray tube current was set to 5  $\mu$ A and the acceleration potential to 10 kV. A 250  $\mu$ m thick aluminum filter was also added to the tube's exit window to filter lower energies and to reduce the counting rate to the desired value. Figure 7.2 shows the resolution pattern

picture and the reconstructed image.

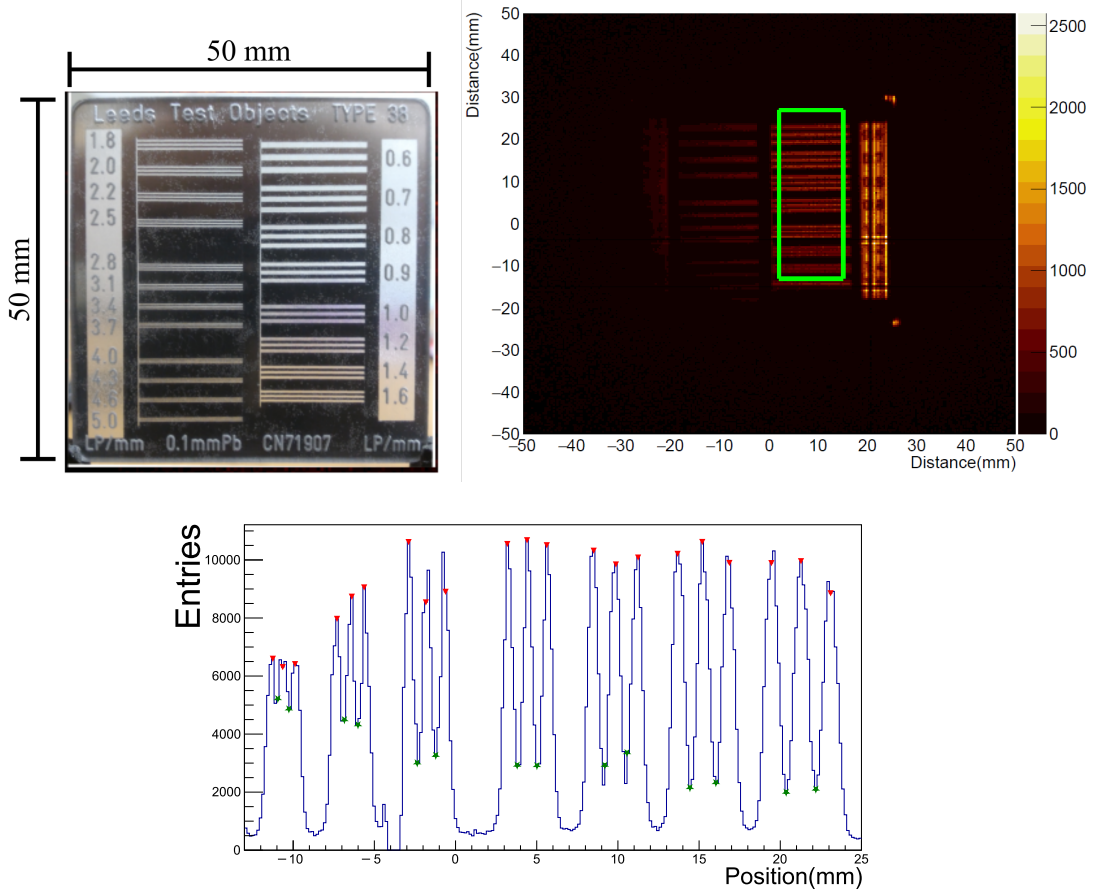


**Figure 7.2:** Top: Lead pattern picture and X-ray transmission image reconstructed using the SRS. Bottom Profile of the selected data from the green region.

One way to obtain the position resolution of an imaging system, that is, the minimum distance in which it is possible to distinguish two objects that are close to each other, is by calculating its Modulation Transfer Function (MTF). This method measures the contrast response of the system to different spatial frequencies [69].

The contrast can be obtained using the Michelson definition[76], as seen in equation 7.1. The absolute value of contrast will decrease for higher spatial frequencies (smaller objects) and the final resolving power of the detector is assumed to be the MTF at 10 % of contrast[77].

$$C = \frac{I_{max} - I_{min}}{I_{max} + I_{min}} \quad (7.1)$$

where  $I_{max}$  and  $I_{min}$  represents a bright and a dark spot (in terms of intensity) respectively.

The contrast is calculated using the peaks and valleys intensities on the profile image. Assuming that the position resolution is equivalent to the inverse of the spatial frequency at 10 %, these preliminary measurements provided a value of resolution power of at least 700  $\mu\text{m}$ .

To create fluorescence images a different arrangement needs to be made, illustrated in figure

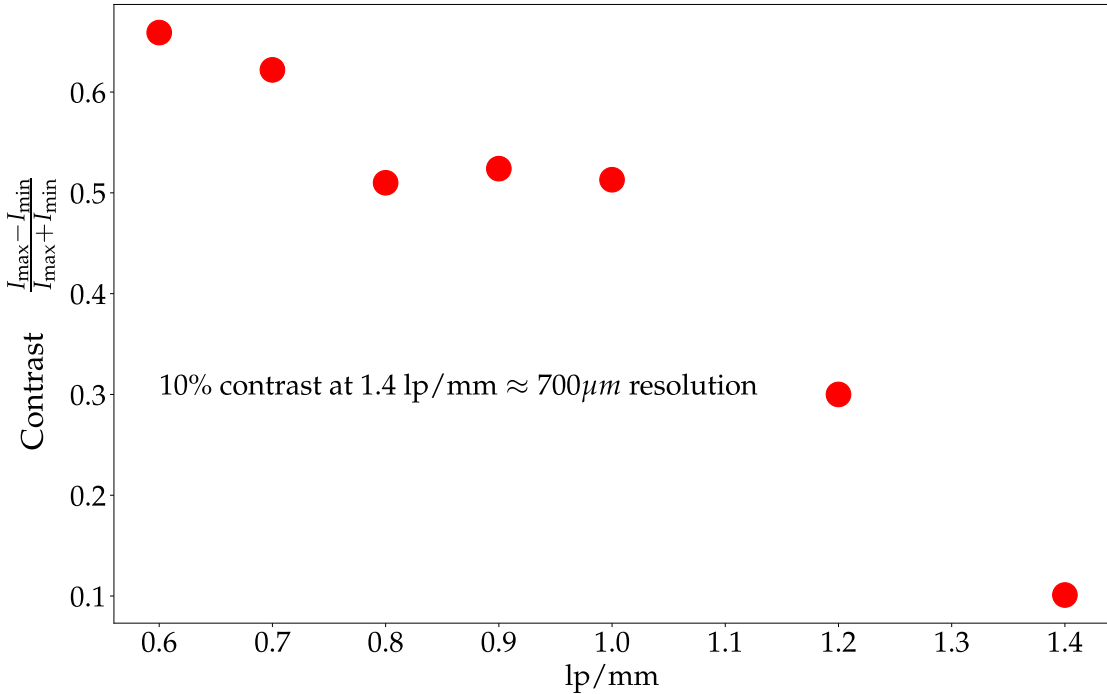


**Figure 7.3:** Preliminary measurements of contrast obtained for different spatial frequencies.

7.4. First of all, we need to change the position of the X-ray tube and to add a lead shielding above the detector window for preventing the passage of any radiation that does not come from the pinhole.

In this configuration the acquisition rate is lower than when doing transmission images. The average counting rates obtained for this experimental setup (1 mm tantalum pinhole and the mini-X X-ray tube[65] at maximum power) was 350 Hz, limited only due to geometric factors and the output current of the X-ray tube.

One of the first fluorescence images to test the system capability is from an titanium plate on top of which we glued several rectangular pieces of copper (check figure 7.5). Figure 7.6 shows the picture of plate and the reconstructed image using the SRS. The color scale in the image was developed in previous works [78] and made in a way that different energies are going to appear as different colors and the number of photons or events in each pixel is going to give a different level in the scale of dark to light.

At first, we can clearly notice in the image that the fluorescence intensity is different for the two different materials. As shown in chapter 6, our detector has its maximum efficiency for radiation with energies close to 8 kV, which is the same energy as the copper K fluorescence.

When we choose to look at a specific region of the image, we can reconstruct the energy spectrum for that part and use it to identify the presence of different elements. Figure 7.7

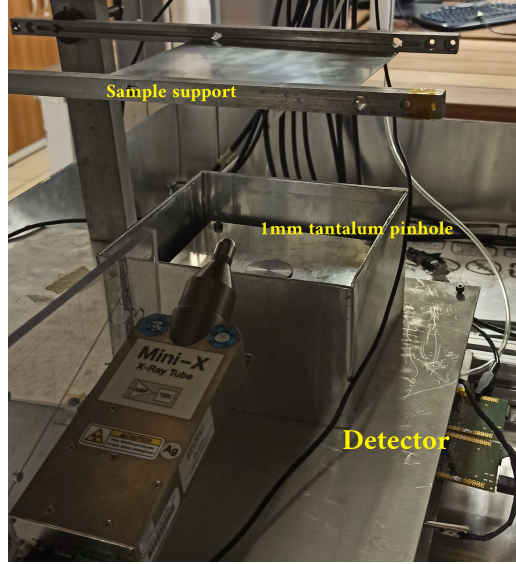


**Figure 7.4:** Picture of the detector mounted to acquire a X-ray fluorescence image. The complete setup is presented at figure 5.2 (right).



**Figure 7.5:** Picture of the titanium and copper plates used to perform the preliminary fluorescence image described in the text.

shows the energy spectrum for two different regions.

To improve the energy resolution of the system and consequently the capability to identify different elements we have mapped the gain distribution across all the active region of the detector. Doing so, we can later use the gain values for each sector to create a correction factor and so, obtain a uniform gain for the complete area of our system. An effective number for the gain was not calculated in this occasion, but what was measured was the relative peak position of the source in terms of ADC channels. This measurement was made placing an  $^{55}\text{Fe}$  source 10 cm above the detector window and irradiating the detector during several hours. Since it was not observed a change in the gain map over the time of this work, we assume that the mapping is something intrinsic to the geometry of the system due to the displacement and spacing between GEM foils, and so, we can use this same map to correct data runs that we have

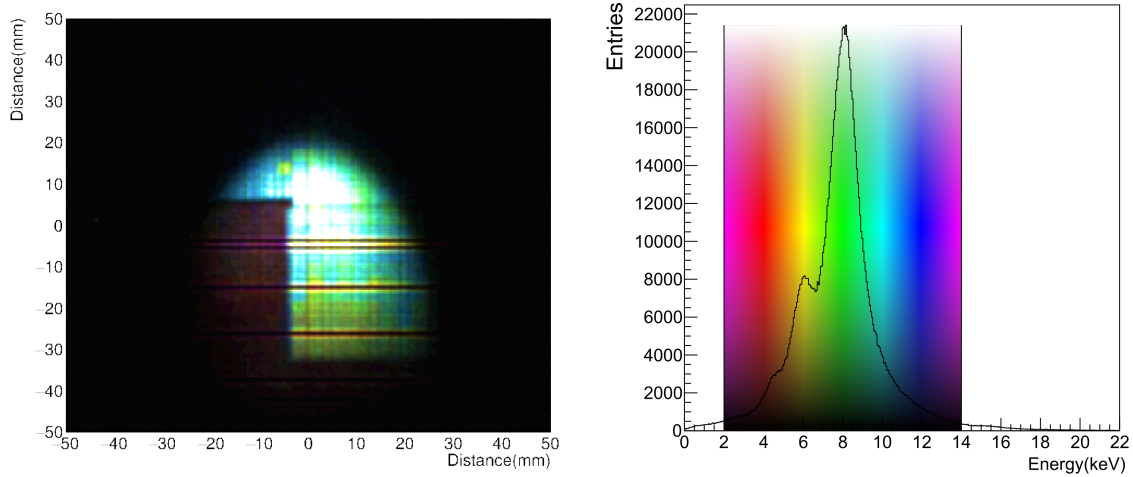


**Figure 7.6:** Left: Image reconstructed using the SRS system. Right: Energy spectrum and color scale palette that represent each energy.

taken in different moments. A data post processing chain was made to apply these corrections to data offline. We have divided the detector in 32 sectors for each dimension, obtain a total of 1024 regions, and for each one of them, the peak position of the  $K_{\alpha}$  fluorescence of  $^{55}\text{Fe}$  was measured. Figure 7.8 shows the value of gain (relative peak position) divided by the mean gain across the whole detector window.

Using these values, it is possible to make an equalization on the gain and to obtain a new energy spectrum, with a better resolution and more definition for each one of the emission lines.

The experimental results shown in this chapter were obtained using the APV25 system integrated with the SRS. In the near future we are going to modify all the system and analysis framework to be compatible with data obtained using the SAMPA chip. With SAMPA, we expect to improve the counting rate of events by a factor of at least 1000, reducing the acquisition time and obtaining better statistics for our analysis. The simulations results are also going to be used to create a contamination background for our energy spectrum and with it, obtain more reliable results. Using the geometric response curves for the detector and metallic concentration standards, we are also going to try to identify element concentration in specific samples, something new with gaseous detectors based on GEMs.

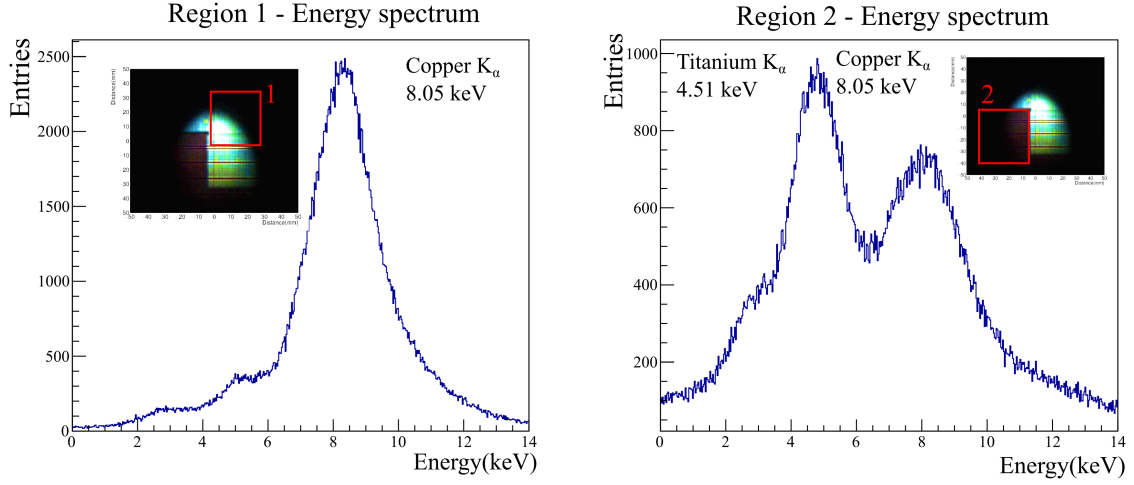


**Figure 7.7:** Left: Energy spectrum for the region 1, where there is only the presence of copper. Right: Energy spectrum for the region 2. We can see the presence of two 2 different elements.

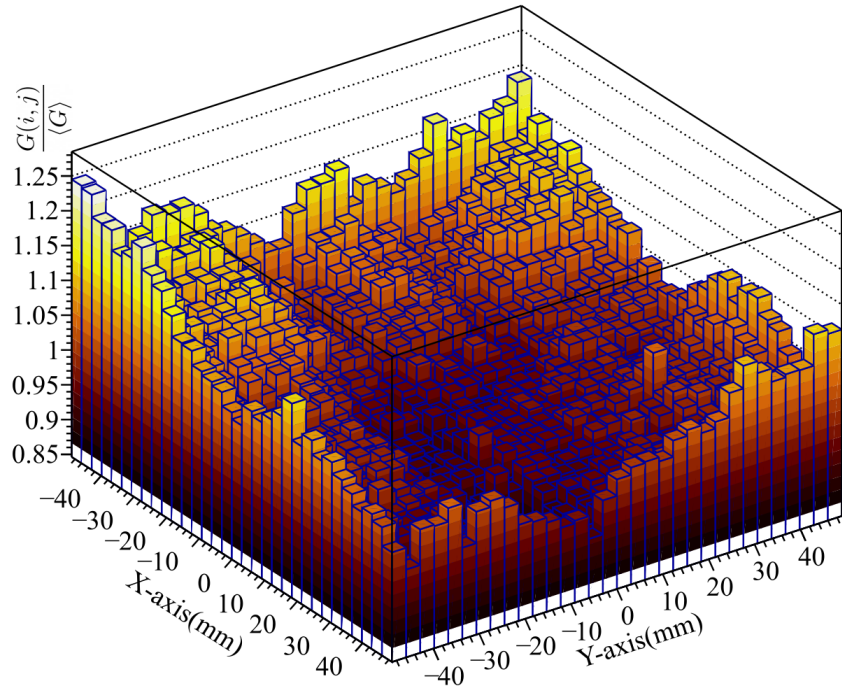


**Figure 7.8:** Gain mapping of the detector. Variations of approximately  $\pm 20\%$  can be observed, however, they can be corrected using a offline post processing analysis.

# Chapter 8

## Conclusion and next steps

The project proposed is ongoing and have already shown different results both in terms of understanding the problem and in creating tools for future analysis. The detector that have already shown different results in a past work[49] is now being optimize to an objective more specific which is the X-ray fluorescence. Due to the COVID-19 pandemic part of the work at the laboratory was delayed but during this time, several simulations were conducted.

The optimization in terms of quantum efficiency and escape peak suppression have shown us that a thicker drift region can help to reduce the acquisition time by increasing the efficiency of the detector and at the same time will reduce the background peaks generated due to the gas fluorescence. In the future we may also try to use krypton in our gaseous mixture to reduce even more any pollution in the energy spectrum, but since it is known that krypton may show a slightly worse position resolution [79], we need to prepare a detection system capable to operate in the optimize conditions related to the object that is going to be irradiated.

The first objective of the background contamination calculation was to create a model or tool that could help us to understand the undesired fluorescence and think in ways to reduce it. The geometric response simulation of the detector may also be in hand as a correction for the peak intensity and need to be taken into account when measuring element compositions.

The read-out studies will help us to understand both the cause of the artifacts that appear in our images and the changes that can be done to suppress them. There are different approaches to the center of mass algorithm when the charge that is taken into account in each strip can receive different weight, in order to given more importance to small charge signals or to completely ignore the presence of them. Since the problem can be suppressed but not completely eliminated, due to the characteristic of non-continuous charge reading, the flat field correction method is an important tool to remove artifacts that are intrinsic to the system and may help to reduce mistakes when one is characterizing an image system.

Regarding the ion back-flow studies we are still working in the laboratory to collect enough data and to compare results. This is an ongoing study that already shows important result

and possibilities to assemble a detector with a structure to mitigate the ion back-flow and to work at a constant potential. At first, the interest of placing a mesh inside the detector was to separate and create two independent electric fields, choosing specific values to optimize efficiencies. However, the mesh transparency itself is the main change to the charge flow. This work has the interest of different research groups and collaborations such as the RD51, and its of their interest the search for new possibilities for gaseous detector as new upgrades in terms of beam luminosity appears.

We are relatively in time with the work schedule and in the next months, with the possibility to restart the laboratory activity, new measurements with the SRS can be done. The first step now is to test the system with the detector that is already build and after that make some changes regarding the drift region depth and hopefully the first semi-quantitative analyses. To change the drift region for values above 2 cm a new frame may be required and new screws adapter to fix the GEM in position. A simulation will also be conducted to study the electric field deviation and both position resolution degradation for large drift regions. A way to work around this problem is to use conductive wires or structures to attenuate the distortions.

### 8.0.1 Schedule

The original schedule of the project can be seen below.

2019:

- Image system assembly and characterization using the SRS with the APV25 chip in X-ray transmission mode (done).
- Development of algorithm to reconstruct images and improve its quality (done).
- Obtaining the necessary credits for the doctorate (done).

2020:

- Development and study of quantitative and semi quantitative analysis (ongoing).
- Assembly of the system to work in X-ray fluorescence mode (done).
- Internship/collaboration at the GDD laboratory at CERN (delayed).

2021:

- Test with the system using the SAMPA chip (planned).
- Measurement of samples to develop a quantitative analysis (ongoing).

2022:

- Project and mounting of a portable system (ongoing).
- Thesis writing.

During the whole project:

- Simulations focused on the study of charge transport and radiation interactions with gaseous detector. Study through simulations on ways to reduce ion back-flow (partially done).
- Reading of articles linked to MPGDs and associated technologies and article focused in X-ray fluorescence and spectrometry techniques (ongoing).



# Bibliography

- [1] W. C. Röntgen, “Über eine neue art von strahlen,” *In Aus den Sitzungsberichten der Würzburger Physik.-medic. Gesellschaft Würzburg - pages 137–147, 1895. Tradução para o Português: A. C. P. Carvalho, “Sobre uma nova espécie de raios”, Rev. Imagem, 27(4):287-293, 2005.*
- [2] T. Arai, N. Langhoff, A. Simionovici, V. Arkadiev, W. Knüpfer, T. Cechak, J. Leonhardt, J. Chavanne, A. Erko, A. Bjeoumikhov, A. Alexander, B. Beckhoff, I. Grigorieva, B. Kanguießer, B. Vidal, F. Scholze, A. Longoni, C. Fiorini, L. Strüder, and W. Malzer, *Handbook of Practical X-Ray Fluorescence Analysis*. Springer, 05 2006.
- [3] D. Isabelle, “The PIXE analytical technique: Principle and applications,” *Radiation Physics and Chemistry*, vol. 44, no. 1, pp. 25–30, 1994.
- [4] W. R. Leo, *Techniques for nuclear and particle physics experiments: a how-to approach, 2nd ed.* Berlin: Springer, 1994.
- [5] G. Charpak, R. Bouclier, T. Bressani, J. Favier, and Č. Zupančič, “The use of multiwire proportional counters to select and localize charged particles,” *Nuclear Instruments and Methods*, vol. 62, no. 3, pp. 262 – 268, 1968.
- [6] D. R. Nygren, “The Time Projection Chamber: A New  $4\pi$  Detector for Charged Particles,” *eConf*, vol. C740805, p. 58, 1974.
- [7] F. Sauli, “GEM: A new concept for electron amplification in gas detectors,” *Nucl. Instr. Meth. A*, vol. 386, p. 531-534, 1997.
- [8] Y. Giomataris, P. Reboursgeard, J. Robert, and G. Charpak, “MICROMEGAS: a high-granularity position-sensitive gaseous detector for high particle-flux environments,” *Nucl. Instr. Meth. A*, vol. 376, no. 1, pp. 29 – 35, 1996.
- [9] R. Chechik, A. Breskin, C. Shalem, and D. Mörmann, “Thick GEM-like hole multipliers: properties and possible applications,” *Nucl. Instr. Meth. A*, 2004.

## BIBLIOGRAPHY

---

- [10] J. F. C. A. Veloso, J. M. F. Santos, and C. A. N. Conde, “A proposed new microstructure for gas radiation detectors: The microhole and strip plate,” *Rev. of Sci Inst. vol 71, no 6, p. 2371-2376*, 2000.
- [11] F. D. Amaro, C. Santos, J. F. C. A. Veloso, A. Breskin, R. Chechik, and J. Santos, “The thick-COBRA: a new gaseous electron multiplier for radiation detectors,” *Journal of Instrumentation, vol. 5, Out*, 2010.
- [12] J. Alme et al., “The ALICE TPC, a large 3-dimensional tracking device with fast readout for ultra-high multiplicity events,” *Nuclear Instruments and Methods in Physics Research Section A: Accelerators, Spectrometers, Detectors and Associated Equipment*, vol. 622, no. 1, pp. 316–367, 2010.
- [13] G. F. Knoll, *Radiation detection and measurement; 4th ed.* New York, NY: Wiley, 2010.
- [14] H. Schindler, “Garfield++ simulation of tracking detectors — user guide.” <https://garfieldpp.web.cern.ch/garfieldpp/>, 2017.2. Access in: 14-09-2018.
- [15] RD51 collaboration, “Development of micro-pattern gas detectors technologies.” <https://rd51-public.web.cern.ch/>, 2021. Access in: 28-06-2021.
- [16] R. M. Eisberg and R. Resnick, *Quantum physics of atoms, molecules, solids, nuclei and particles; 2nd ed.* New York, NY: Wiley, 1985.
- [17] K. S. Krane, *Introductory nuclear physics*. New York, NY: Wiley, 1988.
- [18] L. Pozzo, “Positron Emission Tomography PET / SPECT Systems Study Viability Quantification,” Master’s thesis, University of São Paulo - Institute of Physics, Brazil, 2005.
- [19] M. J. Berger, J. H. Hubbell, S. M. Seltzer, J. Chang, J. S. Coursey, R. Sukumar, D. S. Zucker, and K. Olsen, “XCOM: Photon Cross Sections Database,” *NIST Standard Reference Database 8 (XGAM)*, 2010. Access in: 13-10-2018.
- [20] R. Evans, *The Atomic Nucleus*. McGraw Hill Book Company, Inc., New York, 1955.
- [21] H. Bethe, “Zur theorie des durchgangs schneller korpuskularstrahlen durch materie,” *Annalen der Physik*, vol. 397, no. 3, pp. 325–400, 1930.
- [22] A. Cho, “Helium-3 shortage could put freeze on low-temperature research,” *Science (New York, N.Y.)*, vol. 326, pp. 778–9, 11 2009.
- [23] U.S. Departament of Energy - Office of Science, “Neutron and x-ray detectors,” *Report of the Basic Energy Sciences Workshop on Neutron and X-ray Detectors*, 2012.

- [24] ASTROLab du parc national du Mont-Mégantic, “Photographic plates.” [https://astro-canada.ca/les\\_plaques\\_photographiques-photographic\\_plates-eng](https://astro-canada.ca/les_plaques_photographiques-photographic_plates-eng), 2020. Access in: 05-06-2020.
- [25] “The ALICE TPC, a large 3-dimensional tracking device with fast readout for ultra-high multiplicity events,” *Nucl. Instr. Meth. A*, vol. 622, no. 1, pp. 316 – 367, 2010.
- [26] D. Primor, *Local tracking in the ATLAS muon spectrometer*. PhD thesis, Tel Aviv U., 2007.
- [27] A. Oed, “Position-sensitive detector with microstrip anode for electron multiplication with gases,” *Nucl. Instr. Meth. A*, vol. 263, no. 2, pp. 351 – 359, 1988.
- [28] F. Sauli and A. Sharma, “Micropattern gaseous detectors,” *Annual Review of Nuclear and Particle Science*, vol. 49, no. 1, pp. 341–388, 1999.
- [29] I. Manthos, I. Maniatis, I. Maznas, M. Tsopoulou, P. Paschalias, T. Koutsosimos, S. Kompogiannis, C. Petridou, S. E. Tzamarias, K. Kordas, C. Lampoudis, I. Tsiafis, and D. Sampsonidis, “The micromegas project for the atlas new small wheel,” *AIP Conference Proceedings*, vol. 2075, no. 1, p. 080010, 2019.
- [30] T. Kawamoto, S. Vlachos, L. Pontecorvo, J. Dubbert, G. Mikenberg, P. Iengo, C. Dallapiccola, C. Amelung, L. Levinson, R. Richter, and D. Lellouch, “New Small Wheel Technical Design Report,” Tech. Rep. CERN-LHCC-2013-006. ATLAS-TDR-020, Jun 2013. ATLAS New Small Wheel Technical Design Report.
- [31] F. Sauli, “The gas electron multiplier (GEM): Operating principles and applications,” *Nucl. Instr. Meth. A*, vol. 805, pp. 2 – 24, 2016. Special Issue in memory of Glenn F. Knoll.
- [32] “Upgrade of the ALICE Time Projection Chamber,” Tech. Rep. CERN-LHCC-2013-020. ALICE-TDR-016, Oct 2013.
- [33] A. Colaleo, A. Safonov, A. Sharma, and M. Tytgat, “CMS Technical Design Report for the Muon Endcap GEM Upgrade,” Tech. Rep. CERN-LHCC-2015-012. CMS-TDR-013, Jun 2015.
- [34] A. Cardini, G. Bencivenni, and P. De Simone, “The operational experience of the triple-GEM detectors of the LHCb muon system: Summary of 2 years of data taking,” *IEEE NSS/MIC Proceedings*, 759, 2012.
- [35] C. Altunbas, M. Capéans, K. Dehmelt, J. Ehlers, J. Friedrich, I. Konorov, A. Gandi, S. Kappler, B. Ketzer, R. D. Oliveira, S. Paul, A. Placci, L. Ropelewski, F. Sauli, F. Simon,

## BIBLIOGRAPHY

---

- and M. van Stenis, “Construction, test and commissioning of the triple-GEM tracking detector for COMPASS,” *Nucl. Instr. Meth. A*, vol. 490, no. 1, pp. 177 – 203, 2002.
- [36] D. Pfeiffer, F. Resnati, J. Birch, M. Etxegarai, R. Hall-Wilton, C. Höglund, L. Hultman, I. Llamas-Jansa, E. Oliveri, E. Oksanen, L. Robinson, L. Ropelewski, S. Schmidt, C. Streli, and P. Thuiner, “First measurements with new high-resolution gadolinium-GEM neutron detectors,” *Journal of Instrumentation*, vol. 11, pp. P05011–P05011, may 2016.
- [37] S. Uno, T. Uchida, M. Sekimoto, T. Murakami, K. Miyama, M. Shoji, E. Nakano, T. Koike, K. Morita, H. Satoh, T. Kamiyama, and Y. Kiyanagi, “Two-dimensional neutron detector with GEM and its applications,” *Physics Procedia*, vol. 26, pp. 142 – 152, 2012. Proceedings of the first two meetings of the Union of Compact Accelerator-Driven Neutron Sources.
- [38] Natal da Luz, H., Souza, F. A., Morales, M., Carlin, N., Oliveira, R. A. N., Bregant, M., Suaide, A. A. P., Chubaci, J. F. D., Matsuoka, M., Silva, T. F., Moro, M. V., Rodrigues, C. L., and Munhoz, M. G., “Characterization of multilayer thick-gem geometries as 10b converters aiming thermal neutron detection,” *EPJ Web Conf.*, vol. 174, p. 01012, 2018.
- [39] M. Köhli, M. Klein, F. Allmendinger, A.-K. Perrevoort, T. Schröder, N. Martin, C. J. Schmidt, and U. Schmidt, “CASCADE - a multi-layer boron-10 neutron detection system,” *Journal of Physics: Conference Series*, vol. 746, p. 012003, sep 2016.
- [40] D. Mörmann, A. Breskin, R. Chechik, and B. Singh, “On the efficient operation of a CsI-coated GEM photon detector,” *Nucl. Instr. Meth. A*, vol. 471, no. 3, pp. 333 – 339, 2001.
- [41] A. Morozov, L. M. S. Margato, M. M. F. R. Fraga, L. Pereira, and F. A. F. Fraga, “Secondary scintillation in CF4: emission spectra and photon yields for MSGC and GEM,” *Journal of Instrumentation*, vol. 7, pp. P02008–P02008, feb 2012.
- [42] M. Killenberg, S. Lotze, J. Mnich, S. Roth, R. Schulte, B. Sobloher, W. Struczinski, and M. Tonutti, “Modelling and measurement of charge transfer in multiple GEM structures,” *Nucl. Instr. Meth. A*, vol. 498, no. 1, pp. 369 – 383, 2003.
- [43] S. Bachmann, A. Bressan, L. Ropelewski, F. Sauli, A. Sharma, and D. Mormann, “Charge amplification and transfer processes in the gas electron multiplier,” *Nucl. Instrum. Meth.*, vol. A438, pp. 376–408, 1999.
- [44] “Bronkhorst®.” <https://www.bronkhorst.com/>. Access in: 25-01-2019.
- [45] “CAEN - Power Supply Module.” <https://www.caen.it/products/v6521/>. Access in: 25-01-2019.

- [46] “Raspberry Pi.” <https://www.raspberrypi.org/>. Access in: 25-01-2019.
- [47] A. L. M. Silva, M. L. Carvalho, K. Janssens, and J. F. C. A. Veloso, “A large area full-field edxrf imaging system based on a thcobra gaseous detector,” *J. Anal. At. Spectrom.*, vol. 30, pp. 343–352, 2015.
- [48] M. J. French *et al.*, “Design and results from the APV25, a deep sub-micron CMOS front-end chip for the CMS tracker,” *Nucl. Instr. Meth. A*, vol. A466, pp. 359–365, 2001.
- [49] G. G. A. de Souza, “X-Ray fluorescence imaging system based on Thick-GEM detectors,” Master’s thesis, University of São Paulo - Institute of Physics, Brazil, 2019.
- [50] M. Lupberger, L. Bartels, F. Brumbauer, M. Guth, S. Martoiu, H. Müller, E. Oliveri, D. Pfeiffer, L. Ropelewski, A. Rusu, and P. Thuiner, “Implementation of the vmm asic in the scalable readout system,” *Nuclear Instruments and Methods in Physics Research Section A: Accelerators, Spectrometers, Detectors and Associated Equipment*, vol. 903, pp. 91 – 98, 2018.
- [51] J. Adolfsson, A. A. Pabon, M. Bregant, C. Britton, G. Brulin, D. Carvalho, V. Chambert, D. Chinellato, B. Espagnon, H. H. Herrera, T. Ljubicic, S. Mahmood, U. Mjörnmark, D. Moraes, M. Munhoz, G. Noël, A. Oskarsson, L. Osterman, A. Pilyar, K. Read, A. Ruette, P. Russo, B. Sanches, L. Severo, D. Silvermyr, C. Suire, G. Tambave, K. Tun-Lanoë, W. van Noije, A. Velure, S. Vereschagin, E. Wanlin, T. Weber, and S. Zaporozhets, “SAMPA chip: the new 32 channels ASIC for the ALICE TPC and MCH upgrades,” *Journal of Instrumentation*, vol. 12, pp. C04008–C04008, apr 2017.
- [52] B. Henke, E. Gullikson, and J. Davis, “X-ray interactions: photoabsorption, scattering, transmission, and reflection at E=50-30000 eV, Z=1-92,” *Atomic Data and Nuclear Data Tables*, vol. 54, no. 2, pp. 181–342, 1993.
- [53] Thompson, A. *et al.*, *X-ray Data Booklet - LBNL/PUB-490 Rev.3*. Berkeley, CA, 94720: Lawrence Berkeley National Laboratory, 2009.
- [54] I. Smirnov, “Modeling of ionization produced by fast charged particles in gases,” *Nuclear Instruments and Methods in Physics Research Section A: Accelerators, Spectrometers, Detectors and Associated Equipment*, vol. 554, no. 1, pp. 474 – 493, 2005.
- [55] M. Ribeirete, A. Policarpo, M. Salete, S. Leite, M. Alves, and E. D. Lima, “Fano factors of krypton-xenon mixtures,” *Nuclear Instruments and Methods in Physics Research*, vol. 214, no. 2, pp. 561 – 563, 1983.
- [56] M. Kase, T. Akioka, H. Mamyoda, J. Kikuchi, and T. Doke, “Fano factor in pure argon,” *Nucl. Instr. Meth. A*, vol. 227, no. 2, pp. 311 – 317, 1984.

## BIBLIOGRAPHY

---

- [57] A. Orthen, H. Wagner, H. Besch, S. Martoiu, R. Menk, A. Walenta, and U. Werthenbach, “Gas gain and signal length measurements with a triple-gem at different pressures of Ar-, Kr- and Xe-based gas mixtures,” *Nucl. Instr. Meth. A*, vol. 512, no. 3, pp. 476 – 487, 2003.
- [58] J. Jaklevic, J. Kirby, M. Klein, A. Robertson, G. Brown, and P. Eisenberger, “Fluorescence detection of exafs: Sensitivity enhancement for dilute species and thin films,” *Solid State Communications*, vol. 23, no. 9, pp. 679 – 682, 1977.
- [59] L. Tröger, D. Arvanitis, K. Baberschke, H. Michaelis, U. Grimm, and E. Zschech, “Full correction of the self-absorption in soft-fluorescence extended x-ray-absorption fine structure,” *Phys. Rev. B*, vol. 46, pp. 3283–3289, Aug 1992.
- [60] H. Hirayama, “Lecture note on photon interactions and cross sections.” KEK, High Energy Accelerator Research Organization, Tsukuba, Ibaraki, Japan, 2000.
- [61] A. Kahoul, A. Abassi, B. Deghfel, and M. Nekkab, “K-shell fluorescence yields for elements with  $6 \leq z \leq 99$ ,” *Radiation Physics and Chemistry*, vol. 80, no. 3, pp. 369 – 377, 2011.
- [62] B. Mindur, T. Fiutowski, S. Koperny, P. Wiącek, and W. Dąbrowski, “Performance of a GEM detector with copper-less foils,” *Journal of Instrumentation*, vol. 12, pp. P09020–P09020, sep 2017.
- [63] B. Mindur, T. Fiutowski, S. Koperny, P. Wiącek, and W. Dąbrowski, “Investigation of copper-less gas electron multiplier detectors responses to soft x-rays,” *Sensors*, vol. 20, p. 2784, 05 2020.
- [64] M. Chernyshova, K. Malinowski, T. Czarski, E. Kowalska-Strzeciwilk, P. Linczuk, A. Wojeński, R. D. Krawczyk, and Y. Melikhov, “Advantages of al based gem detector aimed at plasma soft-semi hard x-ray radiation imaging,” *Fusion Engineering and Design*, vol. 146, pp. 1039 – 1042, 2019. SI:SOFT-30.
- [65] Amptek®, “Mini-x2 x-ray tube system for xrf.” <https://www.amptek.com/products/x-ray-sources/mini-x2-ray-tube#Documentation>, 2020. Access in: 04-07-2020.
- [66] F. M. Brunnauer, D. Munoz, D. Pfeiffer, E. Pollacco, E. Oliveri, F. I. G. Fuentes, F. J. I. Gutierrez, G. Norberg, L. Ropelewski, M. Lupberger, M. V. Stenis, P. Thuiner, and H. Muller, “Optical readout of gaseous detectors: new developments and perspectives.” VCI2019 - The 15th Vienna Conference on Instrumentation, 2019.
- [67] A. Zhang, M. Hohlmann, B. Azmoun, M. L. Purschke, and C. Woody, “A gem readout with radial zigzag strips and linear charge-sharing response,” *Nuclear Instruments and Methods in Physics Research Section A: Accelerators, Spectrometers, Detectors and Associated Equipment*, vol. 887, pp. 184 – 192, 2018.

- [68] D. Abbaneo, M. Abbrescia, C. Armagnaud, P. Aspell, Y. Assran, Y. Ban, S. Bally, L. Benussi, U. Berzano, S. Bianco, J. Bos, K. Bunkowski, J. Cai, J. Chatelain, J. Christiansen, S. Colafranceschi, A. Colaleo, A. Conde Garcia, E. David, G. de Robertis, R. De Oliveira, S. Duarte Pinto, S. Ferry, F. Formenti, L. Franconi, T. Fruboes, A. Gutierrez, M. Hohlmann, A. Kamel, P. Karchin, F. Loddo, G. Magazzu, M. Maggi, A. Marchioro, A. Marinov, K. Mehta, J. Merlin, A. Mohapatra, T. Moulik, M. Nemallapudi, S. Nuzzo, E. Oliveri, D. Piccolo, H. Postema, A. Radi, G. Raffone, A. Rodrigues, L. Ropelewski, G. Saviano, A. Sharma, M. Staib, H. Teng, M. Tytgat, S. Tupputi, N. Turini, N. Smilkjovic, M. Villa, N. Zaganidis, and M. Zientek, “Beam Test Results for New Full-scale GEM Prototypes for a Future Upgrade of the CMS High-eta Muon System,” pp. 1172 – 1176. 5 p, Nov 2012. 5 pages, 9 figures, submitted to Proc. 2012 IEEE Nucl. Sci. Symposium, Anaheim, CA.
- [69] U. Neitzel, E. Buhr, G. Hilgers, and P. R. Granfors, “Determination of the modulation transfer function using the edge method: Influence of scattered radiation,” *Medical Physics*, vol. 31, no. 12, pp. 3485–3491, 2004.
- [70] J. Friedrich, U. Leloglu, and E. Tunali, “Radiometric camera calibration of the bilsat small satellite: Preliminary results,” 02 2006.
- [71] N. Hagen, “Flatfield correction errors due to spectral mismatching,” *Optical Engineering*, vol. 53, p. 123107, 12 2014.
- [72] D. Mörmann, A. Breskin, R. Chechik, and D. Bloch, “Evaluation and reduction of ion back-flow in multi-gem detectors,” *Nuclear Instruments and Methods in Physics Research Section A: Accelerators, Spectrometers, Detectors and Associated Equipment*, vol. 516, no. 2, pp. 315 – 326, 2004.
- [73] S. Franchino, D. Gonzalez-Diaz, R. Hall-Wilton, R. Jackman, H. Muller, T. Nguyen, R. de Oliveira, E. Oliveri, D. Pfeiffer, F. Resnati, L. Ropelewski, J. Smith, M. van Stenis, C. Streli, P. Thuiner, and R. Veenhof, “Charge transfer properties through graphene for applications in gaseous detectors,” *Nuclear Instruments and Methods in Physics Research Section A: Accelerators, Spectrometers, Detectors and Associated Equipment*, vol. 824, pp. 571 – 574, 2016. Frontier Detectors for Frontier Physics: Proceedings of the 13th Pisa Meeting on Advanced Detectors.
- [74] R. de Olivera and M. Cortesi, “First performance evaluation of a multi-layer thick gaseous electron multiplier with in-built electrode meshes—MM-THGEM,” *Journal of Instrumentation*, vol. 13, pp. P06019–P06019, jun 2018.

## BIBLIOGRAPHY

---

- [75] C. M. C. C. L. Roux and P. H. F. N. da Luz, “Ion backflow studies in micropattern gaseous detectors,” *Simpósio Internacional de Iniciação Científica e Tecnológica da USP*, 2019. Accessed: 07/12/2020 - ISSN 2448-072X.
- [76] A. A. Michelson, “Studies in optics,” *University of Chicago*, 1927.
- [77] W. R. Hendee and E. R. Ritenour, *Medical Imaging Physics*, 4th ed. New York, NY: Wiley, 2002.
- [78] G. G. de Souza and H. N. da Luz, “Xrf element localization with a triple gem detector using resistive charge division,” *Nuclear Instruments and Methods in Physics Research Section A: Accelerators, Spectrometers, Detectors and Associated Equipment*, vol. 937, pp. 141–147, 2019.
- [79] C. Azevedo, S. Biagi, R. Veenhof, P. Correia, A. Silva, L. Carramate, and J. Veloso, “Position resolution limits in pure noble gaseous detectors for X-ray energies from 1 to 60 keV,” *Physics Letters B*, vol. 741, pp. 272–275, 2015.